ABSTRACT

CASSIDY, DANIEL. Numerical and Experimental Investigations of Mixed Convection in Solid-Liquid Flow for MicroPCM Applications. (Under the direction of Richard D. Gould.)

The present study is both a numerical and experimental investigation into the two phase flow of a microPCM fluid in a circular tube with mixed convection. The PCM was octacosane encapsulated by a polyethylene shell to form a spherical particle with an average diameter of 20 microns. The microPCM particles were suspended in a 50 / 50 ethylene glycol water mixture. The flow was through a 0.00775 m diameter copper tube with a length of approximately 0.75m. A constant wall heat flux was supplied by an electric resistance wire. The flow was gravity fed with a pumped circulation to maintain a constant pressure head. Experimental measurements were made of the tube outer wall at the top and bottom of the copper tube. Numerically an incompressible flow model was used with an Eulerian - Eulerian method to solve the two phase momentum and energy equations. The numerical model was verified using experimental data of single phase flow with mixed convection available in literature and was also verified by thermal results of both single phase and two phase flow from the experimental work in the current investigation.

Through a numerical investigation of the experimental conditions it was found that when the slurry was not cooled to a temperature far enough below the inlet temperature a supercooling effect did not allow a full use of the latent heat available in the octacosane microPCM, only about 50% of the total latent heat was used in one case. Further numerical investigations included tube wall material in which stainless steel was compared to the copper tubing used in the experiment. The inclusion of the solid phase buoyancy term was found to affect the thermal solution. A comparison was also made of microPCM flow rates in which the Reynolds number, the mass flow rate, and the pump power were each held constant and the solutions compared. It was then recommended that a constant pump power be used as a basis for comparison. A parametric study

was also completed in which the Rayleigh number and the Stefan number were both varied to find the effects on the thermal and hydrodynamic solution.

Numerical and Experimental Investigations of Solid-Liquid Flow with Mixed Convection for MicroPCM Applications

by
Daniel Cassidy

A dissertation submitted to the Graduate Faculty of
North Carolina State University
in partial fulfillment of the
requirements for the Degree of
Doctor of Philosophy

Mechanical Engineering

Raleigh, North Carolina

2007

APPROVED BY:

Dr. Andrey V. Kuznetsov	Dr. James W. Leach
Dr. Kevin M. Lyons	Dr. Richard D. Gould Chair of Advisory Committee

DEDICATION

Dedicated to: *My wife Kari, daughter Rebecca, and son Matthew who each bring joy to my life.*

BIOGRAPHY

Daniel Cassidy was born in Cleveland Ohio on December 27th 1967 to John and Evelyn Cassidy. After growing up in Cleveland he attended The University of Cincinnati graduating in June 1991 with a Bachelor of Science in Mechanical engineering. After working for several years as an engineer and receiving his professional Engineering license in the state of Ohio Dan returned to school and received his Masters of Science in Mechanical Engineering from Cleveland State University in 2002. Dan then pursued and completed his Doctor of Mechanical Engineering at The North Carolina State University in May of 2008.

ACKNOWLEDGEMENTS

Through out my studies at North Carolina State University many people have helped me both academically and personally through encouragement and time allowing me to concentrate on school. Specifically I would like to thank:

My advisor Dr. Richard D. Gould whose help and guidance through my studies have given me the direction and technical help to complete my work. Also thanks to my advisory committee: Dr. Andrey Kuznetsov, Dr. James Leach, and Dr. Kevin Lyons for their time and advice during my graduate work.

Thanks to my mother and father John and Evelyn Cassidy and brothers and sisters Margaret Cassidy, Paul Amato, Billy and Elaine Cassidy, and Rose and Steve Walsh whose love and encouragement helped me to complete my work.

And a special thanks to my wife Kari who encouraged me and provided support when it was needed. Also thanks to my children Rebecca and Matthew who were able to make me smile no matter what else was happening.

TABLE OF CONTENTS

LIST OF TABLES vii

LIST OF FIGURES viii

LIST OF SYMBOLS xi

1 INTRODUCTION 1
1.1 MicroPCM and thermal fluid background 1
1.2 Scope of work 5

2 THEORETICAL DEVELOPMENT 7
2.1 Solid-liquid flow analysis 7
2.1.1 Mass and volume concentrations 7
2.2 Governing equations 8
2.3 Geometry 9
2.4 Non-dimensionalization 10
2.4.1 Governing Equations and boundary conditions 10
2.4.2 Tube wall axial conduction 15
2.4.3 Closure equations 16
2.5 Phase change materials 19

3 EXPERIMENTAL 28
3.1 Experimental Setup 28
3.2 Fluid, microPCM, and slurry properties 31
3.2.1 Pure fluid properties 31
3.2.2 Ethylene glycol / water mixture properties 31
3.2.3 Particle properties 32
3.2.4 Slurry properties 33
3.3 Experimental verification 37
3.4 Experimental Results and Discussion 45
3.4.1 Varying the Mass flow rate 48
3.4.2 Rayleigh and Stefan numbers 49

4 NUMERICAL PROCEDURES 52
4.1 Grid 52
4.2 Two phase flow solution procedure 54
4.2.1 PEA 59
4.2.2 Concentration Equation solution modifications 61
4.2.3 Tube wall solution 62
4.2.4 Iterative procedure 64
4.3 Code Verification 66

4.3.1 Pure fluid flow comparison 66
4.3.2 Two phase experimental comparison 69

5 NUMERICAL RESULTS 73
5.1 Control case 73
5.2 Application considerations 78
5.2.1 Inlet Temperature 78
5.2.2 Tube Wall effects 80
5.2.3 Buoyancy effects 82
5.2.4 Concentration 86
5.3 Parametric investigation 89
5.3.1 Rayleigh number 89
5.3.2 Particle addition effects 90
5.3.3 PCM particles with melting 94
5.3.4 Stefan number 101

6 CONCLUSIONS 104
6.1 Future Recommendations 105
6.1.1 Experimental 105
6.1.2 Numerical 105

7 REFERENCES 107
APPENDICES 113
Appendix A 114
Appendix B 118

LIST OF TABLES

Table 3-1 Particle properties 34

Table 3-2 Error estimation values 39

Table 3-3 Single phase test matrix 40

Table 3-4 Two phase test matrix 46

Table 5-1 Summary of concentration / Ste test condition 88

Table 5-2 Outlet tube wall temperature differences at various Rayleigh numbers for a single phase fluid and a two phase fluid without phase change 92

Table 5-3 Outlet tube wall temperature differences melting vs no melt at various Rayleigh numbers 96

LIST OF FIGURES

Figure 2-1 Tube end view with coordinates 9

Figure 2-2 Effects of axial tube wall conduction 16

Figure 3-1 Experimental setup 29

Figure 3-2 MicroPCM slurry 33

Figure 3-3 Octacosane apparent specific heat,DSC data and curve fit 36

Figure 3-4 Bulk octacosane latent heat 37

Figure 3-5 Experimental comparison a) dimensionless wall temperature and b) dimensional wall temperatures 41

Figure 3-6 Fluid viscosities 43

Figure 3-7 Typical inlet / outlet connection section 44

Figure 3-8 Experimental setup end effects 45

Figure 3-9 PCM particle addition effects 47

Figure 3-10 Flow rate variation 49

Figure 3-11 Experimental upper and lower tube wall temperatures 50

Figure 4-1 Tube section - fluid and wall grid 53

Figure 4-2 Typical cell and variable locations 54

Figure 4-3 Typical cell layout for the radial momentum equation 56

Figure 4-4 Particle - particle interaction force 62

Figure 4-5 Numerical comparison with experimental and analytical data 67

Figure 4-6 Upper and lower wall temperatures 68

Figure 4-7 Two phase PCM numerical / experimental comparison 69

Figure 4-8 Dimensionless wall temperatures of the numerically corrected available inlet latent heat 72

Figure 5-1 Concentration / Temperature contour plots and velocity vector plots at various axial locations a) $z^+ = 0.0014$, b) $z^+ = 0.0024$, c) $z^+ = 0.0038$, and d) $z^+ = 0.0069$ 74

Figure 5-2 Axial concentration variations for control case 75

Figure 5-3 Velocity profiles for control case 77

Figure 5-4 Dimensionless axial tube wall temperatures 78

Figure 5-5 Tube wall temperature at various Inlet Temperatures 79

Figure 5-6 Circumferential outer wall temperatures 81

Figure 5-7 Particle buoyancy effects on upper and lower wall temperature a) copper tube and b) stainless steel tube 84

Figure 5-8 Buoyancy effects on solids concentration, temperature, and velocity at tube outlet a) neutrally buoyant copper wall, b) neutrally buoyant stainless wall, c) buoyant copper wall, and d) buoyant stainless wall 86

Figure 5-9 Stefan number variation at two concentrations 89

Figure 5-10 Mixed convection comparison of pure fluid and two-phase fluid at various Rayleigh numbers 91

Figure 5-11 Two phase no melting – single phase outlet cross stream flow comparison a) Two phase Ra_b=1.5 x 10^6, b) Single phase Ra_b=1.5 x 10^6, c) Two phase Ra_b=1.5 x 10^7, and d) Single phase Ra_b=1.5 x 10^7 93

Figure 5-12 Two phase no melting – single phase outlet velocity profile comparison 94

Figure 5-13 Rayleigh number variation 95

Figure 5-14 Concentration and temperature contours and velocity vectors at various Rayleigh numbers a) Ra_b= 0 melting, b) Ra_b= 0 no melt, c) Ra_b= 0.15 x 10^6 melting, d) Ra_b= 0.15 x 10^6 no melt, e) Ra_b= 15.0 x 10^6 melting, and f) Ra_b= 15.0 x 10^6 no melt 98

Figure 5-15 Solids concentration axial development at Ra_b = 15.0 x 10^6 99

Figure 5-16 Solids concentration and temperature contours and velocity vector plots for Ra_b=15.0 x 10^6 at z^+= 0.0011 99

Figure 5-17 Solids concentration axial development at Ra_b = 0 100

Figure 5-18 Outlet velocity profiles for two phase flow with and without PCM phase change 101

Figure 5-19 Stefan number variation 102

Figure 5-20 Contour and velocity vector plots a) Ste = ∞ (no melt), b) Ste = 21.6, c) Ste = 10.8 (control case), and d) Ste = 5.4 103

Figure B-1 Bulk octacosane DSC results from a heating 119

Figure B-2 Bulk octacosane DSC results from a cooling process……120

LIST OF SYMBOLS

Roman Symbols

A	area or a constant
a	coefficient
Ar	Archidemes number $\left(\left(1-\rho_s/\rho_l\right)gd^3/\nu_b^2\right)$
B, C, m	constants
Bi	Biot number $\left(hr/k\right)$
Cp	specific heat (J/kg-K)
D	inner tube diameter
d	diameter
E	alternate relaxation
F	flux
f	specific latent heat function (J/kg-K), friction factor as noted
f	body force
G	solids pressure term
Gr	Grashoff number $\left(g\beta q''D^4/\left(k\nu^2\right)\right)$
Gz	Graetz number $\left(\mathrm{Re}\,\mathrm{Pr}/\left(z/D\right)\right)$
g	gravity
h	heat transfer coefficient (W/m^2-K)
i	specific enthalpy (J/kg)
k	thermal conductivity (W/m-K)
K	momentum exchange factor
L	total specific latent heat (J/kg)
l	partial specific latent heat (J/kg)
Nu	Nusselt number $\left(hD/k\right)$
n	normal direction
P	pump power
p	pressure
Pe	Peclet number $\left(\mathrm{RePr}\right)$
Pr	Prandtl number $\left(\nu/\alpha\right)$
R	tube outside diameter (m)
$\dot{Q}$	volumetric flow rate
q″	heat flux (W/m^2)
R	tube outside diameter (m)
r	radial coordinate (m)
Ra	Rayleigh number $\left(g\beta q''D^4/\left(k\alpha\nu\right)\right)$
Re	Reynolds number $\left(\mathrm{u_m}2R/\nu\right)$
s	source term
Ste	Stefan number $\left(C_b q''D/k_b\right)/\left(cL\rho_p/\rho_b\right)$
T	temperature (ºC)

u	radial velocity (m/s)
U	dimensionless radial velocity $\left(v_r D/\nu_{lin}\right)$
V	dimensionless circumferential velocity $\left(v_\theta D/\nu_{lin}\right)$
$\forall$	volume
v	velocity (m/s)
w	error estimation
W	dimesionless axial velocity $\left(v_z/\nu_{z,m}\right)$
x	variable
Y	mass fraction
y	thermodynamic variable
z	axial coordinate (m)

Greek Symbols:

α	concentration
β	coefficient of volumetric expansion (K^{-1}), grid stretching parameter
δ	dimensionless Tube wall thickness $\left(\delta/D\right)$
Δ	tube wall thickness (m)
ε	fraction of latent heat $(0-1)$
ϕ	scalar variable
Γ	constant
μ	dynamic viscosity (m^2 /s)
ρ	density (kg/ m^3)
σ	standard deviation
τ	integration place holder
ω	constant or a relaxation factor as noted

Subscripts:

app	apparent
avg	average
b	bulk fluid or computational cell bottom face
EG	ethylene glycol
e	exit
eff	effective
F	free convection
f	fluid
i	computational cell index
in	inlet
l	liquid
m	mean
N	natural convection
n	computational cell north face
P	computational cell position

p	particle
q, *r*	index variable
PCM	phase Change Material
R	inside tube radius, dependent function
s	solid or computational cell south face
sb	subcooling
sl	solid to liquid phase change
ss	solid to solid phase change
s	solid or computational cell top face
tot	total
w	wall
wa	water

Superscripts:

*	Dimensionless variable
+	Alternate definition

Abbreviations:

DSC	differential scanning calorimeter
IPSA	Interphase slip algorithm
PCM	phase change material
PEA	Partial elimination algorithm
TC	thermocouple

1 INTRODUCTION

1.1 MicroPCM and thermal fluid background

The latent storage of heat has been used over the years to maintain a desired temperature while absorbing or releasing large amounts of heat energy. The latent heat of phase change is now being used in heat transfer and storage applications for both solid to liquid and liquid to vapor phase change processes, water, ice, paraffin, salts, and refrigerants are examples of materials used for the latent storage of heat through phase change. The solid to liquid phase transition is the focus of this work. Specifically, a solid to liquid phase change material (PCM) which is encapsulated in plastic of small diameter and then an appropriate amount of the microencapsulated PCM is added to a fluid resulting in a slurry. In the resulting slurry the microencapsulated particles remain in a particle form whether the PCM is in the liquid or solid state as the plastic does not melt. The slurry is used to enhance the transfer of heat in a pumped slurry application. The enhanced heat transfer is due mainly to the latent heat storage during the phase change with applications including computer chip cooling, avionics cooling[1], hybrid electric vehicle cooling,[2] energy savings applications such as solar thermal power[3] and building cooling load applications[4], or the possibility of any other heating / cooling process for which a pure fluid is now being used.

The addition of micro encapsulated PCM's was made possible as the process of microencapsulation was improved in the 1980's to be able to manufacture particles of increased strength[5] to with stand the stress found in circulating fluid systems. The microencapsulation of PCM's is now possible below a diameter of 10 microns.

The latent energy absorbed by the PCM during the melting process stores energy with little rise in the bulk fluid temperature throughout the melting process when compared to that of a single phase liquid in which the energy absorbed is stored by raising the temperature of the fluid. Over the years there have been several materials used as the PCM including water, salts, and waxes. The selection criteria include operating temperature (should be at or slightly below the phase change temperature), cost, availability, and amount of energy storage during the phase change process. A review of materials has been given by Gibbs and Hasnain[6] for solar applications and Himran et al.[7] for alkanes and paraffin waxes.

Both numerical and experimental investigations to the use of a microPCM slurry have been completed.[1,2,8-11] One of these was an experimental studied was completed by Goel et al.[8] in which eicosane was the PCM suspended in a circular tube under laminar flow conditions. Variations studied by Goel et al.[8] included various volumetric loadings, particle sizes, and thermal conditions. This experimental work was compared to the previous numerical work of Charunyakorn et al.[9] and significant differences in the numerical versus experimental wall temperatures were found. A number of possible causes of the discrepancy were suggested by Goel et al.[8] including the melting process occurring over a temperature range instead of a single melt temperature as was assumed in the numerical modeling of Charunyakorn et al.[9] Two subsequent numerical studies by Zhang and Faghri[10] and Cassidy and Gould[11] verified that the phase change of the eicosane occurring over a temperature range accounted for the majority of the differences. The phase change temperature range was not included in the numerical work by Charunyakorn et al.[9] The solid to liquid phase change occurring over a temperature range is common among many PCM's with published data available which includes the amount of latent heat and temperature dependent energy, including materials such as n-octadecane,[4] tricosane,[12] eicosane,[13, 14] technical grade paraffin wax,[15] and octacosane[2].

In addition to the above, other studies have been completed including micro-channel applications[16] and turbulent flow[17]. A more recent experimental study by Rao et al.[18] was completed using mini-channels with water as the carrier fluid and n-octadecane as the encapsulated PCM with an average size of 4.97 μm. The study found that heat transfer enhancement occurred over that of pure water at all flow rates at a concentration of 5% whereas at higher concentrations there was enhancement over water only at low mass flow rates, where the basis of comparison was equal mass flow rate for water and microPCM slurry. The lower thermal conductivity of the slurry, due to the lower conductivity of the microPCM particles, was suggested as the reason the higher flow rates at higher concentrations showed lower heat transfer enhancement[18].

The slurry flow in all of these applications was a two phase flow consisting of solid particles suspended in a liquid. Solid - liquid two phase flow, not specific to microPCM slurries, has been and continues to be an active area of research and includes both numerical and experimental studies.[16, 19, 20, 21] The field of two phase flow continues to change with current research while specifically to microPCM's Xing et al.[16] have performed numerical simulations accounting for the two phase flow aspects of microencapsulated PCM's for micro-fluidic applications. The numerical work of Xing et al.[16] included an axisymmetric assumption which neglected any gravitational effects. This assumption is not necessarily valid as Goel et al.[8] reported noticeable phase separation by observing a higher concentration of particles in the upper region of the outlet of the test section during their experiments. Although direct measurements of concentration were not made, Goel et al.[8] tested the effect of gravity on the tube wall temperatures by adjusting the density of the fluid to more closely match that of the particles resulting in particles which were closer to a neutrally buoyant condition. No noticeable changes in tube wall temperatures were measured. However, during the experiments the average circumferential tube wall temperatures

were measured instead of local, which along with thermal conduction along the circumference of the tube wall may have resulted in no noticeable temperature difference.

In addition to the latent heat and two phase flow aspects of using a pumped microPCM slurry as a forced convective thermal fluid, mixed convection may also occur, similar to that of a single phase fluid. The internal axial fluid flow through a tube causes forced convective cooling of the tube wall by the slurry and under certain circumstances cross stream circulation occurs within the fluid due to temperature dependent density variations.[22] This added circulation causes an axisymmetric flow to become three dimensional and the forced convection now includes free or natural convection.

The subject of natural convection has been extensively studied and includes books on the subject such as that by Gebhart et al.[23] which deals extensively with the subject. The added thermal effects of natural convection should be included during thermal analysis when the effects are of the same order as forced convection. Several methods have been found to estimate the conditions for which natural convection will be significant and include using the ratio of buoyancy forces to inertial forces (Gr/Re^2)[24] or using a flow regime map which provides regions of forced, free, and mixed convection.[25] Internal mixed convection in horizontal and vertical flows for single phase fluids has been extensively investigated,[22, 26, 27, 28, 29, 30] however neither numerical or experimental studies of mixed convection for a microPCM application were found. Purely buoyancy driven flows for a microPCM slurry have been investigated by Inaba et al.[31] for a cubical enclosure with no forced convection. During the study by Inaba et al.[31] the fluid was considered a homogenous solution with bulk properties defined, thus there was no accounting for solid liquid interactions in the two phase flow.

The thermal results of mixed convection during single phase tubular flow differs from axisymmetric pure forced convection applications as the hotter fluid will move to the top of the

tube due to a lower density when compared to the cooler fluid at the tube center. This can cause high temperature variations within the tube wall in the circumferential direction,[22] where as in axisymmetric flow the tube wall temperature would remain constant in the circumferential direction. The result of the buoyancy driven cross flow is an overall higher circumferentially averaged convective heat transfer coefficient when compared to pure forced convection in a tube; however locally in the upper portions of the tube the convective heat transfer coefficient may be lower.[22] This is dependent upon the tube wall material, thickness, and strength of cross flow circulation. These differences are still expected in the two phase slurry flow.

1.2 Scope of work

The current work is concerned with microPCM applications in which mixed convection is occurring along with the solid-liquid interactions inherent in the slurry. It is expected that the cross stream circulation present in mixed convection will enhance the heat transfer further by a bulk motion of the un-melted PCM from the flow center line to the heated wall. An attempt will be made to quantify the enhancements.

Both experimental and numerical investigations have been completed using octacosane as the microPCM encapsulated by a polyethylene shell and suspended in an ethylene glycol / water mixture forming the slurry. The application considered was a circular copper tube with a constant wall heat flux supplied and an applied pressure gradient causing laminar flow. Experimental data is limited to tube wall temperatures located both at the top and bottom of the outer tube wall at various axial locations and under several thermal and flow conditions with in the circular tube. Numerical methods are verified using experimental tube wall temperatures, of this and previous studies, and give insight into the cross stream and axial flow characteristics in addition to the

temperature results. Then, using the numerical methods developed, conditions which were not able to be investigated experimentally are investigated including a parametric investigation.

2 THEORETICAL DEVELOPMENT

2.1 Solid-liquid flow analysis

A solid-liquid flow system may be analyzed by any of several methods including Eulerian – Lagrangian, Eulerian – Eulerian, and homogeneous. In the present application a large number of small diameter particles (on the order of 20 μm) are suspended within a fluid at a volumetric fraction of 5 to 25 percent. The approximate number of particles at this size and a volumetric loading of 20 percent is $\#\ of\ \ particles = \frac{6\alpha_s}{\pi d_p^3} = 4.8\text{x}10^{13}$ particles/m^3, which is too many particles to be tracked by the Eulerian – Lagrangian method. Due to expected solid – liquid interactions along with mixed convection the Eulerian – Eulerian approach was chosen, specifically the interacting continua method was chosen due to a wide range of applicability.

2.1.1 Mass and volume concentrations

For the two phase flow application the solids mass concentration of a homogeneous mixture is defined as

$$Y_s = \frac{m_s}{m_s + m_l} \tag{2.1}$$

and the solids volumetric concentration is

$$\alpha_s = \frac{V_s}{V_{tot}} \tag{2.2}$$

From these definitions and for the current application the slurry consists only of two components, solid particles and liquid, the bulk density may defined as

$$\rho_b = \alpha_s \rho_s + (1-\alpha_s)\rho_l \tag{2.3}$$

2.2 Governing equations

Using an Eulerian – Eulerian approach for a solid-liquid flow the two phases are considered separate but interacting continua. To calculate both the hydrodynamic and thermal solutions two sets of the conservation of mass, momentum, and energy equations are required one for the liquid and one for the solid. Interaction terms are included in the momentum and energy equations to account for solid-liquid interactions. The general forms of the governing equations are

Continuity:

$$\frac{\partial}{\partial t}(\alpha_l \rho_l) + \nabla \cdot (\alpha_l \rho_l \mathbf{v}_l) = 0 \tag{2.4}$$

$$\frac{\partial}{\partial t}(\alpha_s \rho_s) + \nabla \cdot (\alpha_s \rho_s \mathbf{v}_s) = 0 \tag{2.5}$$

Momentum:

$$\frac{\partial}{\partial t}(\alpha_l \rho_l \mathbf{v}_l) + \nabla \cdot (\alpha_l \rho_l \mathbf{v}_l \mathbf{v}_l) = -\alpha_l \nabla (p_l) + \alpha_l \rho_l \mathbf{g} + \alpha_l (\mathbf{f}_{ls} + \mathbf{f}_{ll} + \mathbf{f}_{lw}) \tag{2.6}$$

$$\frac{\partial}{\partial t}(\alpha_s \rho_s \mathbf{v}_s) + \nabla \cdot (\alpha_s \rho_s \mathbf{v}_s \mathbf{v}_s) = -\nabla (\alpha_s p_s) + \alpha_s \rho_s \mathbf{g} + \alpha_s (\mathbf{f}_{sl} + \mathbf{f}_{ss} + \mathbf{f}_{sw}) \tag{2.7}$$

Energy:

$$\frac{\partial}{\partial t}\left(\alpha_l \rho_l h_l\right)+\nabla\cdot\left(\alpha_l \rho_l h_l \mathbf{v}_l\right)=\left[\frac{\partial\left(\alpha_l p_l\right)}{\partial t}-p_l\nabla\cdot\left(\alpha_l \mathbf{v}_l\right)\right]+ \nabla\cdot\left(\alpha_l k_l \nabla T_l\right)-\frac{6.0\alpha_s}{d_p}h\left(T_l-T_s\right) \tag{2.8}$$

$$\frac{\partial}{\partial t}\left(\alpha_s \rho_s h_s\right)+\nabla\cdot\left(\alpha_s \rho_s h_s \mathbf{v}_s\right)=\left[\frac{\partial\left(\alpha_s p_s\right)}{\partial t}-p_s\nabla\cdot\left(\alpha_s \mathbf{v}_s\right)\right]+ \nabla\cdot\left(\alpha_s k_s \nabla T_s\right)-\frac{6.0\alpha_s}{d_p}h\left(T_s-T_l\right) \tag{2.9}$$

2.3 Geometry

The current application is a horizontal circular tube flow with a constant wall heat flux. One half of the tube will be considered due to symmetry about the central vertical plane. Cylindrical coordinates were used and are defined in Fig.2-1,with the z coordinate being the axial direction.

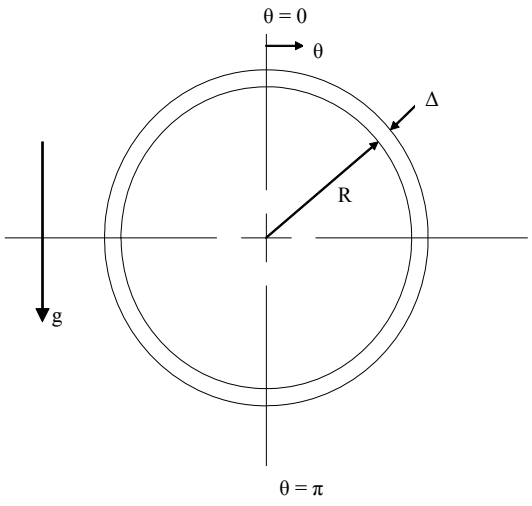

Figure 2-1 Tube end view with coordinates

2.4 Non-dimensionalization

2.4.1 Governing Equations and boundary conditions

The general equations of two phase flow, Eq.s 2-1 to 2.5, were put into cylindrical coordinates to describe the geometry of the current application and then were changed to dimensionless form using the following dimensionless definitions

$$\begin{aligned} r^* &= \frac{r}{D} & z^* &= \frac{z}{D\,\mathrm{Re}_b} & z^+ &= \frac{z}{D\,\mathrm{Re}_b\,\mathrm{Pr}_b} \\ T^* &= \frac{T - T_{in}}{\frac{q''D}{k_b}} & p^* &= \frac{p}{\rho_b w_m^2} & G^* &= \frac{G}{\rho_b w_m^2} \\ k^* &= k/k_b & \mu^* &= \mu/\mu_b & \rho^* &= \rho/\rho_b \end{aligned} \qquad 2.10$$

The resulting dimensionless governing equations are

Continuitiy:

$$\frac{1}{r^*}\frac{\partial}{\partial r^*}\left(\rho_q^*\alpha_q r^* U_q\right) + \frac{1}{r^*}\frac{\partial}{\partial \theta}\left(\rho_q^*\alpha_q V_q\right) + \frac{\partial}{\partial z^*}\left(\rho_q^*\alpha_q W_q\right) = 0 \qquad 2.11$$

Momentum:

r – direction

$$\rho_q^*\left(\frac{\partial}{\partial r^*}\left(\alpha_q U_q^2\right)+\frac{1}{r^*}\frac{\partial}{\partial\theta}\left(\alpha_q U_q V_q\right)-\alpha_q\frac{V_q^2}{r^*}+\frac{\partial}{\partial z^*}\left(\alpha_q U_q W_q\right)\right)=$$

$$-\alpha_q \mathrm{Re}_b^2\frac{\partial p^*}{\partial r^*}-\mathrm{B}G_b^*\mathrm{Re}_b^2\frac{\partial\alpha_p}{\partial r^*}+\mathrm{A}\alpha_q \mathrm{k}_q^*\rho_q^*\nu_{q\,\mathrm{in}}^{*2}\ \mathrm{Gr_l T}^*\cos\theta$$

$$-\mathrm{C}\alpha_q\alpha_r d_p^{*3}\rho_q^*\nu_{q\,in}^{*2}\mathrm{Ar}\cos\theta-K_{qr}^*\left(U_q-U_r\right) \qquad 2.12$$

$$+\left\{\frac{1}{r^*}\frac{\partial}{\partial r^*}\left(\alpha_q\mu_q^* r^*\frac{\partial U_q}{\partial r^*}\right)+\frac{U_q}{r^*}\frac{\partial\left(\alpha_q\mu_q^*\right)}{\partial r^*}-\frac{\alpha_q\mu_q^* U_q}{r^{*2}}\right.$$

$$\left.+\frac{1}{r^{*2}}\frac{\partial}{\partial\theta}\left(\alpha_q\mu_q^*\frac{\partial U_q}{\partial\theta}\right)-\frac{2}{r^{*2}}\alpha_q\mu_q^*\frac{\partial V_q}{\partial\theta}\right\}$$

θ – direction

$$\rho_q^*\left(\frac{\partial}{\partial r^*}\left(\alpha_q U_q V_q\right)+\frac{1}{r^*}\frac{\partial}{\partial\theta}\left(\alpha_q V_q^2\right)+\alpha_q\frac{U_q V_q}{r^*}+\frac{\partial}{\partial z^*}\left(\alpha_q V_q W_q\right)\right)=$$

$$-\alpha_q \mathrm{Re}_b^2\frac{1}{r^*}\frac{\partial p^*}{\partial\theta}-\mathrm{B}G^*\mathrm{Re}^2\frac{1}{r^*}\frac{\partial\alpha_q}{\partial\theta}+\mathrm{A}\alpha_q \mathrm{k}_q^*\rho_q^*\nu_{q\,\mathrm{in}}^{*2}\ \mathrm{Gr_l T}_q^*\sin\theta$$

$$+\mathrm{C}\alpha_q\alpha_r d_p^{*3}\rho_{\mathrm{q}}^*\nu_{q\,in}^{*2}\mathrm{Ar}\sin\theta-K_{qr}^*\left(V_q-V_r\right) \qquad 2.13$$

$$+\left\{\frac{1}{r^*}\frac{\partial}{\partial r^*}\left(\alpha_q\mu_q^* r^*\frac{\partial\left(V_q\right)}{\partial r^*}\right)+\frac{V_q}{r^*}\frac{\partial\left(\alpha_q\mu_q^*\right)}{\partial r^*}-\frac{\alpha_q\mu_q^* V_q}{r^{*2}}\right.$$

$$\left.+\frac{1}{r^{*2}}\frac{\partial}{\partial\theta}\left(\alpha_q\mu_q^*\frac{\partial V_q}{\partial\theta}\right)+\frac{2\alpha_q\mu_q^*}{r^{*2}}\frac{\partial U_q}{\partial\theta}\right\}$$

z – direction

$$\rho_q^*\left(\frac{\partial}{\partial r^*}\left(\alpha_q U_q W_q\right)+\frac{1}{r^*}\frac{\partial}{\partial\theta}\left(\alpha_q W_q V_q\right)+\frac{\partial}{\partial z^*}\left(\alpha_q W_q^2\right)\right)=$$

$$-\alpha_q\frac{\partial p^*}{\partial z^*}-\mathrm{B}G^*\frac{\partial\alpha_q}{\partial z^*}-K_{qr}^*\left(W_q-W_r\right) \qquad 2.14$$

$$+\left[\frac{1}{r^*}\frac{\partial}{\partial r^*}\left(\alpha_q\mu_q^* r^*\frac{\partial W_q}{\partial r^*}\right)+\frac{1}{r^{*2}}\frac{\partial}{\partial\theta}\left(\alpha_q\mu_q^*\frac{\partial W_q}{\partial\theta}\right)\right]$$

Energy:

$$\rho_q^* Cp_{q\,app}^* \left(\frac{\partial\left(\alpha_q U_q T_q^*\right)}{\partial r^*} + \frac{1}{r^*}\frac{\partial\left(\alpha_q V_q T_q^*\right)}{\partial \theta} + \frac{\partial\left(\alpha_q W_q T_q^*\right)}{\partial z^*} \right) =$$

$$-\frac{6\alpha_s \mathrm{Nu_p} d_p^{*2} k_l^*}{\mathrm{Pr}_b}\left(T_q^* - T_r^*\right) \qquad 2.15$$

$$+\frac{1}{\mathrm{Pr}_b}\left(\frac{1}{r^*}\frac{\partial}{\partial r^*}\left(r^* \alpha_q k_q^* \frac{\partial T_q^*}{\partial r^*}\right) + \frac{1}{r^{*2}}\frac{\partial}{\partial \theta}\left(\alpha_q k_q^* \frac{\partial T_q^*}{\partial \theta}\right) \right)$$

where $q = l \text{ or } s \text{ and } r = s \text{ or } l$, $\mathrm{A} = 1.0,\ B = 0.0, \text{and } C = 1.0$ when $q = l$ and $\mathrm{A} = 0.0,\ B = 1.0, \text{and } C = -1.0$ when $q = s$. Further more, the energy equation is given in temperature form where the relation $dh = Cp\,dT$ for an incompressible substance was used and the apparent specific heat, $Cp_{q\,app}^*$, will be defined later in Section 2.5. The pressure was assumed common for both phases[19] and development of the buoyant terms may be found in Appendix A.

During the development of the governing equations the flow was assumed to be steady, laminar, incompressible, Newtonian, with no viscous heat dissipation, and no axial diffusion. In addition the Bousinesq approximation was used to account for liquid density variations which cause the free convection of the liquid phase. A constant wall heat flux was applied at the outer surface of the tube wall and circumferential tube wall conduction was included. The wall heat flux was calculated and reported using the inner tube wall area. Within the tube wall region $\left(r^* = 0.5 \text{ to } 0.5 + \delta\right)$ only the energy equation is required to be solved

$$\frac{1}{r^*}\frac{\partial}{\partial r^*}\left(r^* \frac{\partial T_w^*}{\partial r^*}\right) + \frac{1}{r^{*2}}\frac{\partial^2 T_w^*}{\partial \theta^2} = 0 \qquad 2.16$$

The dimensionless boundary conditions for the given flow field and tube wall for the given geometry are:

Inlet:

$$Fluid\ region: r^* = 0\ to\ 0.5$$

$$\begin{aligned} p &= p_{in} \\ T^* &= 0 \\ W &= W_{in} \\ U &= V = 0 \end{aligned} \tag{2.17}$$

$$Tube\ wall\ region: r^* = 0.5\ to\ 0.5+\delta$$

$$\left.\frac{\partial T_w^*}{\partial z^*}\right|_{z^*=0} = 0 \tag{2.18}$$

Outlet:

$$Fluid\ region: r^* = 0\ to\ 0.5$$

$$\left.\frac{\partial \phi}{\partial z^*}\right|_{z^*=L^*} = Const. \tag{2.19}$$

$$p = 0.0 \tag{2.20}$$

$$Tube\ wall\ region: r^* = 0.5\ to\ 0.5+\delta$$

$$\left.\frac{\partial T_w^*}{\partial z^*}\right|_{z^*=L^*} = 0 \tag{2.21}$$

Outer wall:

$$\left.\frac{\partial T_w^*}{\partial r^*}\right|_{r^*=\delta+0.5} = \frac{1}{k_w^*(2\delta+1)} \tag{2.22}$$

Inner wall:

$$k_l^* \left.\frac{\partial T_l^*}{\partial r^*}\right|_{r^*=0.5} = k_w^* \left.\frac{\partial T_w^*}{\partial r^*}\right|_{r^*=0.5} = \mathrm{Nu}\left(T_l^*\Big|_{r^*=0.5} - T_b^*\right)$$

$$\left.\frac{\partial T_s^*}{\partial r^*}\right|_{r^*=0.5} = 0$$

$$T_l^*\Big|_{r^*=0.5} = T_w^*\Big|_{r^*=0.5} \qquad 2.23$$

$$U_l = V_l = W_l = U_s = V_s = W_s = 0$$

$\theta = 0$ and π:

$$V = \frac{\partial T^*}{\partial \theta} = \frac{\partial U}{\partial \theta} = \frac{\partial W}{\partial \theta} = \frac{\partial p^*}{\partial \theta} = 0 \qquad 2.24$$

Centerline:

$$\left.\frac{\partial T^*}{\partial r^*}\right|_{r*=0} = U = V = W = 0 \qquad 2.25$$

At the inner wall it was assumed that the heat was transferred entirely to the liquid phase and therefore an adiabatic boundary condition at the solids / wall interface results in Eq. 2.23. Energy to the solid phase was therefore transferred entirely by the thermal exchange coefficient found in Eq. 2.15. This assumption was used because the solid phase is small spherical particles making only point contact with the tube wall.

Five dimensionless numbers that appear in the governing equations are the Reynolds, Grashoff, Archidemes, Nusselt, and Prandtl numbers. The Reynolds and Prandtl numbers are each based on bulk fluid properties to be defined later, where as the Grashoff, Archidemes, and particle Nusselt numbers are defined as

$$\mathrm{Gr} = \frac{g\beta_l q'' D^4}{k_l \nu_l^2} \tag{2.26}$$

$$\mathrm{Ar} = \left\{ \left(1 - \rho_s / \rho_l\right) g d_p^3 / \nu_l^2 \right\} \tag{2.27}$$

$$Nu_p = \frac{h_p d_p}{k_l} \tag{2.28}$$

2.4.2 Tube wall axial conduction

Axial conduction within the tube wall has been neglected in Eq. 2.15 due to the physical conditions currently under consideration. Axial heat transfer within a tube wall has been examined extensively including Barozzie[32] in which axial conduction for an axis symmetric flow was found to depend upon the Peclet number (Pe), wall thickness to tube diameter ratio (δ), and fluid thermal conductivity to wall conductivity ratio (k_w^*). End effects were found to be negligible with large Pe, small k_w^*, or small δ. Similar results were found by Cassidy and Gould[11] for an axisymmetric microPCM flow. The nominal values for the current study are: Pe = 12000, k_w^* = 1000, and δ = 0.1 and has a dimensionless axial length range of $0.005 < z^+ < 0.02$. Results for an axisymmetric single phase flow are shown in Figure 2-2 in which axial tube wall conduction is clearly isolated to the tube ends in the axial range of interest.

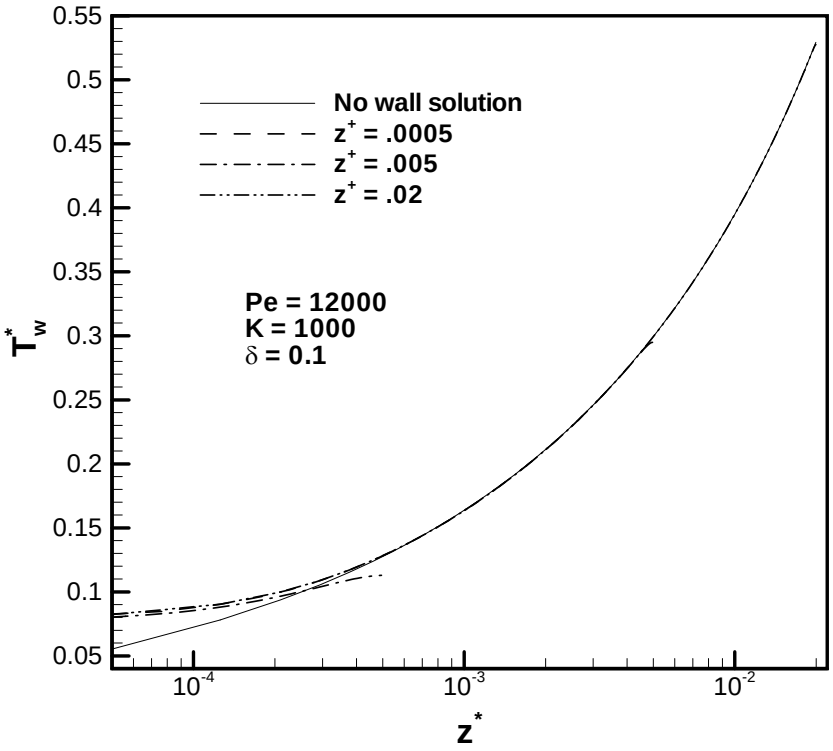

Figure 2-2 Effects of axial tube wall conduction

2.4.3 Closure equations

Equations to describe the fluid – solid interactions and the various properties are required to solve the governing equations.

The momentum exchange factor has been given by Bouillard et al.[33] as

$$K_{ls} = K_{sl} = \begin{cases} \frac{3}{4} C_D \frac{\alpha_l \alpha_s \rho_l \left| \mathbf{v}_l - \mathbf{v}_s \right|}{d_p} \alpha_l^{-2.65} & \alpha_l > 0.8 \\ 150 \frac{\alpha_s^2 \mu_l}{\alpha_l d_p^2} + 1.75 \frac{\alpha_s \rho_l}{d_p} \left| \mathbf{v}_l - \mathbf{v}_s \right| & \alpha_l \le 0.8 \end{cases} \qquad 2.29$$

and in dimensionless form

$$K^*_{U,ls} = \begin{cases} \frac{3}{4} C_D \alpha_l \alpha_s \left| U_l - U_s \right| d^*_p \rho^*_l \alpha_l^{-2.65} & \alpha_l > 0.8 \\ 150 \frac{\alpha_s^2 d^{*2}_p \mu^*_l}{\alpha_l} + 1.75 \alpha_s \left| U_l - U_s \right| d^*_p \rho^*_l & \alpha_l \le 0.8 \end{cases} \quad 2.30$$

$$K^*_{V,ls} = \begin{cases} \frac{3}{4} C_D \alpha_l \alpha_s \left| V_l - V_s \right| d^*_p \rho^*_l \alpha_l^{-2.65} & \alpha_l > 0.8 \\ 150 \frac{\alpha_s^2 d^{*2}_p \mu^*_l}{\alpha_l} + 1.75 \alpha_s \left| V_l - V_s \right| d^*_p \rho^*_l & \alpha_l \le 0.8 \end{cases} \quad 2.31$$

$$K^*_{W,ls} = \begin{cases} \frac{3}{4} C_D \alpha_l \alpha_s \left| W_l - W_s \right| \mathrm{Re}_b \, d^*_p \rho^*_l \alpha_l^{-2.65} & \alpha_l > 0.8 \\ 150 \frac{\alpha_s^2 d^{*2}_p \mu^*_l}{\alpha_l} + 1.75 \varepsilon_s \left| W_l - W_s \right| \mathrm{Re}_b \, d^*_p \rho^*_l & \alpha_l \le 0.8 \end{cases} \quad 2.32$$

where the coefficient of drag and Reynolds number are defined as[34]

$$C_d = \begin{cases} \frac{24}{\mathrm{Re}_p} \left(1 + 0.15 \, \mathrm{Re}_p^{0.687} \right) & \mathrm{Re}_p < 1000 \\ 0.44 & \mathrm{Re}_p \ge 1000 \end{cases} \quad 2.33$$

$$\mathrm{Re}_p = \frac{d_p \left| \mathrm{v}_l - \mathrm{v}_s \right|}{\nu_l} = \frac{1}{d^*_p} \frac{\rho^*_l}{\mu^*_l} \left| \mathrm{v}^*_l - \mathrm{v}^*_s \right| \quad 2.34$$

The first term on the right hand side of Eq. 2.7 is a pressure gradient term where

$$\nabla \left(\alpha_s p_s \right) = \alpha_s \nabla p + G \nabla \alpha_s \quad 2.35$$

It has been assumed that the pressure "p" is shared by both the solid and liquid phases[19] and the second term on the right hand side of Eq. 2.35 is the solids pressure. This term appears as the second quantity on the right hand side of each of the Eq.s 2.12 - 2.14 and is the solids phase pressure term which is found through empirical correlations for the particle-particle interaction force and includes a term, G^*. The effect of the solids pressure is to increase as the solids concentration increases then as the solids concentration approaches a compaction limit and the maximum possible solids concentration will be limited. There are a number of correlations for this

term some of which are discussed by Massoudi et al.[35] The correlation of Bouillard et al.[33] was used here

$$G = e^{-600.0\left(\alpha_{s,\max} - \alpha_s\right)} \tag{2.36}$$

where the compaction limit is $\alpha_{s,\max} = 0.624$ and the value of 600 is referred to as the compaction modulus.

The thermal exchange between the liquid and solid is found using the particle Nusselt number from Eq. 2.15 and was calculated using the Ranz-Marshall correlation[36] for a single sphere in a fluid with relative motion.

$$\mathrm{Nu}_p = 2 + 0.6\,\mathrm{Re}_p^{1/2}\,\mathrm{Pr}_l^{1/3} \tag{2.37}$$

Numerous additional correlations exist and are summarized by Floyd et al.[37]

Many correlations exist for the bulk viscosity of a solid-liquid flow of which Xing et al.[38] gives a summary under various conditions. The current work is a steady laminar flow and the bulk viscosity of the Thomas correlation for spherical particles[39] was used.

$$\frac{\mu_b}{\mu_l} = 1.0 + 2.5\alpha_s + 10.05\alpha_s^2 + 0.00273\, e^{16.6\alpha_s} \tag{2.38}$$

With no correlation available for the local dimensionless solid viscosity a linear approximation was used as suggested by Enwald et al.[40]

$$\mu_b = \alpha_l \mu_l + \alpha_s \mu_s \tag{2.39}$$

The local thermal conductivity of each phase and the local bulk fluid was calculated using a correlation by Kuipers, et al.[41]

$$k_b = k_{b,l} + k_{b,s} \tag{2.40}$$

where

$$k_{b,l} = \left(1.0 - \sqrt{1-\alpha_l}\right)k_l \tag{2.41}$$

$$k_{b,s} = \sqrt{1-\alpha_l}\left[\omega A + (1.0-\omega)\Gamma\right]k_l \tag{2.42}$$

$$\Gamma = \frac{2.0}{1.0-\frac{B}{A}}\left[\frac{A-1.0}{\left(1.0-\frac{B}{A}\right)^2}\frac{B}{A}\ln\left(\frac{A}{B}\right) - \frac{B-1.0}{1.0-\frac{B}{A}} - \frac{1.0}{2.0}(B+1.0)\right] \tag{2.43}$$

$$B = 1.25\left(\frac{1.0-\alpha_l}{\alpha_l}\right)^{10/9} \tag{2.44}$$

and for spherical particles

$$A = \frac{k_s}{k_l} \tag{2.45}$$

$$\omega = 7.26\,\mathrm{x}\,10^{-3} \tag{2.46}$$

This local bulk thermal conductivity was used for calculation when there was a slurry flow and is different than the bulk thermal conductivity of the stagnant slurry presented in Chapter 3.

2.5 Phase change materials

As discussed in Chapter 1, phase change can occur at a single temperature or over a temperature range. The effects of a phase change temperature range have been the subject of several studies and include arbitrarily shaped specific heat curves and material specific specific heat curves.[42, 43] In addition the phase change process for the heating of a given PCM could occur at different temperatures and the energy–temperature relation may be a different than the phase change process for the cooling of the PCM, this is particular to each PCM.[44] The shift in the

heating and cooling curves is known as super cooling. This phenomenon may be increased during the microencapsulation process; however the addition of nucleating agent can reduce this effect.[44] Some PCM's also have significantly lower thermal conductivities, particularly the waxes. This problem can also be minimized by adding small amounts of conductivity enhancing materials such as copper powder.[12]

The phase change materials considered in this work will have a phase change from a solid to a liquid over a temperature range and it will be assumed that both cooling and heating processes occur over the same temperature range and follow the same energy-temperature relation. The enthalpy of such an encapsulated phase change material is given in a particle form as

$$h_p = \begin{cases} Cp_p\left(T - T_{in}\right) & T < T_l \\ Cp_p\left(T - T_{in}\right) + Y_{PCM}\left(\int_{T_s}^{T_p} f dT - \int_{T_s}^{T_{in}} f dT\right) & T_s \le T \le T_l \\ Cp_p\left(T - T_{in}\right) + Y_{PCM} L & T > T_l \end{cases} \qquad 2.47$$

where, f, is a temperature dependent function describing the heat energy necessary to change the PCM from a solid to a liquid and the particle specific heat is defined in Chapter 3. The function f may be found through the use of a differential scanning calorimeter (DSC). The phase change at a single temperature may be found by letting the phase change temperature range approach zero.

The energy equation, Eq. 2.15, requires an apparent specific heat term, $Cp_{app,\,p}$, which is defined using the curve f and may be considered as an addition to the specific heat of the particle.

$$Cp_{app,\,p} = \begin{cases} Cp_p & T < T_l \\ Cp_p + Y_{PCM} f\left(T\right) & T_s \le T \le T_l \\ Cp_p & T > T_l \end{cases} \qquad 2.48$$

In dimensionless form the equation is

$$Cp^*_{app,\,p} = \frac{Cp_{app,\,p}}{Cp_b} = \begin{cases} Cp^*_p & T^* < T^*_l \\ Cp^*_p + Y_{PCM}\, f^*\left(T^*\right) & T^*_s \le T^* \le T^*_l \\ Cp^*_p & T^* > T^*_l \end{cases} \qquad 2.49$$

The equations of f and f^* are left undefined for now as they are dependent upon the specific PCM being used, for the current application these equations will be defined in Chapter 3.

3 EXPERIMENTAL

3.1 Experimental Setup

The experimental set up, Figure 3-1, was an open loop consisting of a constant heat transfer test section, adiabatic mixing, fluid cooler, volumetric flow rate capture vessel, circulating pump, and a gravity feed tube. The test section was made of a 9.525 mm OD (3/8") by 7.747 mm ID (0.305") copper tube with an over all length of 0.78 m. Of the 0.78 m length 0.75 m were wound with a 1.667 ohm/ft resistance wire, with approximately 1200 tightly wound wraps split into two sections along the length of the tube. The first section had a total resistance of 65.43 ohms while the second section had a total resistance of 70.72 ohms. Two layers of insulation were placed over the resistance wire; the first layer was 1" thick melamine insulation and the second layer was 2.5" thick urethane insulation.

There was an inlet section of approximately 10 diameters before the test section in addition the test section was thermally isolated using plastic fittings at the inlet and outlet. After the heated test section the working fluid was cooled using a counter flow concentric tube cooler with tap water as the cooling fluid. The flow rate of the test fluid was measured using the capture method in which a clear PVC pipe was volumetrically calibrated and a valve at the exit allowed for the capturing of the fluid during the measurement process without interrupting the test flow conditions. The time to fill 50 to 100 ml of fluid was measured using a stop watch, allowing for the calculation of a volumetric flow rate. The temperature of the captured fluid was measured and recorded to allow for the calculation of the test fluid / slurry density. The circulating pump was a centrifugal pump

by Lang which, by controlling the voltage, the speed of the pump was regulated to provide enough fluid flow for the gravity fed test section and some circulation to keep the gravity feed tank mixed (the microencapsulated particles were less dense than the suspending fluid and therefore tended to accumulate at the top over time). There was a pre-heater before the circulating pump to maintain the slurry at the inlet temperature. The gravity feed section was made of a PVC tube held at a constant height using the circulating pump and an overflow. The flow rate was controlled by raising or lowering the tubing discharge into the volumetric flow measurement tank which caused a decrease or increase of applied pressure gradient allowing the flow rate across the test section to be varied.

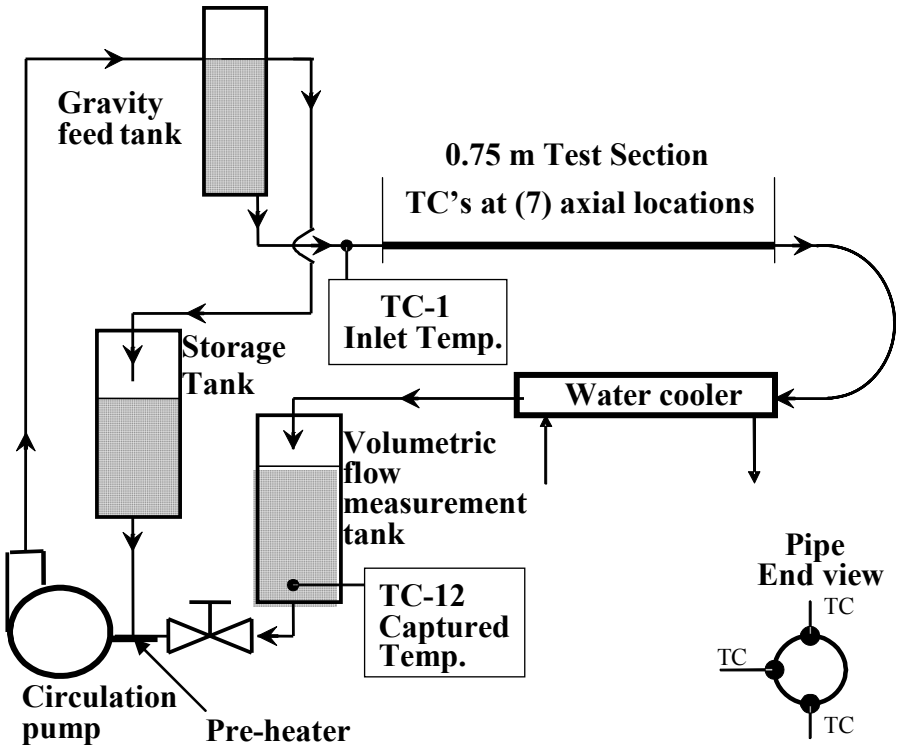

Figure 3-1 Experimental setup

There were 27 total type T thermocouples used to measure fluid and wall temperatures of the system and included a bulk inlet thermocouple, a bulk outlet thermocouple, captured fluid thermocouple, and 20 thermocouples used to measure wall temperature in the test section. The wall thermocouples were made by soldering the type T thermocouple wire to the copper tube outer wall. They were placed at both the top and bottom of the tube at eight axial positions, as shown in Figure 3-1. There were also four axial positions which included a third thermocouple 90 degrees from the top and bottom locations. The temperatures were recorded using an Agilent data acquisition unit with a distilled water ice bath as cold junction compensation.

The constant heat flux was applied at the outer wall using two sections of resistance wire wound around the tube and a voltage applied using a variable voltage transformer. A nominal 120 VAC was supplied by a wall outlet through a constant voltage transformer. The same voltage was applied to each section. To account for the difference in the resistances between the two heated sections an added resistance, before the windings of the first section, of 65.43 ohms was included so the total resistance and therefore the heat flux was equal for both heated sections. The voltage was adjusted and set using the variable voltage transformer as required by the testing conditions and the voltage drop across each section was recorded using the Agilent data acquisition unit. Using Ohms law a total heat input was calculated using the measured voltage drop and wire resistance. Then the heated length and tube diameter were used to calculate the applied heat flux.

After the flow rate and heat input (voltage) were set the system was allowed to reach steady state which was considered reached when the temperature at any thermocouple did not vary from a nominal value by more than plus or minus 0.07°C. Temperature and voltage were then recorded approximately every 3 seconds for at least 1 minute. The average value over the one minute of recording time was then used for all calculations and graphics.

3.2 Fluid, microPCM, and slurry properties

3.2.1 Pure fluid properties

The density, viscosity, and thermal conductivity of pure water and pure ethylene glycol were found using the following equations presented by Sun et. al[45] (constants available in original publication)

Ethylene Glycol:

$$k \text{ or } \rho = A_1 + A_2 T + A_3 T^2 \tag{3.1}$$

$$\ln \mu = A_1 + \frac{A_2}{(T + A_3)} \tag{3.2}$$

Water:

$$\rho = 1002.17 - 0.116189T - \left(0.358024\, x10^{-2}\right)T^2 + \left(.373667\, x10^{-5}\right)\ T^3 \tag{3.3}$$

$$\ln \mu = -3.758023 + \frac{590.9808}{(T + 137.2645)} \tag{3.4}$$

$$k = 0.570990 + \left(0.167156\, x10^{-2}\right)T - \left(0.609054\, x10^{-5}\right)T^2 \tag{3.5}$$

The specific heat was found using the following equation from Daubert and Danner[46] (constants available in original publication) and is used for both water and ethylene glycol.

$$Cp = A_1 + A_2 T + A_3 T^2 + A_4 T^4 \tag{3.6}$$

3.2.2 Ethylene glycol / water mixture properties

The density, viscosity, and thermal conductivity of a 50 / 50 mixture by volume of ethylene glycol and water were calculated using the following equation[45]

$$y = Y_{EG} y_{EG} + Y_{wa} y_{wa} + \left(y_{EG} - y_{wa}\right) Y_{EG} Y_{wa} \left(A_4 + A_5 Y_{EG} + A_6 T\right) \quad 3.7$$

where, $y = \rho, \ln \mu, or\ k$.

The specific heat of the mixture was found from an energy balance and was dependent upon the mass fraction of each component

$$Cp = Y_{EG} Cp_{EG} + Y_{wa} Cp_{wa} \quad 3.8$$

The coefficient of volumetric expansion of the fluids and mixture was calculated using the definition

$$\beta = -\frac{1}{\rho}\frac{\partial \rho}{\partial T} \quad 3.9$$

3.2.3 Particle properties

The microencapsulated particle consist of two parts an outer wall and a core material which is the PCM. The particle properties are defined as follows

Thermal conductivity[9]

$$\frac{1}{k_p d_p} = \frac{1}{k_{PCM} d_{PCM}} + \frac{d_p - d_{PCM}}{k_w d_{PCM} d_p} \quad 3.10$$

Density:

$$\rho_p = Y_{PCM} \rho_{PCM} + \left(1 - Y_{PCM}\right) \rho_w \quad 3.11$$

Specific heat:

$$Cp_p = Y_{PCM} Cp_{PCM} + \left(1 - Y_{PCM}\right) Cp_w \quad 3.12$$

where the particle specific heat was found using an energy balance.

3.2.4 Slurry properties

With the addition of the microPCM particles to the base fluid (50/50 ethylene glycol / water) a slurry was formed in which the particles had a mean diameter of 20 microns. A mass concentration of 23% particles was used through the entire experiment which corresponds to a 26.3% volumetric concentration with the fluid at room temperature. The volumetric concentration will vary slightly with variations in the carrier fluid and PCM density. Considering the extreme operating temperatures in the majority of this experiment, at a temperature of 58.85 ºC the volumetric concentration is 25.6% while at a temperature of 90.0 ºC the volumetric concentration is 26.4%. A microscopic picture of the slurry showing the solid particles is shown in Fig.3-2.

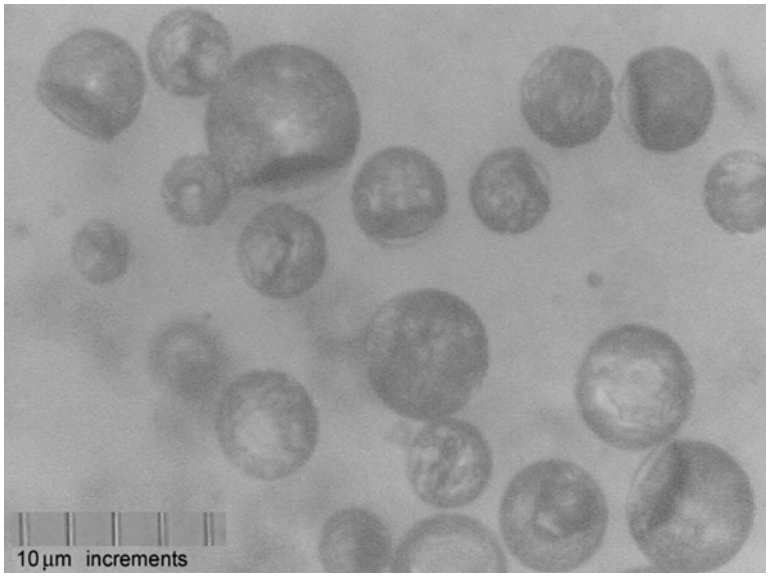

Figure 3-2 MicroPCM slurry

The bulk properties of the slurry were calculated using the following equations.

Bulk thermal conductivity of stagnant slurry[9]

$$\frac{k_b}{k_l} = \frac{2 + k_p/k_l + 2\alpha_p\left(k_p/k_l - 1\right)}{2 + k_p/k_l - \alpha_p\left(kp/k_l - 1\right)} \qquad 3.13$$

The bulk viscosity used was developed by Thomas[39] and was given previously by Eq. 2.36 and the bulk density was previously given be Eq. 2.3.

The specific heat was found using an energy balance as

$$Cp_b = Y_p Cp_p + \left(1 - Y_p\right)Cp_{50/50} \qquad 3.14$$

The current study uses octacosane as the PCM encapsulated by a polyethylene wall in which 83% by weight is the PCM. Individual properties of the wall and PCM are listed in Table 3-1.

Table 3-1 Particle properties

Property	Octacosane	Polyethelene Particle Wall
$Cp\ \left(J/kg-C\right)$	1910.7 (s), 2378.2 (l)[47]	1900 (estimated)
$\rho\ \left(kg/m^3\right)$	910 (s), 765 (l)[48]	1906 (estimated)
$k\ \left(W/m-C\right)$	0.21[48]	.47 (estimated)
$h_{sl}\ \left(J/kg-C\right)$	259,100 (DSC data)	N/A

The enthalpy of the solid to liquid phase change for the octacosane occurs over a temperature range as shown by the results of DSC measurements made by Triangle Research and Development Corporation, the supplier of the microPCM slurry. The original data was given as power vs temperature (shown as Fig. B-1 in App. B) and was therefore converted to an apparent specific heat vs. temperature using the sample weight and rate of temperature rise, the resulting graph is shown in Fig. 3-3, which also includes a curve fit of the actual data. The curve fit of the actual data was represented by the addition of two gaussian curves given as

$$f(T)=\frac{0.32L}{\sqrt{.845\pi}}\exp\left(\frac{-(T-59.1)^2}{.845}\right)+\frac{0.68L}{\sqrt{.98\pi}}\exp\left(\frac{-(T-62.8)^2}{.98}\right) \tag{3.15}$$

The first peak of the apparent specific heat curve corresponds to a solid to solid phase transition while the second peak corresponds to a solid to liquid transition; the total area beneath both peaks is the latent heat of phase transition. Each curve (DSC data and curve fit), see Fig. 3-3, represents 259.1 kJ/kg of latent heat, the latent heat for any temperature range within the phase change region may be found by the integration of the curve, $f(T)$. Integration of Eq. 3.15 within the melt region yields:

$$l=\left[41{,}456.0\,\mathrm{erf}\left(\frac{(T-59.1)}{\sqrt{.845}}\right)+88{,}094.0\,\mathrm{erf}\left(\frac{(T-62{,}8)}{\sqrt{.98}}\right)\right]_{T_s}^{T} \tag{3.16}$$

or in dimensionless form

$$f^*=\frac{f(T)}{Cp_b}=\frac{0.32}{\alpha_s\rho_p^*\mathrm{Ste}\sqrt{2\sigma_{ss}^{*\,2}\pi}}\exp\left(\frac{-(T^*-T_{ss}^*)^2}{2\sigma_{ss}^{*\,2}}\right)+\frac{0.68}{\alpha_s\rho_p^*\mathrm{Ste}\sqrt{2\sigma_{sl}^{*\,2}\pi}}\exp\left(\frac{-(T^*-T_{sl}^*)^2}{2\sigma_{sl}^{*\,2}}\right) \tag{3.17}$$

$$l^*=\frac{1}{\alpha_s\rho_p^*\mathrm{Ste}}\left[\frac{0.16}{\sqrt{2\sigma_{ss}^{*\,2}\pi}}\mathrm{erf}\left(\frac{(T^*-T_{ss}^*)}{\sigma_{ss}^*\sqrt{2}}\right)+\frac{0.34}{\sqrt{2\sigma_{sl}^{*\,2}\pi}}\mathrm{erf}\left(\frac{(T^*-T_{sl}^*)}{\sigma_{sl}^*\sqrt{2}}\right)\right]_0^{\theta} \tag{3.18}$$

Figure 3-4 is a graph of latent heat vs temperature, Eq. 3.16, within the melt range of octacosane, also shown, on the same graph, is the latent heat when a single melt temperature is assumed. The latent heat curve also clearly shows the solid to solid phase transition and the solid to liquid phase transition found in the DSC plot. In addition the slope of the latent heat curve is realated to the height of the apparent specific heat curve. For the current work the curve fit, Eq. 3.15, is used to calculate the apparent specific heat in all calculations.

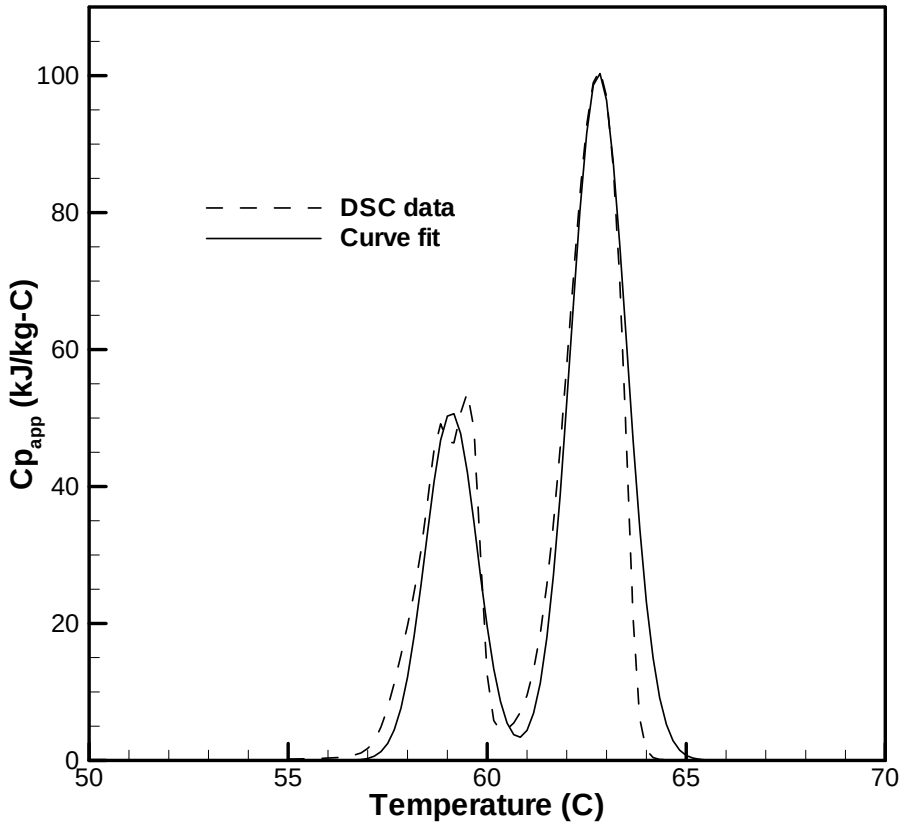

Figure 3-3 Octacosane apparent specific heat,DSC data and curve fit

The cooling of the bulk octacosane, Fig. B-2, does not follow the same curve as the heating cycle shown in Fig. B-1 of Appendix B, as discussed earlier this is common to other types of phase change materials and is referred as supercooling.[49, 50] The cooling cycle is similar to the heating cycle where two peaks are present but the curves are slightly different and shifted downward in temperature by about 5 ºC. Methods have been researched to reduce these supercooling effects in microPCM's.[49]

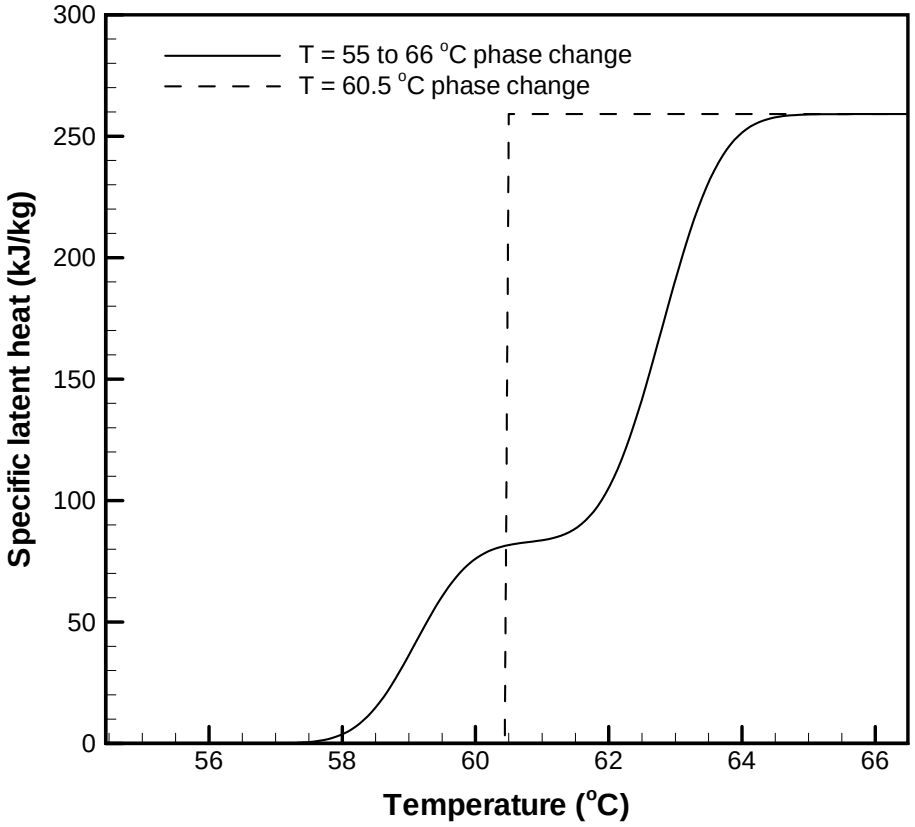

Figure 3-4 Bulk octacosane latent heat

3.3 Experimental verification

The experimental setup was verified by comparing the average wall temperature to a calculated average wall temperature using existing Nusselt correlations for single phase fluids. Both 50 / 50 (ethylene glycol / distilled water) mixture and pure distilled water were used as the single phase working fluid. The average wall temperature was used in the following correlations and is an integrated circumferential wall temperature at any axial location, which for the existing

experimental data is an average of the upper and lower external wall temperatures. A combined convection correlation was presented by Churchill[25]

$$\mathrm{Nu} = \left(\mathrm{Nu}_F^6 + \mathrm{Nu}_N^6\right)^{1/6} \tag{3.19}$$

where for natural convection[25]

$$\mathrm{Nu}_N = 0.847\mathrm{Ra}^{*0.177}\left[1.0 + \left(\frac{0.492}{\mathrm{Pr}}\right)^{9/16}\right]^{-0.315} \tag{3.20}$$

and for forced convection[51]

$$\mathrm{Nu}_F = 5.364\left[1.0 + \left(\frac{\mathrm{Gz}}{55.0}\right)^{10/9}\right]^{0.3} - 1.0 \tag{3.21}$$

In addition to the comparison of the experimental data to the Nusselt correlation, the data includes an attempt to quantify error by accounting for error in each measurement and using the methods of Kline and McKlintock,[52] Eq. 3-23, to estimate the overall error assuming the correlations of Eq.s 3.19-3.21 as a basis. Table 3-2 lists the error estimations for each of the measured values.

$$w_R = \pm\left[\left(\frac{\partial R}{\partial x_1} w_1\right)^2 + \left(\frac{\partial R}{\partial x_1} w_1\right)^2 + \ldots\right]^{1/2} \tag{3.22}$$

Table 3-2 Error estimation values

Dimension	+ / -	Units	Description
Axial Position	0.00655	m	Thermocouple end was .00635 m long in the direction of the tube axis
Diameter	0.00008	m	0.007747
Captured Volume	0.000005	m^3	Beaker tolerance
Temp	0.1	°C	Thermocouple tolerance
EG and Water Mixture Volume	0.00005	m^3	Beaker tolerance
Volts	0.047468	volts	1 std dev of measured data
Resistance	0.005	ohms	10 % of meter accuracy
time	0.403058	sec	1 std dev of a test of 20 measurements 100 ml volume using captured volume method of the experimental apparatus

Comparisons using both a 50/50 ethylene glycol/water mixture and water as the working fluid are made between the experimentally measured wall temperatures in this study and wall temperatures calculated using the correlations of Eq.s 3.15-3.17. Both dimensional and dimensionless plots are presented in Fig 3-3. In addition to the comparisons and error estimates energy conservation was verified using the measured inlet and outlet temperatures, mass flow rate,

and specific heat of the fluid. In each case energy was conserved to 94% or better. Table 3-3 summarizes the pure fluid experimental runs.

Table 3-3 Single phase test matrix

Fluid	Ra ($\times 10^6$)	Re	Pr	Gr ($\times 10^5$)	Gr / Re^2	Mdot ($\times 10^{-3}$) (kg/s)	q" (W/m^2)	Tin (°C)	Run #
50/50	0.79	285	19.3	0.41	0.50	4.10	4248.8	35.3	8-31_1
50/50	0.76	780	13.2	0.58	0.09	7.77	2733.1	52.6	8-31_7
50/50	4.0	663	12.6	0.32	0.72	6.33	13766.8	49.8	8-31_6
50/50	4.1	432	11.9	0.34	1.8	3.88	13257.2	49.7	8-31_3
50/50	4.1	333	12.4	0.33	3.0	3.12	13707.7	45.1	8-31_2
50/50	4.0	1063	11.6	0.34	3.1	9.32	12507.6	56.13	8-31_8
50/50	5.1	339	12.3	0.41	3.6	3.16	17108.7	42.6	8-25_2
Water	5.2	1177	3.0	1.7	1.3	3.32	13788.4	51.8	9-7_1

The first three experimentally measured and averaged tube wall temperatures, shown in Fig. 3-5a, are within the experimental error of the correlation data. The final five circumferentially averaged experimental data points are below the correlation and outside the range of experimental error, in addition the error appears to be increasing with axial position. Also, the final experimental data point appears to drop from the trend or slope of the previous points. Figure 3-5b shows the upper and lower wall temperature measurements for the water / glycol mixture. The upper and lower wall temperatures are within 1.5 °C of each other.

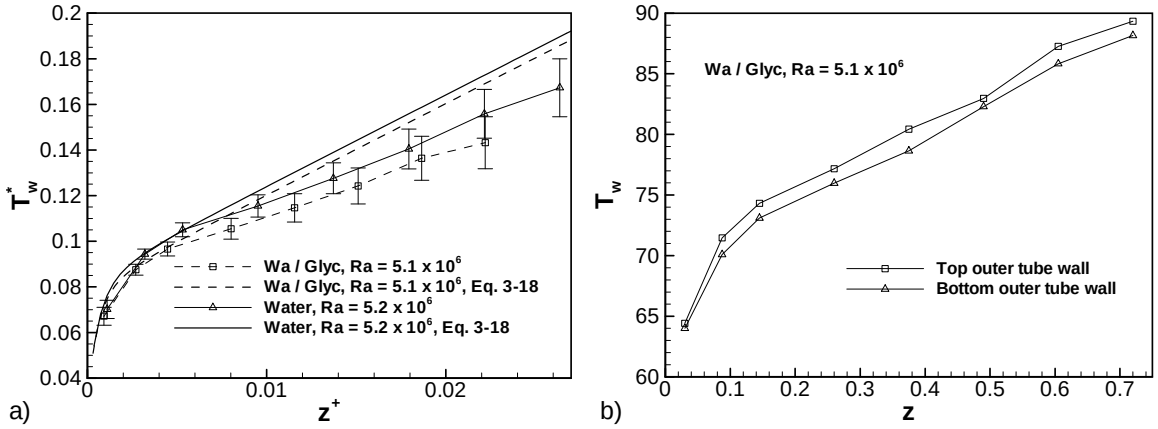

Figure 3-5 Experimental comparison a) dimensionless wall temperature and b) dimensional wall temperatures

The lower slope and resulting lower wall temperatures measured in the current experimental setup are attributed to two phenomena not accounted for in the Nusselt correlation of Eq. 3.15, circumferential heat transfer within the pipe wall and variable viscosity of the fluid. The correlations used for comparison were made using data with tube walls of stainless steel which has an order of magnitude lower thermal conductivity. The higher thermal conductivity of the copper in the current study caused heat to be transferred from the hotter tube top to the cooler bottom of the tube causing the lower average wall temperature. The stainless steel had less heat transferred circumferentially keeping the hot upper wall at a higher temperature. The relatively low temperature difference, approximately 1.5°C between the upper portion of the heated tube and lower portion indicate that the experimental apparatus is approaching the infinite circumferential heat transfer limit in which the wall would be one temperature. This is evident when compared to experimental results of previous experiments in which a temperature difference of 5 to 45°C[22] was found using a stainless tube with water as the working fluid. As noted earlier the first three experimental data points match the correlation because the effects of the forced convection

dominate in this region which also causes the top and bottom of the tube wall to be nearly the same temperature.

A correlating parameter for the wall effects in the steady state region for a mixed convection pure fluid flow has been given by Morcos and Bergles[53] as $\frac{k_l}{k_w}\frac{D}{\Delta}$ and tested within the parameter range of 2 to 66. A Nusselt correlation for free convection in the fully developed region was found.[26]

$$Nu_l = \frac{0.42 Gr_l^{0.28} \Pr_l^{0.33}}{\frac{k_l D}{k_w \Delta}} \qquad 3.23$$

As the correlating parameter becomes greater there is less circumferential wall conduction, the circumferential average Nusselt number decreases, and the temperature difference between the top and bottom of the tube wall becomes greater. For the current application the parameter was nominally .0044, this is outside the range of applicability of Eq. 3.23. However, it is approaching the limit of infinite circumferential wall conduction which would be a parameter value of zero, thus higher Nusselt numbers and lower average wall temperatures would be expected. The correlation given by Eq. 3.23 fails at the infinite conduction limit and therefore a new correlation would be needed for the copper wall material, but this is outside the scope of the current work and only mentioned here.

The viscosity effects were investigated by using pure distilled water and comparing the wall temperatures to that of the 50 / 50 mixture. The viscosity changes for both fluids are plotted in Fig 3-6 and show the pure water has a lower viscosity change over the same temperature range. The variable viscosity effects are not as great as the circumferential heat transfer effects, but should be kept in mind when working with fluids of highly temperature dependent viscosities.

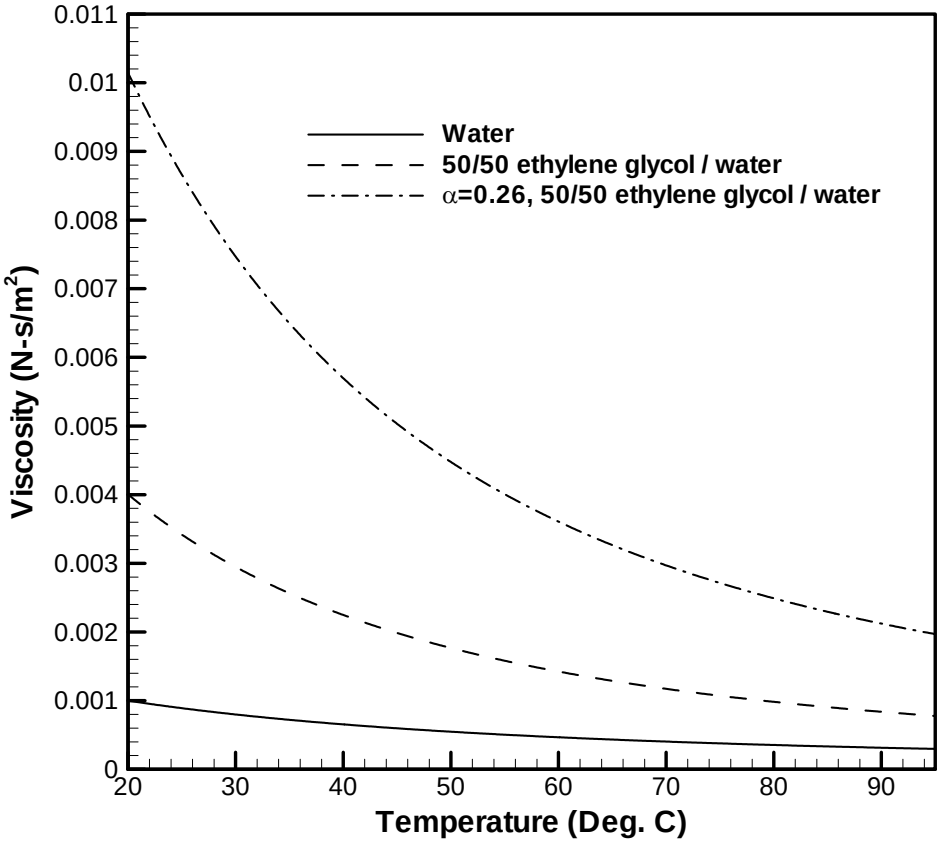

Figure 3-6 Fluid viscosities

The change in slope of the last experimentally measured position was due to the influence of the end conditions, Fig. 3-7, of the experimental setup. In the experimental set up the adiabatic end connection was a plastic fitting connected over the tube wall. The plastic fitting did not allow the constant wall heat flux condition to be continued to the end of the pipe. The unheated tube end caused axial conduction from the last measurement point to the unheated tube end connection. To check if this phenomena affected more than the last measured point the fluid flow rate was changed from high to low while maintaining a constant Rayleigh number. The high flow rate corresponds to a thermally shorter length than the lower flow rate. The difference in thermal

lengths is observed as dimensionless tube lengths in Fig. 3-8, in which the dimensionless tube wall temperatures were shown as a function of dimensionless tube lengths. As the dimensionless length is reduced the end effects are more pronounced. If the end condition affects more than the last point the temperature at that point will deviate from the curve.

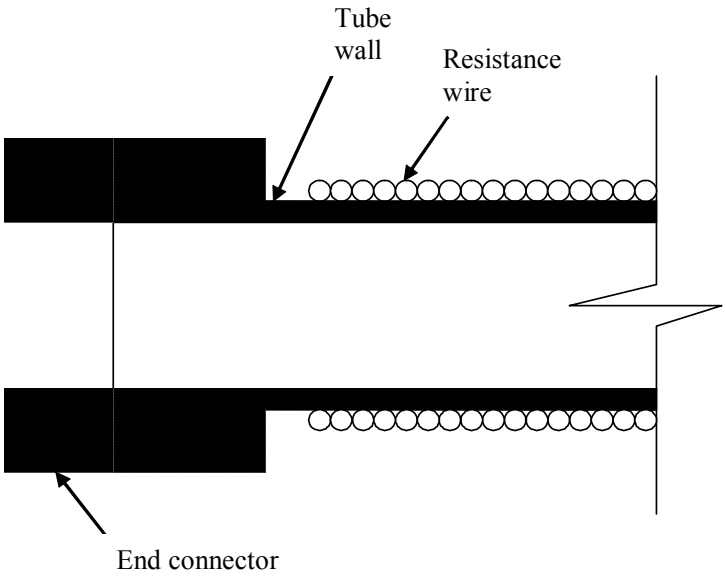

Figure 3-7 Typical inlet / outlet connection section

Because only the last experimentally measured point deviated from the curve formed by the multiple dimensionless length experimental runs the experimental setup tube end condition was shown to only affect the final measured point, as seen in Fig. 3-8. The effects on the final measured point increased as the dimensionless length decreased. In addition to the experimental data numerical results (numerical methods discussed in Chapter 4) are presented in Fig. 3-8 and verify these single phase fluid results. Also shown are analytic results of a flow with $\mathrm{Ra} = 0$. The results of the analytic comparison show the dimensionless wall temperatures to be lower in temperature after a short region and are of similar temperature at the tube entrance. This is typical

of mixed convection in tubular flow in which the fully developed region occurs sooner and makes a shorter thermal entrance region than pure forced convection; this is discussed further by Petkuhov[22] and Ouzzane.[29]

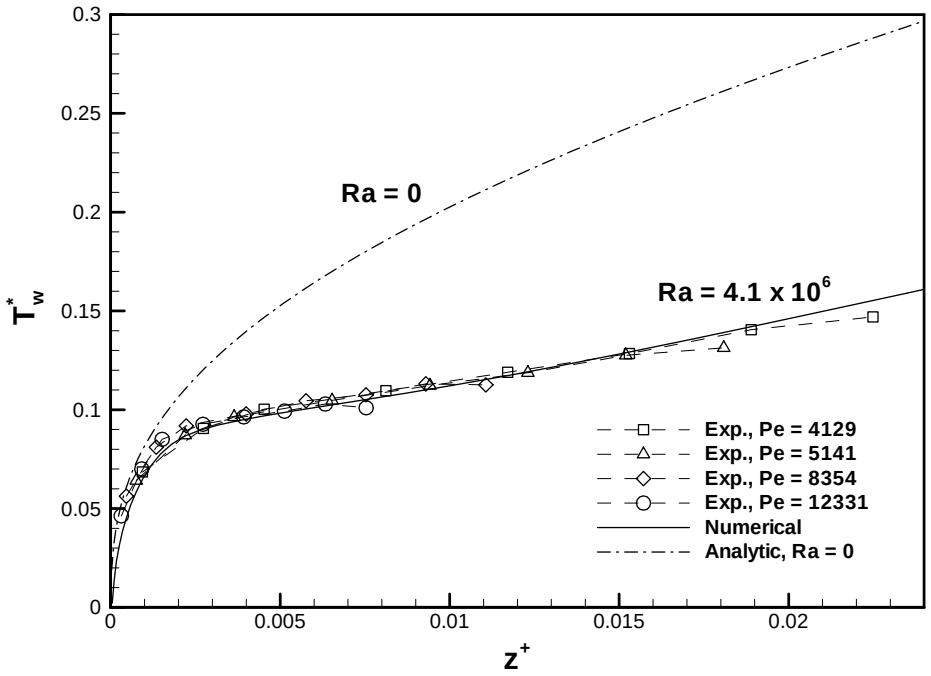

Figure 3-8 Experimental setup end effects

3.4 Experimental Results and Discussion

The addition of the microPCM particles increases the viscosity of the fluid which is estimated by Eq. 2.38 and plotted over the temperature range for the microPCM used in the current work in Fig. 3-6. Also the microPCM particles can enhance heat transfer when the operating temperature is within the melt range of the PCM and melting of the particles occurs. First the fluid and particle mixture or slurry was investigated with no phase change occurring by applying a maximum

amount of power but still maintained the maximum tube wall temperature to 45°C which is below the start of the phase change of octacosane. The results are presented in Fig. 3-9 and are shown for similar Rayleigh numbers for a single phase fluid (50 / 50 ethylene glycol water mixture) and the slurry made of a 50 / 50 ethylene glycol water mixture with 23 % by mass addition of microPCM particles both with and without phase change. The dimensionless length was again varied to check the end effects of the experimental setup which, like the single phase fluid, were found to only affect the final measured position. The addition of the microPCM particles causes additional heat transfer enhancement over the single phase liquid flow, as seen in Fig. 3-9, in which single phase flow dimensionless tube wall temperature were presented along with the two phase results. The heat transfer enhancement was evident even though the single phase flow has a Rayleigh number 1.46 times that of the two phase flows. This causes the single phase fluid Nusselt correlations to be invalid for two phase mixed convection thermal predictions because of the neglected effects of the solid particles suspended in the fluid.

Table 3-4 Two phase test matrix

Ra_f ($\times 10^6$)	Ra_b ($\times 10^6$)	Ste	Re_b	Pr_b	Gr_b ($\times 10^5$)	Gr_b/Re^2	Mdot ($\times 10^{-3}$) (kg/s)	q" (W/m^2)	Tin (°C)	Run #
3.1	1.5	10.8	424	30.3	0.50	0.27	9.01	9598.4	58.9	9-24_1
4.2	2.1	13.3	201	27.4	0.77	1.90	3.90	11857.4	58.8	9-24_4
5.6	2.7	18.8	418	29.3	0.92	0.53	8.62	16682.9	58.9	9-24_3
4.0	1.9	12.8	228	28.2	0.67	1.30	4.54	11411.1	58.9	9-25_2
1.1	0.53	7.6	464	52.1	0.10	0.047	1.69	6340.0	33.9	9-26_2
0.97	0.46	6.5	276	55.4	0.083	0.11	1.06	5653.8	33.8	9-26_1
1.0	0.50	3.6	384	28.7	0.018	0.12	7.79	3211.3	58.9	9-26_6
3.8	1.9	12.8	285	29.1	0.065	0.80	5.85	11365.5	58.9	9-30_1

The inlet temperature of the two phase fluid was then increased to nominally 58.85 ºC which was within the melting region of the octacosane. These results, at the same Rayleigh number of the non-melting case, are presented in Fig. 3-9. The enhanced heat transfer due to melting is clearly evident. The 58.85°C inlet temperature was chosen from the DSC data presented in Fig. 3-3, which indicated that the peak of energy storage due to melting was at 62.8°C which would cause the greatest heat transfer enhancement. This inlet temperature was maintained for the remainder of the experimental work. A summary of the experimental conditions is summarized in Table 3-4.

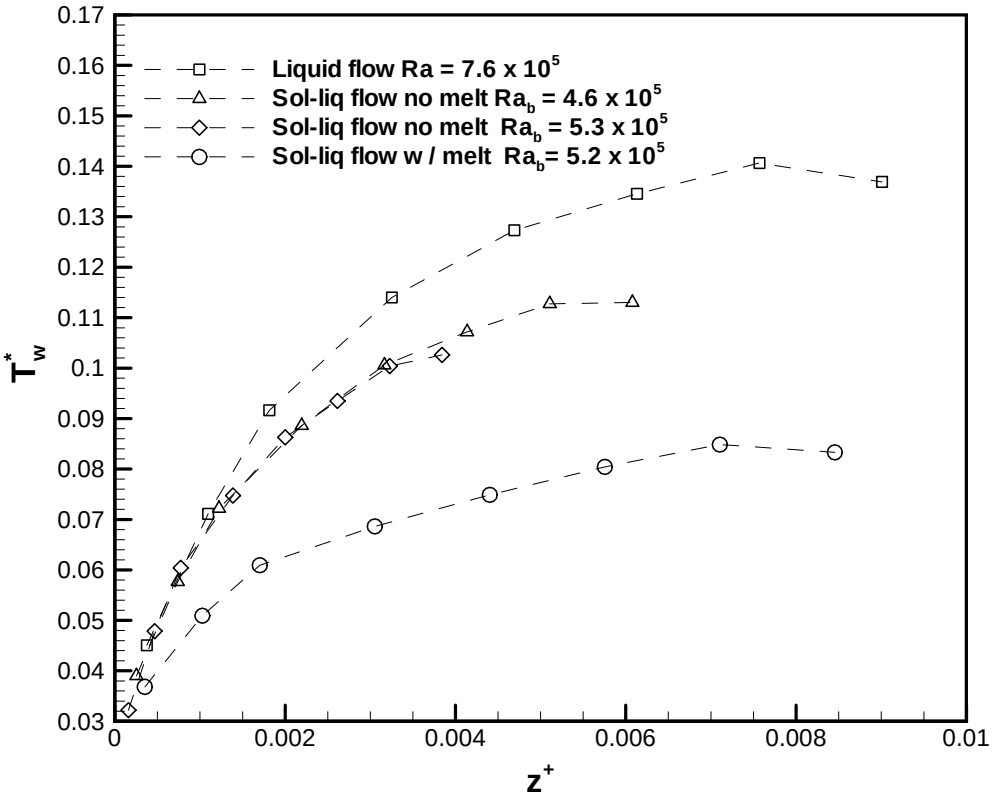

Figure 3-9 PCM particle addition effects

3.4.1 Varying the Mass flow rate

As seen in Fig. 3-10 increasing the slurry mass flow rate through the heated section, while maintaining the Rayleigh and Stefan numbers nearly constant, causes the dimensionless length to decrease and the dimensionless tube wall temperature to decrease, this is in contrast to that of the single phase fluid with no microPCM particles, Fig. 3-8, and two phase flow with no phase change, Fig 3-9.. There are two causes of the difference.

1) Because the mass flow rate was higher the fluid and PCM had a lower temperature rise at the same dimensionless axial position versus the lower mass flow rate. The lower temperature rise of the PCM meant there was less latent heat stored at a dimensionless axial position and since a similar amount of energy was added the fluid temperature at the wall was higher. A second way of looking at this is that the apparent specific heat of the slurry, Fig. 3-3, at the peak is approximately 5 times that of the bulk fluid specific heat, this large property variation causes the curves to behave different when compared to the results of the single phase fluid, Fig. 3-8, or the solid liquid flow with no melting, Fig. 3-9.
2) The bulk cooler outlet temperature measured by TC-12, Fig.3-1, was only reduced to 56.8 ºC, which was not low enough to complete the cooling phase change, see Fig. B-2, and thus latent heat below 56.8 ºC was unavailable as energy storage.

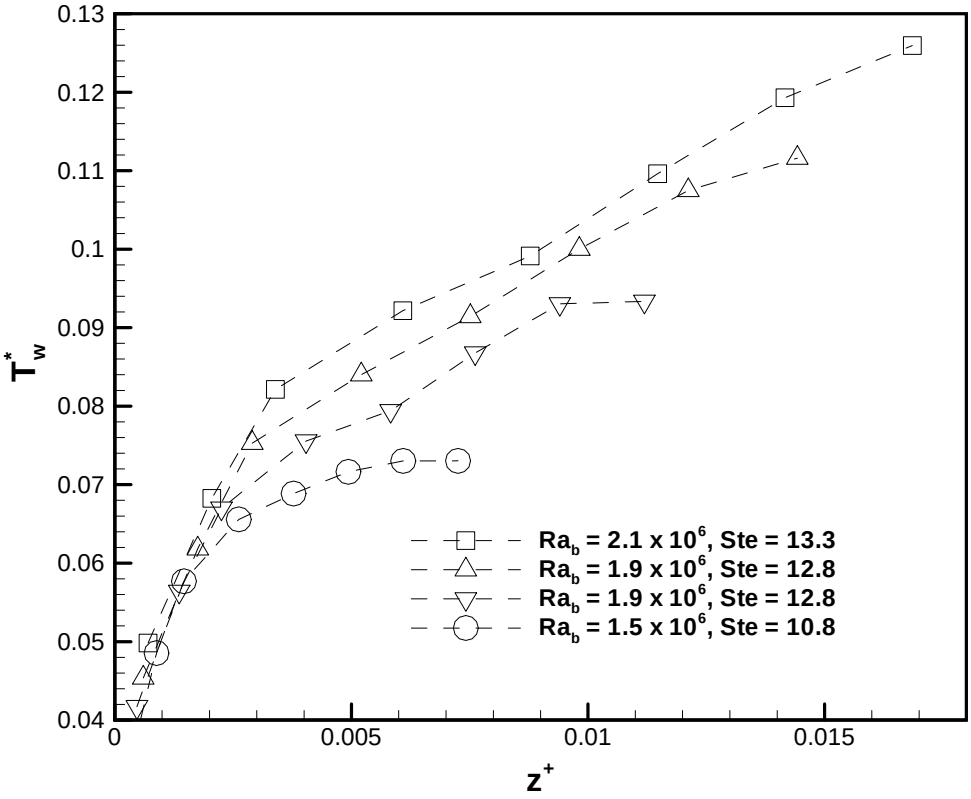

Figure 3-10 Flow rate variation

3.4.2 Rayleigh and Stefan numbers

Two dimensionless parameters which the tube wall temperatures are dependent are the Rayleigh and Stefan numbers. Because these two dimensionless parameters are both dependent upon the heat flux which in the current experimental apparatus is the only experimentally controlled quantity, upon which both parameters are dependent, that is able to be varied, a thorough investigation of the interaction of these two parameters was not possible. However, within the limitations of this experimental set up some observations are made.

The Rayleigh and Stefan numbers were varied using the heat flux, of which both are dependent to the first power, to establish the effects on the tube wall temperatures for the microPCM slurry

the extreme cases are presented in Fig.3-11. For the two experimental conditions of Fig. 3-11 the heat flux differed by a factor of 5.2 while the Rayleigh and Stefan numbers differed by factors of 5.4 and 5.2 respectively. The slight variation with the Rayleigh number is due to a difference in the temperature dependent viscosity which the Rayleigh number is dependent upon to the second power and the Stefan number is not dependent upon.

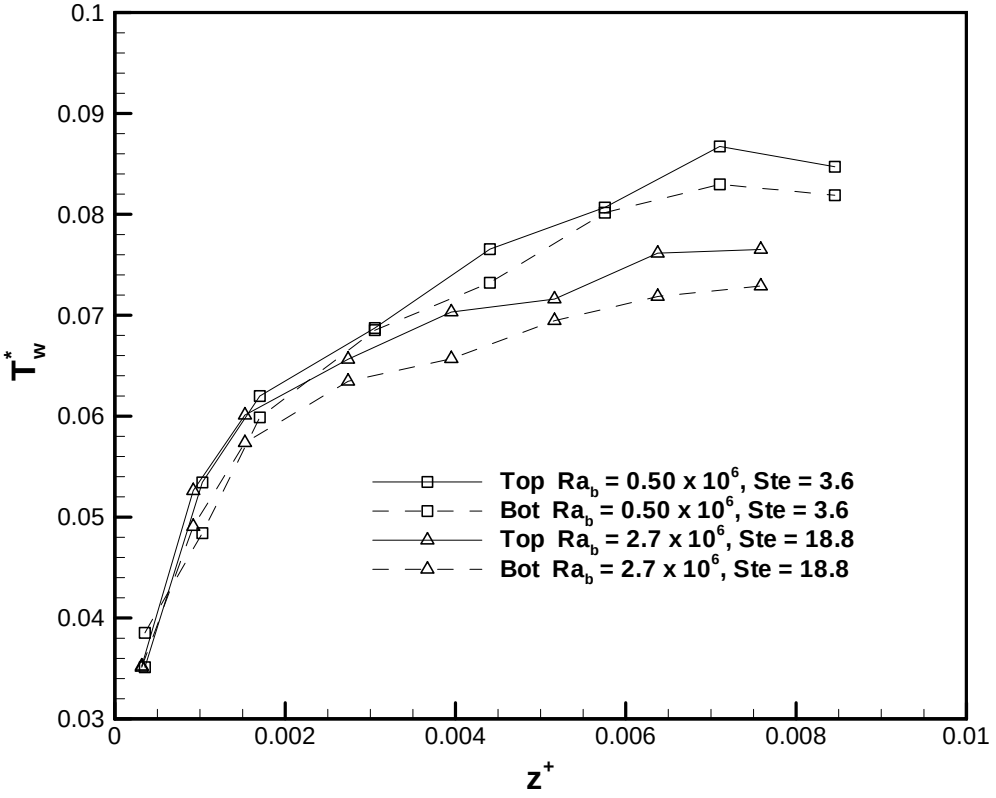

Figure 3-11 Experimental upper and lower tube wall temperatures

These two parameters are competing in that as the Stefan number is raised the dimensionless wall temperature is expected to increase as can be easily seen in the upper limit where there is no phase change when the Stefan number approaches infinity. Where as, the increase of the Rayleigh number tends to decrease the dimensionless wall temperature due to increased buoyancy induced

secondary flow. For the range of Rayleigh and Stefan numbers presented in Fig. 3-11 the effects of the Rayleigh number are dominant, after the dimensionless length of 0.0025, causing the dimensionless tube wall temperature to be lower. At the inlet of the tube, 0.0 – 0.0025, the effects of the forced convection are dominant overshadowing free convection effects as was discussed for single phase flows. In this inlet region it was therefore expected the lower Stefan number case would have the lower wall temperature but the data was too close in temperature draw that conclusion. Under the conditions of this experiment the free convection effects, causing lower dimensionless wall temperatures were greater than the increased Stefan number effects, which alone would cause a rise in dimensionless wall temperature. This may not be the case in other combinations of Stefan and Rayleigh numbers but these were outside the capabilities of the current experimental apparatus.

4 NUMERICAL PROCEDURES

4.1 Grid

For the cylindrical coordinate system of the tubular flow condition considered an uneven grid was used which was clustered to the tube wall in the radial direction and to the tube inlet in the axial direction to better resolve the higher gradients expected in these two regions. The circumferential direction used an evenly spaced grid. The following equation was used for the grid generation[54] in both the radial and axial directions.

$$r^* = 0.5 - \frac{0.5*(\beta+1)-(\beta-1)\left\{\left[(\beta+1)/(\beta-1)\right]^{1-\bar{y}}\right\}}{\left[(\beta+1)/(\beta-1)\right]^{1-\bar{y}}+1} \qquad 4.1$$

$$z^* = L^* \frac{(\beta+1)-(\beta-1)\left\{\left[(\beta+1)/(\beta-1)\right]^{1-\bar{y}}\right\}}{\left[(\beta+1)/(\beta-1)\right]^{1-\bar{y}}+1} \qquad 4.2$$

where $\bar{y}$ is the position for an evenly spaced grid and β is chosen such that $1 < \beta < \infty$. Equation 4.1 clusters points towards the inner tube wall in the flow region and the tube inlet in both the flow and tube wall regions as β approaches 1. The current application used $\beta = 1.1$ for the radial direction and $\beta = 1.1$ for the axial direction. An evenly spaced radial grid was used for the tube wall radial direction and for the circumferential direction. The same circumferential and axial grids used in the flow region were used within the tube wall. Figure 4-1 is an example of the $r^* - \theta$ grid used (the tube wall is represented by the thicker lines).

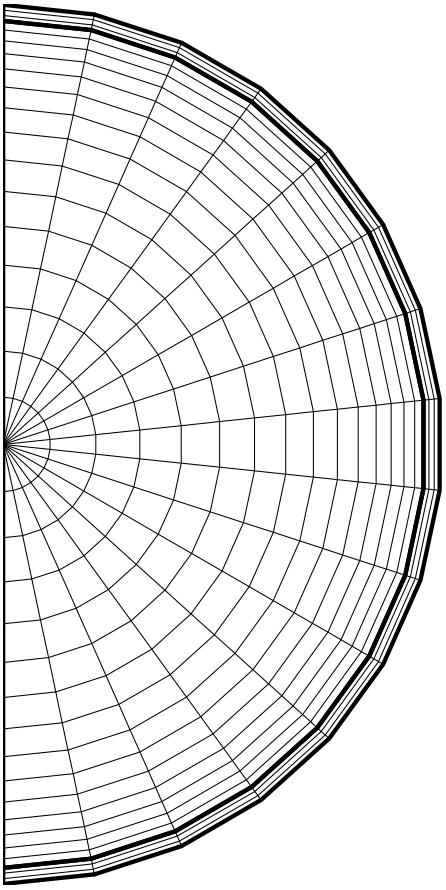

Figure 4-1 Tube section - fluid and wall grid

The final grid size within the fluid region was 16 x 16 x 20-120, where the axial direction depended upon the dimensionless length. The tube wall consisted of 6 radial cells with the axial and circumferential directions being equal to the fluid region.

4.2 Two phase flow solution procedure

To solve the governing equations Eq. 2.11-2.15 the SIMPLER method[55] was used by first modifying the method to handle the two interacting fluids of the two phase flow. The grid / mesh layout was as described in section 4.1 and the variables were solved on a staggered mesh with velocities solved at cell boundaries and all scalar variables were solved at cell centers, as shown for the radial and circumferential directions in Fig. 4-2. In addition all thermodynamic properties were calculated at the cell centers.

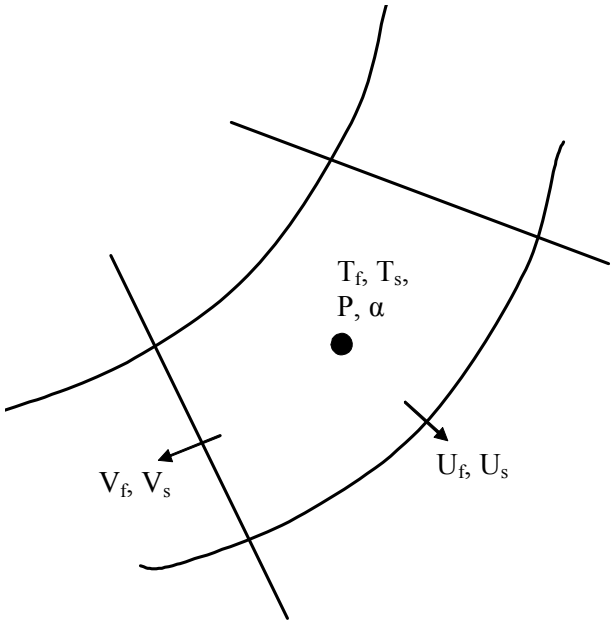

Figure 4-2 Typical cell and variable locations

The following solution description is based on the SIMPLER method[55] and only equations needed for the two phase aspect, which are different than the SIMPLER method, of the current study are presented. The solution method begins with a guessed initial velocity field for each phase. A pseudo velocity, in which the differential pressure term is neglected, is calculated for

both phases. To solve the pressure field the discretized liquid mass conservation equation, Eq. 2-11, is used by substituting the pseudo velocities of the liquid phase into the discretized mass conservation equation, resulting in a set of equations with pressure as the unknown. Solving this set of equations results in a pressure field that is shared by both the liquid and solid phases. This method follows the SIMPLER method for single phase flow and has been used in other numerical investigations.[56] Now with the pressure field solved the discretized momentum equations, shown below in a general form, may be solved for the velocity field of each phase.

$$a_{P,l}\phi_{P,l} = \sum a_{i,l}\phi_{i,l} - \lambda\left(\phi_{P,l} - \phi_{P,s}\right) + \alpha_l \Delta p + s_{P,l} \tag{4.3}$$

$$a_{P,s}\phi_{P,s} = \sum a_{i,s}\phi_{i,s} - \lambda\left(\phi_{P,s} - \phi_{P,l}\right) + \alpha_s \Delta p + s_{P,s} \tag{4.4}$$

As discussed in Chapter 2 the interphase coupling between the solid and liquid phases is completed in the second term on the right hand side of Eq. 4.3, where lambda represents the interphase coupling term. As an example of a typical computational cell the liquid phase of the radial direction momentum equation, Eq. 2-12, is discretized. The computational cell of concern is shown in Fig. 4-3, where dashed lines being the cell boundary and solid lines are representing the computational grid.

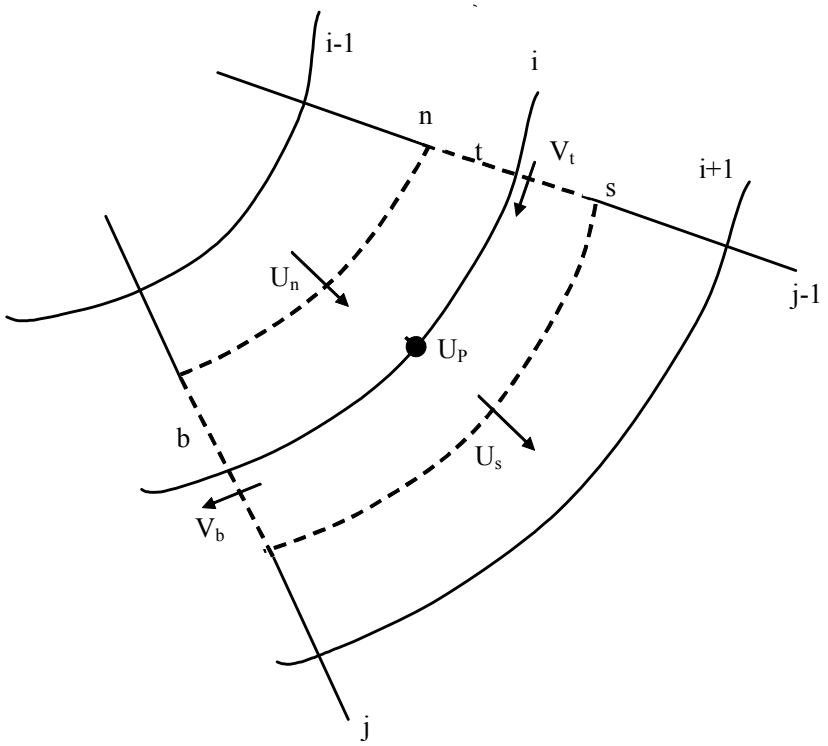

Figure 4-3 Typical cell layout for the radial momentum equation

The coefficient values to be used in Eq. 4.3 for the radial component of the liquid momentum equation, Eq. 2-12, are

$$a_{P,l} = a_{n,l} + a_{s,l} + s_{P,l} + \Delta\forall \max\left[0,\ -\frac{\left(\alpha_l \mu_l^*\right)_P}{r_P^{*2}}\right] \tag{4.5}$$

$$a_{n,l} = D_n \times \max\left[0,\ \left(1.0 - 0.1F_n / D_n\right)^5\right] + \max\left[F_n,\ 0\right] \tag{4.6}$$

$$a_{s,l} = D_s \times \max\left[0,\ \left(1.0 - 0.1F_s / D_s\right)^5\right] + \max\left[-F_s,\ 0\right] \tag{4.7}$$

$$F_n = \rho_l^*\ \alpha_{l,i}\ r_n^*\ \Delta\theta\ \Delta z\ U_n \tag{4.8}$$

$$F_s = \rho_l^*\ \alpha_{l,i+1}\ r_s^*\ \Delta\theta\ \Delta z\ U_s \tag{4.9}$$

$$D_n = \left(\mu_l^* \alpha_l\right)_n r_n^*\ \Delta\theta\ \Delta z\ \ / \Delta r_n \tag{4.10}$$

$$D_s = \left(\mu_l^* \alpha_l\right)_s r_s^*\ \Delta\theta\ \Delta z\ \ / \Delta r_s \tag{4.11}$$

$$\lambda = \Delta\forall K_{ls}^* \tag{4.12}$$

$$\Delta p = \Delta\forall\, \mathrm{Re}_b^2\, \frac{p_i - p_{i+1}}{\Delta r^*} \tag{4.13}$$

$$\begin{aligned} s_{P,\,l} = \Delta\forall \Bigg\{ & \left(\alpha_l \mathrm{k}_l^* \rho_l^* \nu_{l\,\mathrm{in}}^{*2}\ \right)_P \mathrm{Gr_l T_P^*} \cos\theta_P + \left(\alpha_l\ \alpha_s \rho_l^* \nu_{l\,in}^{*2}\right)_P d_p^{*3}\, \mathrm{Ar} \cos\theta_P \\ & - G_b^*\, \mathrm{Re}_b^2\, \frac{\Delta\left(\alpha_s\right)}{\Delta r^*} + \frac{1}{r_P^*} \frac{\Delta\left(\alpha_l \mu_l^* r^* \dfrac{\Delta U_l}{\Delta r^*}\right)}{\Delta r^*} + \frac{U_{P,l}}{r_P^*} \frac{\Delta\left(\alpha_l \mu_l^*\right)}{\Delta r^*} \\ & - \max\left[0,\ \frac{\left(\alpha_l \mu_l^* U_l\right)_P}{r_P^{*2}}\right] + \frac{1}{r_P^{*2}} \frac{\Delta\left(\alpha_l \mu_l^* \dfrac{\Delta U_l}{\Delta\theta}\right)}{\Delta\theta} - \frac{2}{r_P^{*2}} \left(\alpha_l\ \mu_l^*\right)_P \frac{\Delta V_l}{\Delta\theta} \\ & + \alpha_{P,l} \frac{V_{P,l}^2}{r_P^*} \Bigg\} \end{aligned} \tag{4.14}$$

where the diffusive coefficients were calculated using the geometric mean as recommended by Pantakar,[55] the variables were linearly interpolated to cell center or cell face as needed, $\Delta\forall$ is the

cell volume, and the $a_{P,l}$ coefficient was written to maintain a positive value, the notation $\max[0\ ,(\ )\ ]$ was used to select only positive values. In addition the power law scheme[55] was used to calculate the diffusive fluxes. The other coordinate directions are similarly discretized.

The pressure field was based on the initial guessed velocities; a new velocity field is then calculated using Eq.s 4.3 and 4.4. The resulting velocity field however, does not satisfy the conservation of mass and therefore similar to the SIMPLER method a pressure equation based only on the liquid mass continuity was used to derive a pressure correction equation. The pressure equation was solved and the results used to correct the velocity fields of both phases using equations of the form (the details may be found in Ref. 55).

$$u_s = u_s^* + \frac{A_s}{a_{P,s}}\left(p_i - p_{i+1}\right) \tag{4.15}$$

where the nomenclature of Ref. 55 was used.

Using the most recently calculated pressure and velocity fields the concentration of the two phases may now be calculated by solving the solids mass conservation equation, Eq. 2.11, for the solids volumetric concentration. Then using the fact that the volumetric concentrations of the two phases sum to unity the liquid concentration may be found as

$$\alpha_l = 1.0 - \alpha_s \tag{4.16}$$

To solve for the solids concentration derivatives of the incompressible mass conservation equation, Eq. 2.11, were expanded and after rearranging

$$U_s \frac{\partial \alpha_s}{\partial r^*} + \frac{V_s}{r^*}\frac{\partial \alpha_s}{\partial \theta} + W_s \frac{\partial \alpha_s}{\partial z^*} = -\alpha_s\left[\frac{1}{r^*}\frac{\partial}{\partial r^*}\left(r^* U_s\right) + \frac{1}{r^*}\frac{\partial}{\partial \theta}\left(V_s\right) + \frac{\partial}{\partial z^*}\left(W_s\right)\right] \tag{4.17}$$

The upwinding method was used to discretize Eq. 4.17 which resulted in an equation of the form

$$a_{P,s}\,\alpha_{P,s} = \sum_{nb} a_{i,s}\,\alpha_{i,s} + s_{P,s} \qquad 4.18$$

where the coefficient definitions for the upwinding method are similar to the discretized radial momentum equation presented earlier by Eq.s 4.5 – 4.14. The resulting set of equations was solved for the solids concentration using the Thomas algorithm. Now with the solids volumetric concentration known Eq. 4.16 was used to find the liquid volumetric concentration. The velocities and concentrations are now known and therefore the temperature field of each phase can be solved using the discretized form of the energy equations, which are also of the form of Eq.s 4.2 and 4.3 excluding the pressure term. The method just described is the inter phase slip algorithm (IPSA).[57] Specific issues with two phase flow solution procedure and the current application will be discussed in sections 4.2.1 to 4.2.3.

4.2.1 PEA

To increase the convergence rate of the above iterative procedure the partial elimination algorithm (PEA)[58] was implemented. The general form of a discretized conservation equation given by Eq.s 4.3 and 4.4 is the starting point where phi may be either a component of the velocity field or the temperature depending upon the conservation equation being solved, but only the momentum equations involving the velocity contain the pressure gradient term, and lambda represents the exchange coefficient between the two phases. Rearranging Eq.s 4.3 and 4.4 yields

$$\left(a_{P,l} + \lambda\right)\phi_{P,l} = \sum a_{i,l}\phi_{i,l} + \lambda\phi_{P,s} + \alpha_l \Delta p + s_{P,l} \qquad 4.19$$

$$\left(a_{P,s} + \lambda\right)\phi_{P,s} = \sum a_{i,s}\phi_{i,s} + \lambda\phi_{P,l} + \alpha_s \Delta p + s_{P,s} \qquad 4.20$$

Solving for both the liquid and solid phase variables of Eq.s 4.19 and 4.20

$$\phi_{P,l} = \frac{\sum a_{i,l}\phi_{i,l} + \lambda\phi_{P,s} + \alpha_l \Delta p + s_{P,l}}{\left(a_{P,l} + \lambda\right)} \tag{4.21}$$

$$\phi_{P,s} = \frac{\sum a_{i,s}\phi_{i,s} + \lambda\phi_{P,l} + \alpha_s \Delta p + s_{P,s}}{\left(a_{P,s} + \lambda\right)} \tag{4.22}$$

The solution of the solid phase variable, phi from Eq. 4.22, is now substituted into the liquid phase equation, Eq. 4.21, thus eliminating the current solid phase variable from the solution for the liquid phase variable. Similarly the solution of the liquid variable is then substituted into the solid phase variable solution. After rearranging and adding relaxation the following equations result

$$\begin{aligned}\left(1+1/E\right)\left[a_{P,l} + \frac{\lambda}{\left(a_{P,s}+\lambda\right)}a_{P,s}\right]\phi_{P,l} = \\ \sum a_{i,l}\phi_{i,l} + \alpha_l \Delta p + s_{P,l} + \frac{1}{E}\left[a_{P,l} + \frac{\lambda}{\left(a_{P,s}+\lambda\right)}a_{P,s}\right]\phi^o_{P,l} \\ + \frac{\lambda}{\left(a_{P,s}+\lambda\right)}\left[\sum a_{i,s}\phi_{i,s} + \alpha_s \Delta p + s_{P,s}\right]\end{aligned} \tag{4.23}$$

$$\begin{aligned}\left(1+1/E\right)\left[a_{P,s} + \frac{\lambda}{\left(a_{P,l}+\lambda\right)}a_{P,l}\right]\phi_{P,s} = \\ \sum a_{i,s}\phi_{i,s} + \alpha_s \Delta p + s_{P,s} + \frac{1}{E}\left[a_{P,s} + \frac{\lambda}{\left(a_{P,l}+\lambda\right)}a_{P,l}\right]\phi^o_{P,l} \\ + \frac{\lambda}{\left(a_{P,l}+\lambda\right)}\left[\sum a_{i,l}\phi_{i,l} + \alpha_l \Delta p + s_{P,l}\right]\end{aligned} \tag{4.24}$$

where E is defined by Van Doormal and Raithby[59] as

$$E = \frac{\omega}{1-\omega} \tag{4.25}$$

Equations 4.23 and 4.24 are then solved iteratively, described in section 4.2.4, for the unknown variable phi. The PEA method was used to solve the momentum and energy equations, Eq.s 2.12 - 2.15.

4.2.2 Concentration Equation solution modifications

In two phase flows each phase has a maximum limit which may be as high as 1.0 when only a single phase is present at a particular location. During the solution of the concentration equation the upper limit is not bounded and can be exceeded causing physically unrealistic solutions or divergence. Several methods have been proposed to solve this problem.[60, 61]

When solving the momentum equations, Eq. 2.12 – 2.14, the particle-particle interaction force or solids pressure term G is calculated using the correlation given by Eq. 2.36 and a plot of G versus particle volumetric concentration is shown in Fig 4-4. When the concentration of the solids phase is at the compaction limit $\left(\alpha_{\max} = 0.624\right)$ Eq. 2.34 gives $G = 1$, above the limit the value quickly grows which causes a large source term in the momentum equation and limits the particle concentration at any particular location. When the particle concentration is above the compaction limit the large value of G can cause the iterative solution to diverge. An effective method of preventing divergence while solving for the particle concentration was presented by Carver[61] and was successfully implemented by Zhang et al.[62] The method first calculates the a preliminary particle concentration of Eq. 4.18 at each computational grid location in point Jacobi form giving

$$\alpha_{P,s} = \frac{\sum_{nb} a_{i,s}\,\alpha_{i,s} + s_{P,s}}{a_{P,s}} \tag{4.26}$$

Then if $\alpha_{P,s} > 0.59$ at any grid point a local relaxation factor for the solid phase concentration at that grid point is set to the minimum value of $\left(\alpha_{\max,s} - \alpha_{P,s}\right)$ and 10^{-10} or in equation form $\omega = \max\left[\left(\alpha_{\max,s} - \alpha_{P,s}\right), 10^{-10}\right]$ is used resulting in the following equation

$$\alpha_{P,s} = \frac{\sum_{nb} a_{i,s}\,\alpha_{i,s} + s_{P,s} + \dfrac{\alpha_{P,s}^{old}}{E}}{a_{P,s}\left(1 + 1/E\right)} \qquad 4.27$$

Now using the local value of relaxation Eq. 4.17 is solved for the particle concentration using Eq. 4.28. This method allows the concentration and momentum equations to be solved iteratively for the concentration without causing divergence.

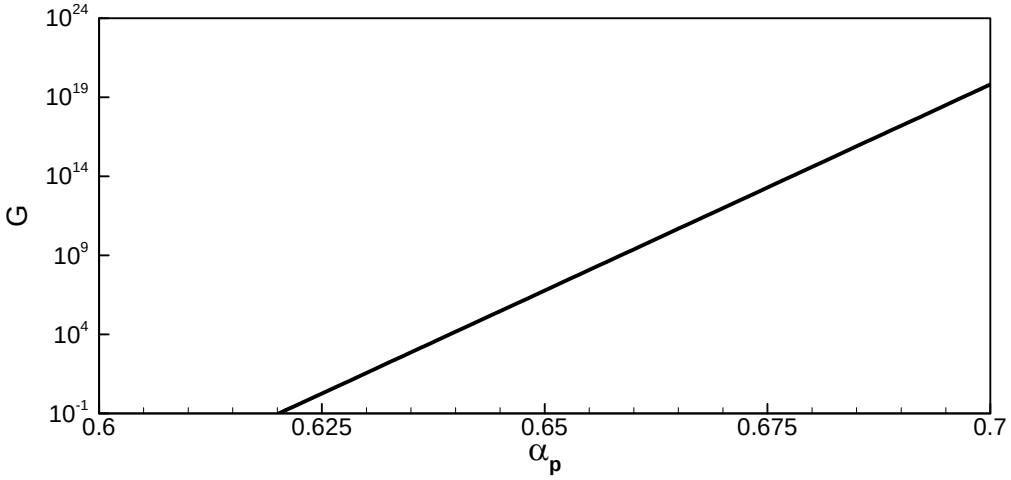

Figure 4-4 Particle - particle interaction force

4.2.3 Tube wall solution

As was presented in Section 2.4.2 the axial conduction within the tube wall was not considered however, the circumferential conduction within the tube wall was considered. The second term in Eq. 2.16 accounts for the circumferential heat conduction. The inclusion of the circumferential conduction was found to be significant in studies such as the numerical work of Ouzzane and Galanis,[29] and is expected to be significant here due to the highly conductive copper wall and therefore it will be included here. This conjugate problem was solved using the appropriate wall boundary conditions of Eq.s 2.17 – 2.25. The velocity within the wall was not solved but set to

zero. During the solution of the liquid phase energy equation the temperature distribution was solved using Eq. 2.15. The tube wall temperature was solved along with the fluid temperature due to the interfacial boundary condition requiring all thermal energy transport is to the liquid phase as described in Chapter 2.

At the fluid – wall interface a large jump in thermal conductivity occurred and was solved by taking the harmonic mean of the two thermal conductivities.[55] A formula for the harmonic mean is found by considering Fouriers law of conduction between two cells of different size and conductivity. The steady state 1-D heat transfer may be written as

$$q'' = -k_{eff}\frac{dT}{dn} = \frac{T_2 - T_1}{\frac{\Delta n_1}{k_1} + \frac{\Delta n_2}{k_2}} \tag{4.28}$$

and solving for the effective thermal conductivity

$$k_{eff} = \frac{\Delta n k_1 k_2}{\Delta n_1 k_2 + \Delta n_2 k_1} \tag{4.29}$$

where Δn1 and Δn2 are the distance from the respective cell center to the interface. The computational cell interface during the solution of the energy equation is at the fluid-wall interface.

A local Nusselt number at a given circumferential and axial position is given by

$$\mathrm{Nu}_\theta = \frac{1}{T^*_{w,\theta} - T^*_b} \tag{4.30}$$

with a circumferential average Nusselt number defined as

$$\mathrm{Nu}_{avg} = \frac{1}{\frac{1}{\pi}\int_0^\pi T^*_{w,\theta}\, d\theta - T^*_b} \tag{4.31}$$

where the bulk temperature is found using the bulk energy flow within the fluid at an axial cross section.

$$T_b = \frac{\int_{A_c} \rho w Cp T dA_c}{\dot{m} Cp} \qquad \text{Eq 4.1}$$

Now using an iterative solution procedure the variables of both the fluid and tube wall regions may be solved.

4.2.4 Iterative procedure

The following is the two phase solution procedure for the current application:

1) Variable initialization
2) Calculate properties and momentum exchange coefficients
3) Calculate momentum equation coefficients
4) Calculate the pseudo velocities
5) Solve for the pressure field
6) Solve the momentum equations for velocities of both phases
7) Solve the pressure correction equation and correct the velocities of both phases
8) Solve the concentration equation
9) Calculate particle – fluid Nusselt number
10) Solve the energy equation for fluid, solids, and wall temperatures
11) Solve the tube wall temperature equation
12) Check convergence if not return to 2)

During the solution the following values of relaxation were used

Velocities: $\omega = 0.5$

Thermal: $\omega = 1.0$

Concentration: $\omega = 0.5$ (unless locally modified as described in section 4.2.2)

The above iterative solution is repeated until the final solution of all variables is found. The solution was considered converged when the overall mass residual, the energy residual, and each of the velocity variables met the following convergence criteria.

Mass:

$$\frac{\sum_{i,j,k}\left(\phi_l + \phi_s\right)}{\dot{m}^*_{in}} < 10^{-3} \tag{4.32}$$

where $\phi =$ Residual of *continuity eq.s*

Velocity:

$$\frac{\sqrt{\sum\left(\phi_{q\,\mathrm{Res}}\right)^2}}{W_m \dot{m}^*_b} < 10^{-3} \tag{4.33}$$

where $\phi =$ Residual of U_l, V_l, W_l, U_s, V_s, *and* W_s *momentum eq.s*

Energy:

$$\frac{\sqrt{\sum\left(\phi_{l\,\mathrm{Res}} + \phi_{s\,\mathrm{Res}}\right)^2}}{\dot{E}^*_{in}} < 10^{-5} \tag{4.34}$$

where $\phi =$ Residual of solid and liquid.

4.3 Code Verification

The numerical code was verified by first using a single phase liquid where the circumferentially averaged Nusselt numbers were compared to analytical results and previous experimental results and then tube wall temperatures were compared to experimental results of the current work. Two phase thermal numerical solutions were compared to experimental results of the current work which included the melting of the encapsulated particles.

4.3.1 Pure fluid flow comparison

Numerical results of a pure fluid for a hydrodynamically fully developed axisymmetric flow with pure forced convection are compared with an analytic tube wall Nusselt number solution by Siegel et al.[63]

$$\mathrm{Nu} = \frac{2}{\frac{11}{24} + \sum C_n \mathrm{e}^{\frac{\beta_n^2 \, x}{\mathrm{Re}\,\mathrm{Pr}\,R}} R_n} \tag{4.35}$$

where the constants in Eq. 4.35 may be found in Ref. 63. Numerical results of a hydrodynamically fully developed mixed convection flow are also compared with the experimental results of Petukhov[22] for Rayleigh numbers of 6 x 10^6 and 1.4 x 10^6 in which water was the working fluid flowing inside a stainless steel circular tube. The local circumferentially averaged Nusselt number is presented for comparison in Fig. 4-5. The results for the numerical case which was an axisymmetric flow were good as was the case with mixed convection when $\mathrm{Ra} = 6.0x10^6$. When the Rayleigh number was $\mathrm{Ra} = 1.4x10^6$ the numerical results were slightly higher than the experimental results with a maximum percent difference of 9%, where the percent difference was found as

$$\%\,Diff = \frac{2\times\left|\phi_1 - \phi_2\right|}{\phi_1 + \phi_2} \qquad 4.36$$

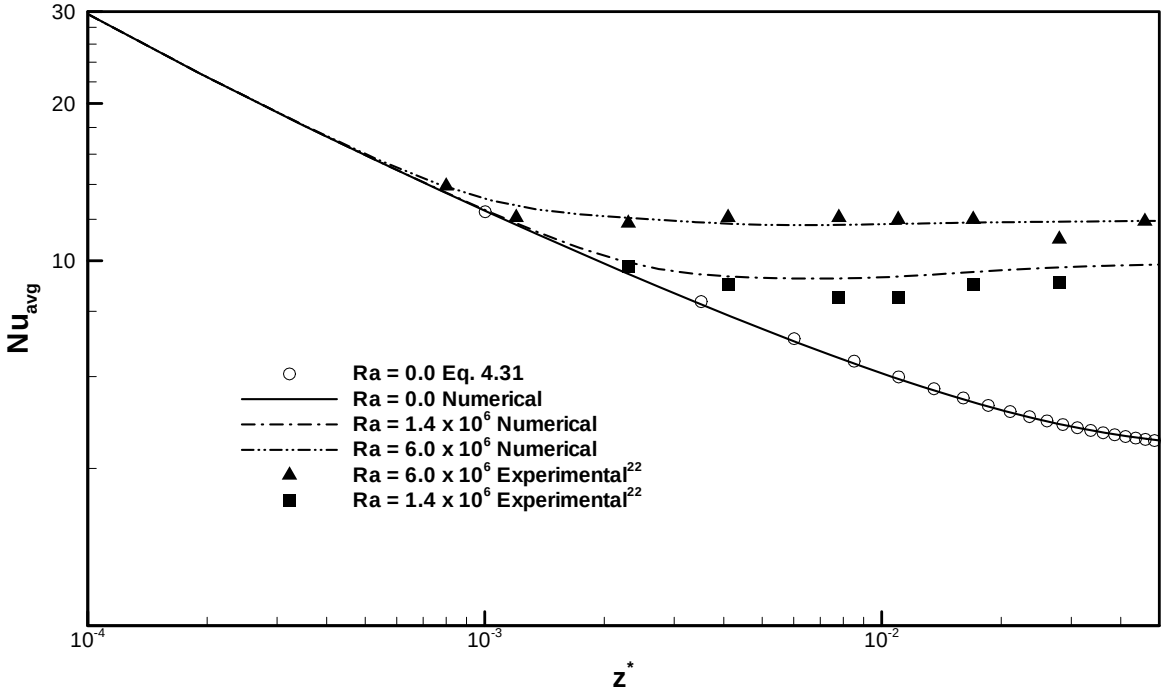

Figure 4-5 Numerical comparison with experimental and analytical data

Numerical results from the code were also compared to experimental data for the single phase flow with ethylene glycol and water as the working fluid in a circular copper tube of the current work. The outer tube wall temperatures were compared at a Rayleigh number of 4.1 x 10^6. Results of the circumferentially averaged wall temperature may be seen in previously presented Fig. 3-6 and the upper and lower numerical tube wall temperatures were compared with the experimental results in Fig. 4-6. The numerical results predict the circumferentially averaged wall temperatures and Nusselt numbers accurately when compared to experimental data from literature, Fig. 4-5, and the upper and lower tube wall temperatures, Fig. 4-6, of the current experimental data were

consistently above the experimental data with a maximum percent difference of 7.5%. This is slightly higher than the $\pm 7.0\%$ for the average wall temperature at that position.

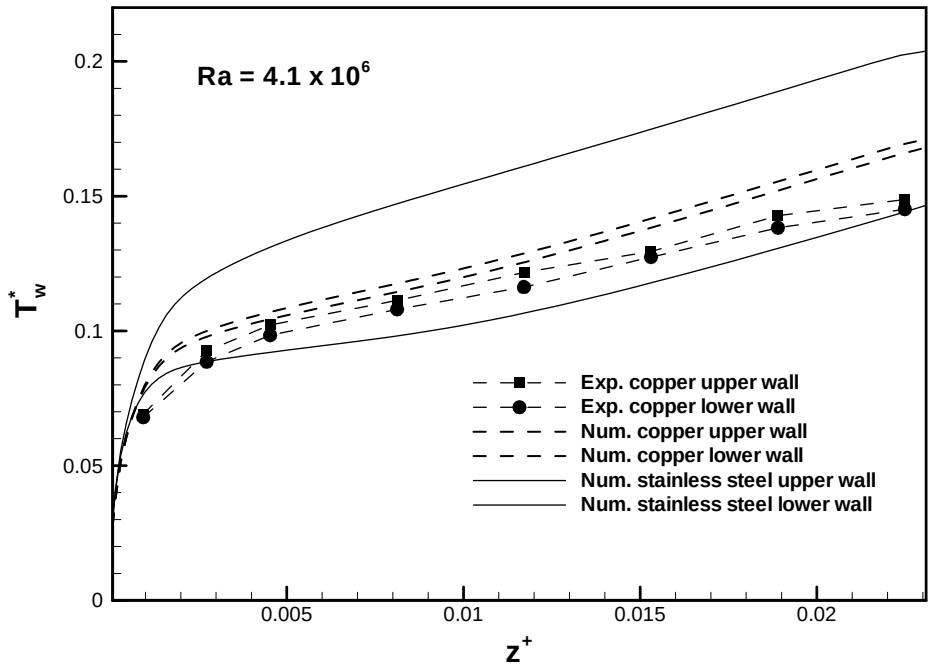

Figure 4-6 Upper and lower wall temperatures

In order to show the thermal effects of the tube wall material, numerically found upper and lower dimensionless wall temperatures are also shown in Fig 4-6 using the same experimental conditions but with a stainless steel tube wall of the same dimensions as the copper wall used during the experiment. These numerical results indicate the extent of circumferential heat transfer for the stainless steel tube wall compared to that of the copper tube wall which have thermal conductivities of 14.9 and 401 $W/(m-K)$ respectively.[24]

4.3.2 Two phase experimental comparison

The code was additionally verified with the solid – liquid flow experimental results of the current work presented in Chapter 3. Figure 4-7 shows comparisons of experimental and numerical results at two different lengths with PCM melting and one length with no melting of the PCM particles. The wall average temperature is presented for clarity and because the top and bottom tube wall temperatures are nearly the same.

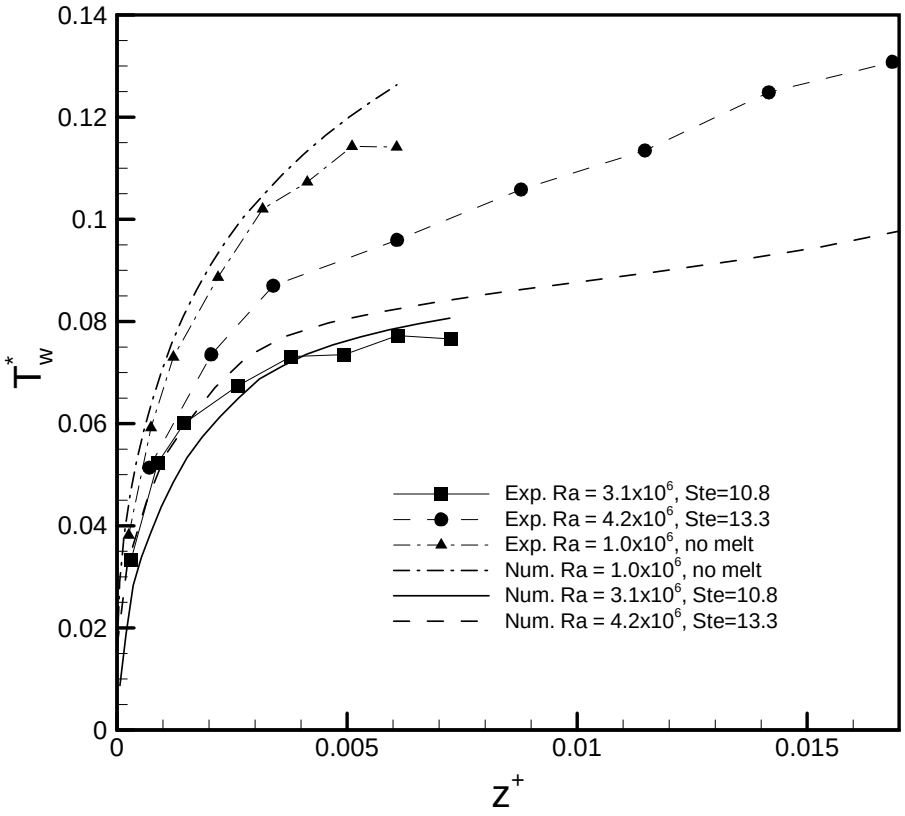

Figure 4-7 Two phase PCM numerical / experimental comparison

The numerical results for the flow with no PCM melting were consistently higher than the experimental but was a low difference (note that the last experimental point was not considered a

good measurement due to the experimental setup end effects discussed in Chapter 3). The numerical results for the shorter melting matched the experimental results well starting below the experimental data and ending slightly above the data at the tube outlet. The numerical results for the longer case were consistently below the experimental data and the second to last experimental point was approximately 24% lower. At similar Rayleigh numbers for single phase flow the experimental uncertainty was +/- 6%. The experimental uncertainty is expected to be higher for the two phase flow with melting but the 24% is thought to be excessive.

A numerical investigation into the cause of the discrepancy included varying the inlet concentration, particle density, slurry thermal conductivity, strength of cross stream recirculation due to mixed convection, and supercooling of the PCM, the cause was found to be supercooling. Figure B-2 is the cooling curve of bulk octacosane which is shifted about 5 ºC below the heating curve, Fig. B-1. The experimental cooler outlet bulk slurry temperature, TC-12 in Fig. 3-1, was recorded as 56.8 ºC, which is not cooled below the super cooled temperature shown in Fig. B-2. Therefore some of the latent heat is not available during the heating and melting process. The amount of latent heat unavailable is difficult to predict for the following reasons:

1) Cooling was accomplished by using a concentric counter flow tube in tube heat exchanger which caused temperature differences within the slurry. The microPCM particles near the cooled wall are cooler than those at the core of the flow, therefore some particles may have been cooled below 50 ºC making 100 % of the latent heat available while the microPCM particles in the center will be cooled only to 56.8 ºC, the bulk slurry temperature.
2) The preheater used to keep the slurry at the inlet temperature of 58.85 ºC was an electric heat trace wrapped around the copper pipe leading

into the recirculation pump, see Fig 3-1. This addition of heat again caused temperature differences with the slurry flow. The microPCM particles near the heated wall were some temperature above the 58.85 ºC inlet temperature but were cooled back to the 58.85 ºC inlet temperature, by pump mixing action, before entering the test section. It is then probable that any latent heat of these particles would not be recovered due to super cooling.

3) A further complication is the non-homogeneous flow concentration due mainly to the gravity. Near the top of the tube there would be more particles but flowing at a slower velocity than the rest of the tube, as will be shown in Ch. 5.
4) The DSC cooling curve shown in Fig. B-2 is for bulk octacosane, the micro encapsulation process can alter this curve.

In spite of these difficulties numerical predictions were numerically tested by adjusting the amount of latent heat available for each portion of the melting process, solid to solid and solid to liquid. The results of these tests are shown in Fig. 4-8. The best fit of the experimental data from the numerical testing were 0% of the latent heat from the solid to solid phase change was available and 50% of the latent heat from the solid to liquid phase change was available.

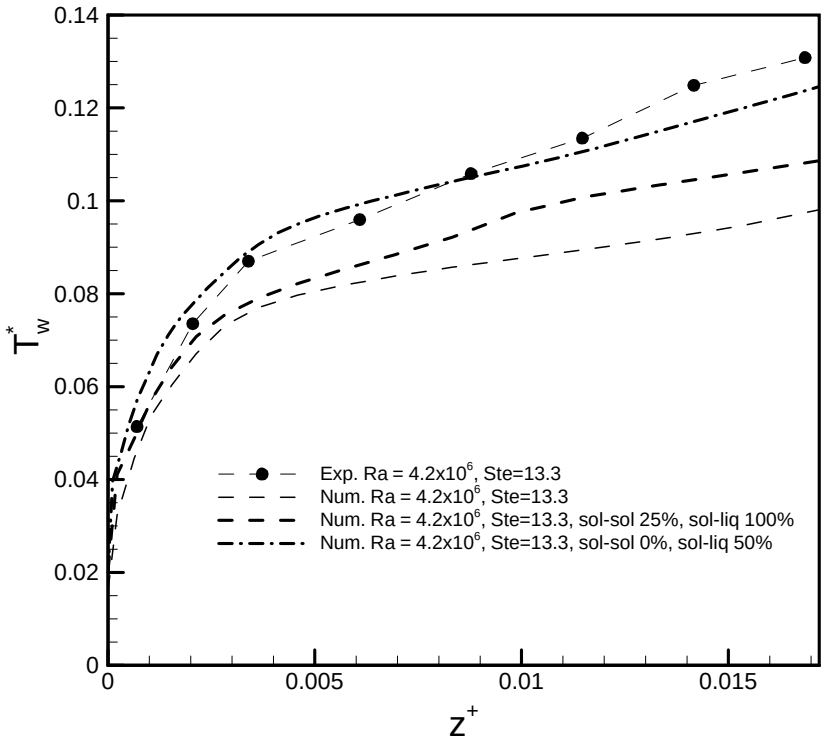

Figure 4-8 Dimensionless wall temperatures of the numerically corrected available inlet latent heat

5 NUMERICAL RESULTS

5.1 Control case

In order to investigate the effects of some of the most important parameters involved in the microPCM application a control case, based on experimental run #9-24_1, will be considered under the following conditions: a uniform inlet velocity and concentration, a uniform temperature of 58.85 ºC, and a uniform heat flux which starts at the inlet of the tube thus hydrodynamic and thermally developing flow will be considered. In addition the control case will have the following parameters:

$$\begin{array}{lllll} \mathrm{Re} = 424 & \mathrm{Ra_b} = 1.5\mathrm{x}10^{6} & & \mathrm{Pr} = 30.3 & \mathrm{Ste} = 10.8 \\ \mathrm{Ar} = 4.76\mathrm{x}10^{-3} & \rho_l^* = 1.03 & \rho_p^* = 0.91 & \alpha_s = 0.25 & \\ \Delta = 0.115 & k_w^* = 1139 & k_l^* = 1.18 & k_p^* = 0.57 & \mu_l^* = 0.41 \end{array} \qquad 5.1$$

Although shown in previous chapters to be important supercooling will be neglected during for the duration of the work presented here. In addition for the numerical work presented here the liquid viscosity will be considered constant at the bulk temperature of the experimental run on which the control case is based. The liquid viscosity is considered constant because it is possible during the parametric investigations that the fluid temperature could go outside the range of applicability of the temperature dependent viscosity equation describing the 50 / 50 ethylene glycol / water mixture, Eq. 3-7. The viscosity due to the addition of particles, Eq. 2-36, is still used as it is dependent on the volumetric concentration only not the fluid temperature.

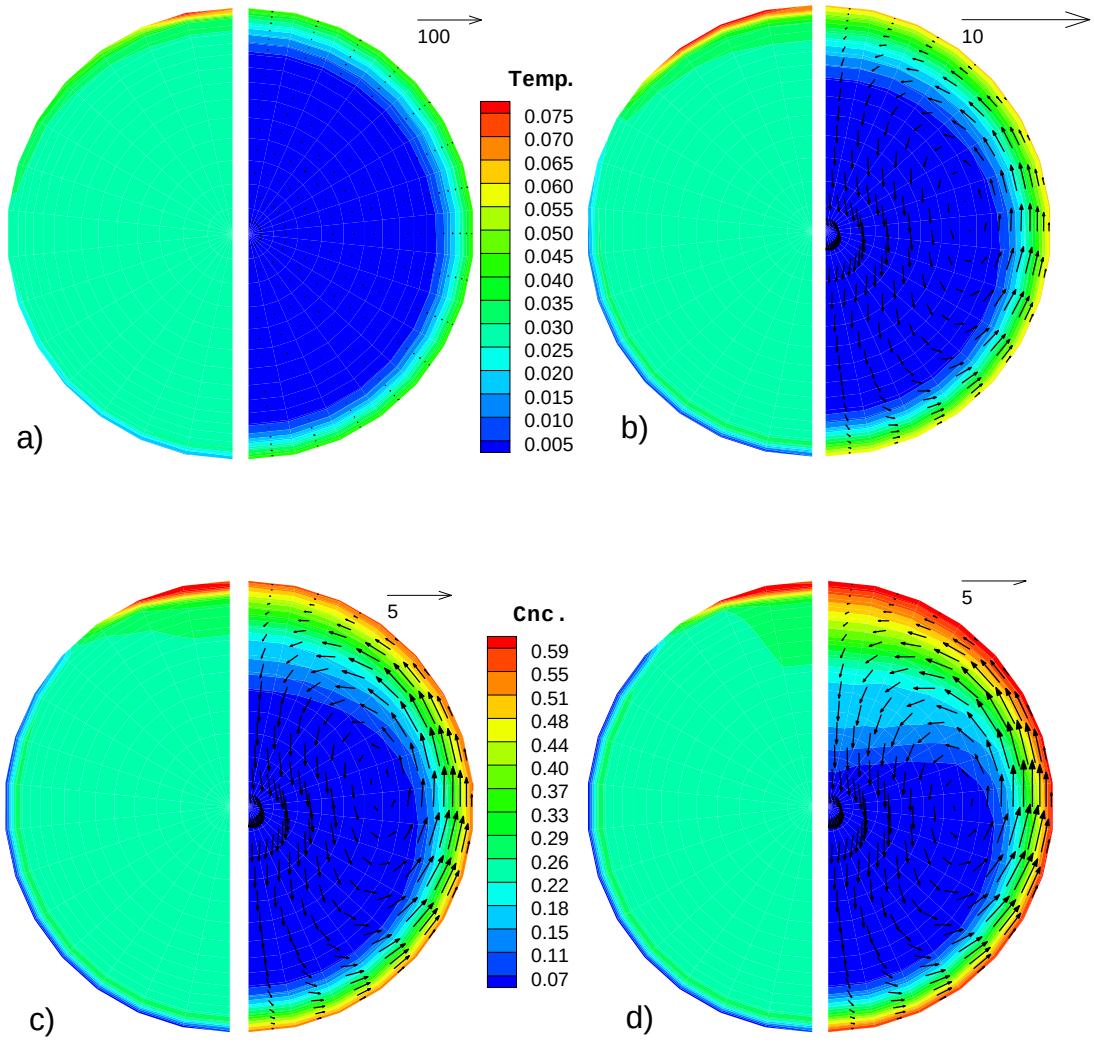

Figure 5-1 Concentration / Temperature contour plots and velocity vector plots at various axial locations a) $z^+ = 0.0014$, b) $z^+ = 0.0024$, c) $z^+ = 0.0038$, and d) $z^+ = 0.0069$

Concentration and thermal contours and velocity vector plots are shown for the control case in Fig. 5-1 at several axial locations. Each contour plot within Fig. 5-1 is at the same scale for comparison purposes and a reference velocity arrow is shown for the velocity vector plots. The plots show a particle phase concentration at the compaction limit (0.624) at the top of the tube

which forms quickly and continues to grow throughout the length of the tube. At the outer radius at the bottom of the tube a low concentration of particles begins to form near the entrance of the tube and spreads circumferentially up along the tube wall. The axial development of the particle phase concentration is presented in Fig. 5-2 at several radial locations. At the outer radius the compaction limit is reached at approximately an axial location of 0.0011, while the nearly particle free zone at the outer radius in the lower portion is reached at an axial location of 0.0040. Consistent with the solid phase concentration contour plots the central portion of the flow remains near the inlet concentration. There is a region at the upper portion of the tube where the concentration is higher whose area becomes smaller circumferentially and thicker radially with increasing axial distance.

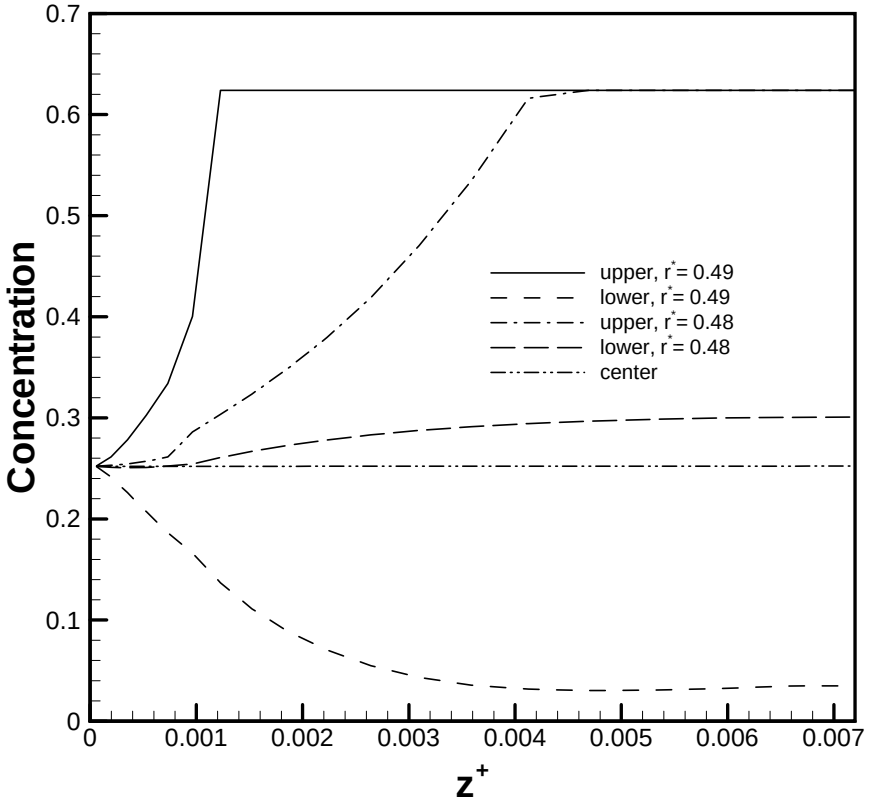

Figure 5-2 Axial concentration variations for control case

The buoyancy driven circulation of both phases is up along the heated wall and straight down through the central part of the flow. The circulation velocity at the outer wall is zero and increases to a maximum and decreases toward the circulation center. This circulation profile is similar to that found by others[28] when a single phase fluid is considered. A development of the axial velocity profile within the tube is presented in Fig. 5-3. The velocity of both phases is shown however the difference in velocity is negligible due to the small 20 micron particle diameter. Both phases enter the tube at a uniform velocity and develop quickly. The exit velocity profile remains unchanged from the previous axial location. At the upper portion of the tube the velocity gradient at the tube outlet is lower and increases as the slurry moves away from the upper wall. This is due to an increased bulk viscosity of the two phase flow with the solids concentration at or near the compaction limit. At the lower portion of the tube near the tube wall a higher velocity at the tube outlet occurs due to the low solids concentration and thus lower bulk viscosity. The bulk viscosity varies exponentially with particle concentration as shown by Eq. 2.36. Also the maximum velocity has shifted slightly below the tube centerline.

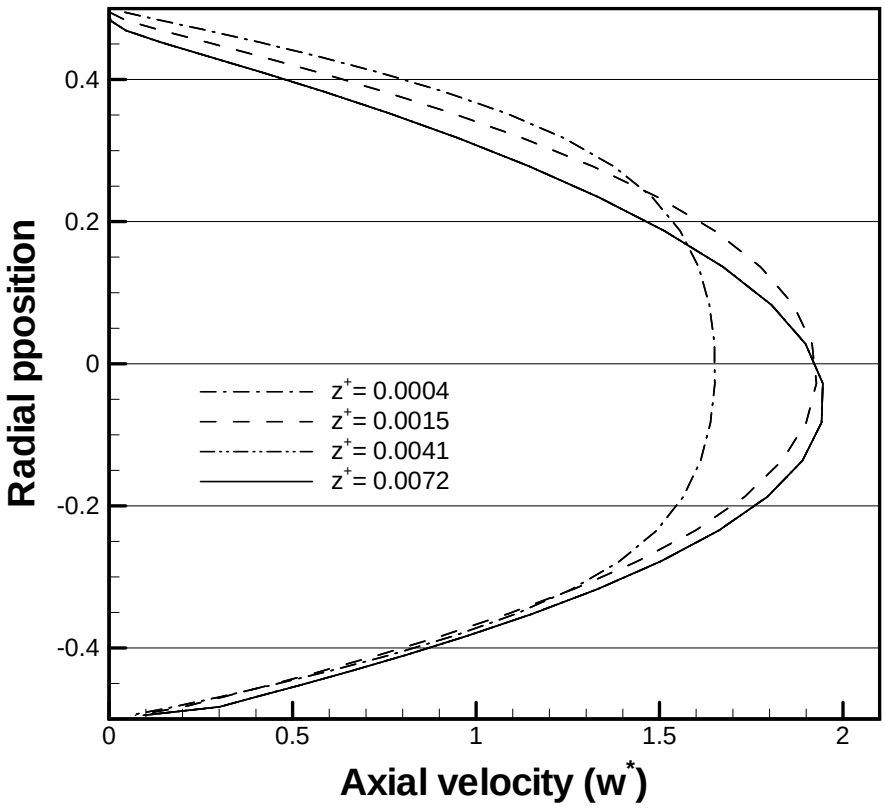

Figure 5-3 Velocity profiles for control case

The thermal development, Fig. 5-1, at the inlet of the tube is symmetric top to bottom but becomes cooler at the bottom and hotter at the top of the tube with an increase in axial position. The hotter buoyant fluid is moving upward and stagnating in the vertical direction at the upper portion of the tube, this is again similar to findings of a single phase fluid in mixed convection. The axially varying dimensionless temperature at the outer tube wall is presented in Fig. 5-4. For the control case, based on the experimental work, the copper tube was used. There was very little difference between the upper and lower outer tube wall temperature. The tube material considerations, also shown in Fig. 5-4, will be discussed further in the following sections.

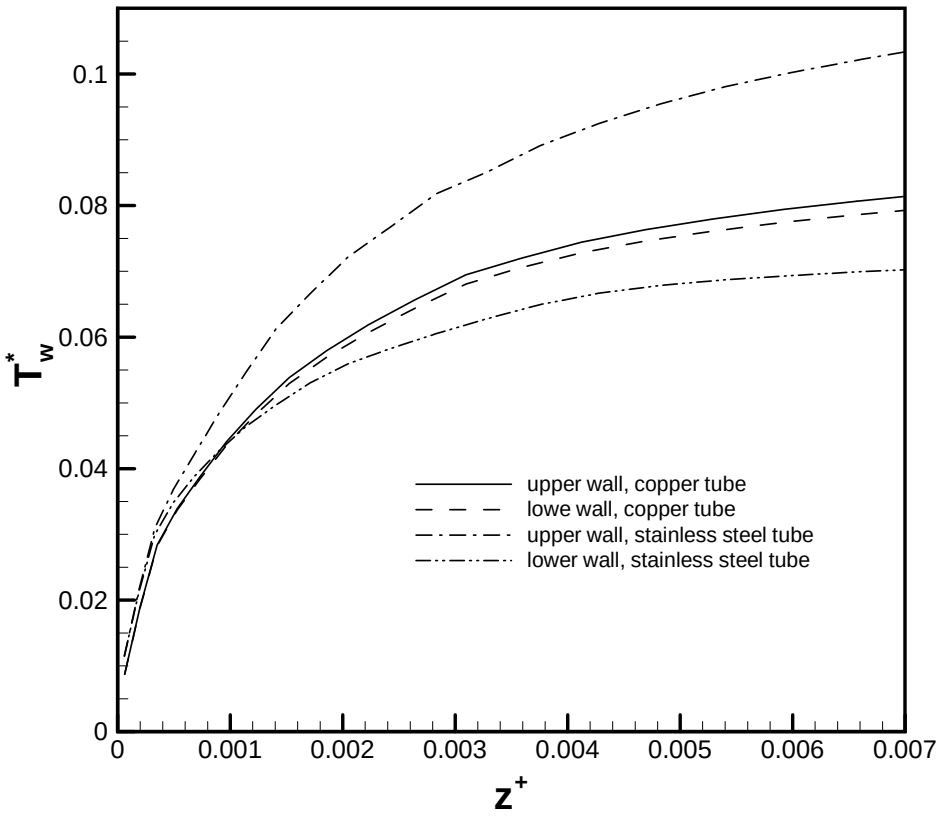

Figure 5-4 Dimensionless axial tube wall temperatures

5.2 Application considerations

5.2.1 Inlet Temperature

The apparent specific heat for octacosane is temperature dependent as shown in Fig. 3-3, which is common to PCM's. The inlet temperature of the slurry to the heat transfer section may be below, within, or above the range of phase change for the PCM being used. The following is to investigate the effects of inlet temperature upon outer tube wall temperatures. The resulting dimensionless tube wall temperatures are presented in Fig. 5-5 for several inlet temperatures and

the control case of 58.82 °C. For reference purposes the position of the various inlet temperatures on the melting curve may be seen in Fig. 3-3. The only changes from the control case were the following inlet temperatures, given in dimensional form as

$$T_{in} = 57.0,\ 58.0,\ 58.82\ (\textit{control case}),\ 60.0,\ \textit{and}\ 62.0\ ^{\circ}C \qquad 5.1$$

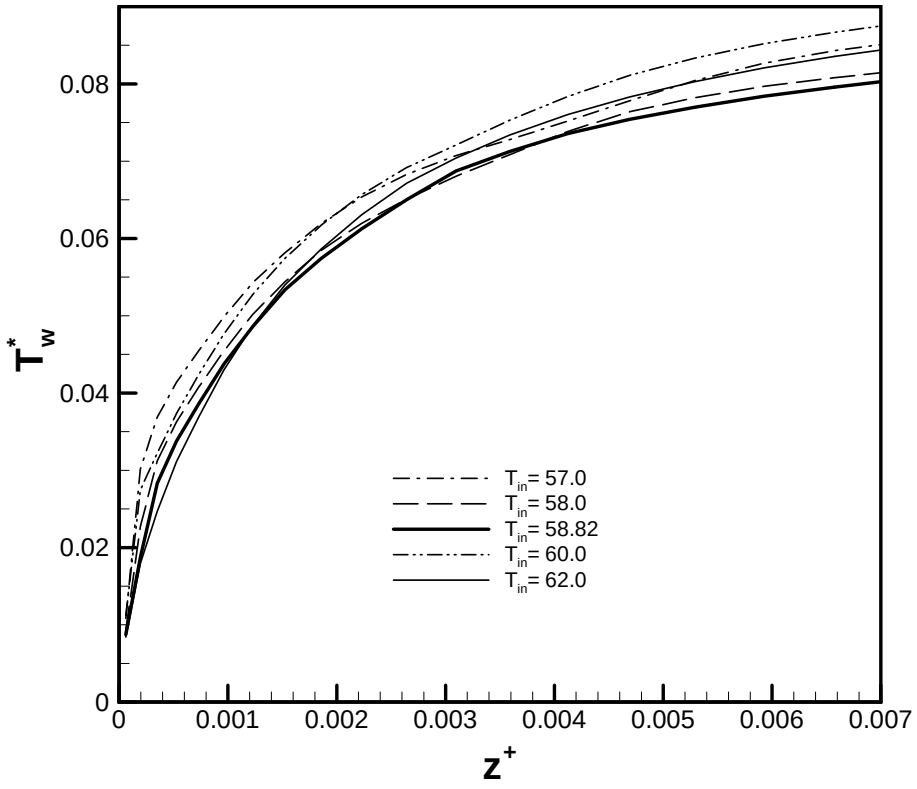

Figure 5-5 Tube wall temperature at various Inlet Temperatures

The control case of T_{in}= 58.82 ºC provided the lowest tube wall temperature at the outlet which was approximately 9% below the highest outlet tube wall temperature which occurred at T_{in}= 60.0 ºC. It is interesting to note that the highest tube wall temperature at the outlet did not occur using the highest inlet temperature of 62.0 ºC and this same inlet temperature provides the lowest tube

wall temperature at the inlet of the tube, as shown in Fig. 5-5. The reason for this can be seen in Fig. 3-3 where the 62.0 ºC inlet temperature occurs just before the highest apparent specific heat. This indicates that not only the amount of latent heat available but also the range of temperature over which the phase change occurs is an important factor for the tube wall temperature.

5.2.2 Tube Wall effects

A tube wall having a finite thickness and thermal conductivity will conduct heat radially, axially, and circumferentially. This is true for any flow condition including single phase and multi-phase flow. The relative importance of each direction of conduction will be dependent upon tube wall material and thickness, the Peclet number, and the Rayleigh number. The Peclet number is an indicating factor of axial conduction because it is a measure of the energy being convected axially by the flow while the Rayleigh number indicates circumferential conduction as it is a measure of the strength of the natural convection causing cross stream circulation. Both axial and circumferential wall conduction were discussed earlier along with correlating parameters in chapters two and three respectively. In the solid-liquid flow situation these correlations are expected to still be true but with additional parameters needed including concentration, density ratios, particle to duct ratio, and the Stefan number.

The effects of circumferential tube wall conduction are now considered. The copper wall of the control case is compared to that of a stainless steel tube wall of the same thickness. The axial tube wall temperature variations are presented in Fig. 5-4, while circumferential variations are presented in Fig. 5-5. For the copper wall there is very little difference in upper and lower wall temperature indicating a high amount of heat transfer from the upper portion of the tube wall to the lower portion. While for the stainless steel there is a larger difference in upper and lower tube wall temperatures. At the inlet, Fig. 5-4, the tube with the stainless steel wall has a higher outer

tube wall dimensionless temperature than the copper wall, this is due to the reduced thermal conductivity of the stainless steel causing a higher temperature difference to accomplish the same heat transfer in the radial direction. The results for the stainless steel tube wall are similar to single phase experimental results reported by Petkuhov.[22] The parameters changed from the control case were

$$\begin{aligned} &copper\ \ (control\ \ case): && k_w^* = 1139 \\ &stainless\ \ steel: && k_w^* = 43 \end{aligned} \qquad 5.2$$

The stainless steel tube wall conductivity ratio was approximately $1/26^{th}$ of the copper tube wall.

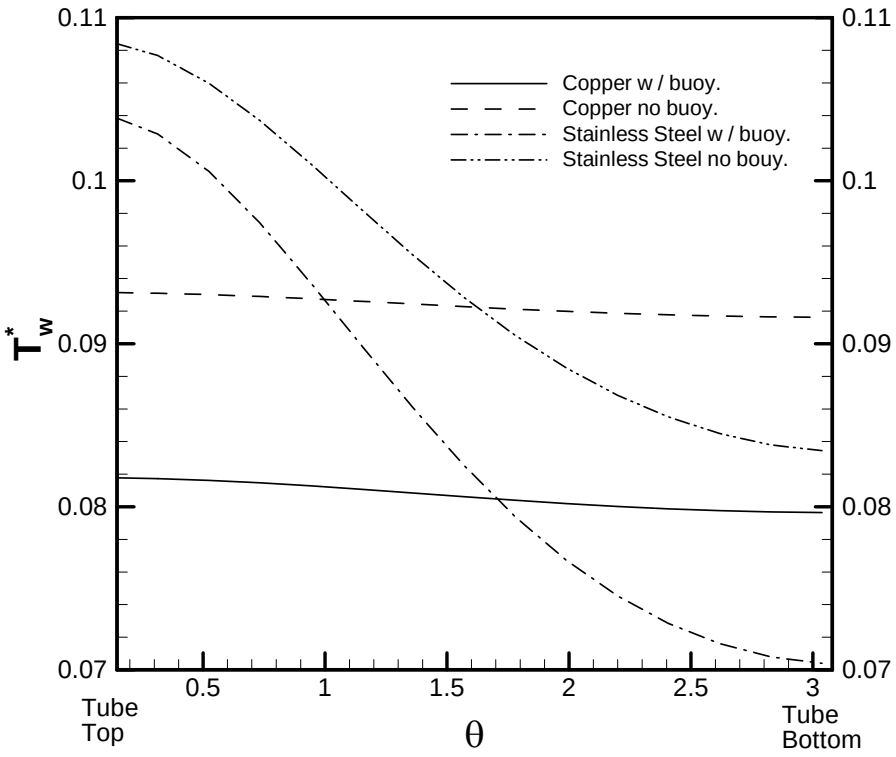

Figure 5-6 Circumferential outer wall temperatures

5.2.3 Buoyancy effects

A settling velocity for a particle in a stagnant liquid results from the balance of gravity and drag force which act oppositely. As a reference the settling velocity of a homogenous stagnant slurry is calculated to get a feeling for the buoyant effects within the flow. The settling velocity is found using[64]

$$v_{set} = -v_{\infty}(1.0 - \alpha_s)^{4.7} \qquad \text{Eq 5.3}$$

where

$$v_{\infty} = \left(\frac{4gd_p\left(\rho_p/\rho_l - 1.0\right)}{3C_D} \right)^{0.5} \qquad \text{Eq 5.4}$$

which is the settling velocity of a sphere in an infinite medium and

$$C_D = \frac{24}{\mathrm{Re}_p} \qquad \mathrm{Re}_p < 0.2 \qquad \text{Eq 5.5}$$

Under the experimental conditions of Chapter 3, from which the properties in the following numerical simulations were based, the settling velocity is calculated as 2.1 x 10^{-6} m/s, using the experimental data of run # 9-24_1.

The effect of the particle buoyancy was investigated by comparing the numerical results of the control case, in which buoyancy was included, to numerical results when buoyancy was neglected. Numerically this was accomplished by setting the Archimedes number in Eq.s 2-12 and 2-13 to zero, effectively eliminating the buoyancy. In addition both the stainless steel and copper walls under the two buoyant conditions were investigated. The changes to the control case were

$$
\begin{aligned}
&\textit{copper (control case)}: && k_w^* = 1139 \\
&\textit{stainless steel}: && k_w^* = 43 \\
&\textit{control case}: && \mathrm{Ar} = 4.76\,x10^{-3} \\
&\textit{neutrally buoyant}: && \mathrm{Ar} = 0.0
\end{aligned}
\qquad \text{Eq 5.6}
$$

Neglecting the buoyant term for the copper tube wall led to higher wall temperatures starting at an axial position of 0.002 and continued to increase along the length of the tube, Fig. 5-7a. The stainless steel wall, Fig. 5-7b, showed a difference starting at an axial position of 0.001 and while the bottom the tube with buoyancy included remained below the neutrally buoyant case, the top tube wall started above the neutrally buoyant case and then crossed below at an axial position of about 0.005. The copper wall has very little circumferential temperature variation both with and without buoyancy, Fig. 5-7a. The stainless steel has a larger circumferential wall temperature variation with the buoyancy included case having a higher variation of 0.034 compared to the neutrally buoyant case with a 0.026 difference at the outlet. The temperature at the upper portion of the stainless tube changed 0.004 between the two buoyant cases while at the bottom of the tube the change was 0.014.

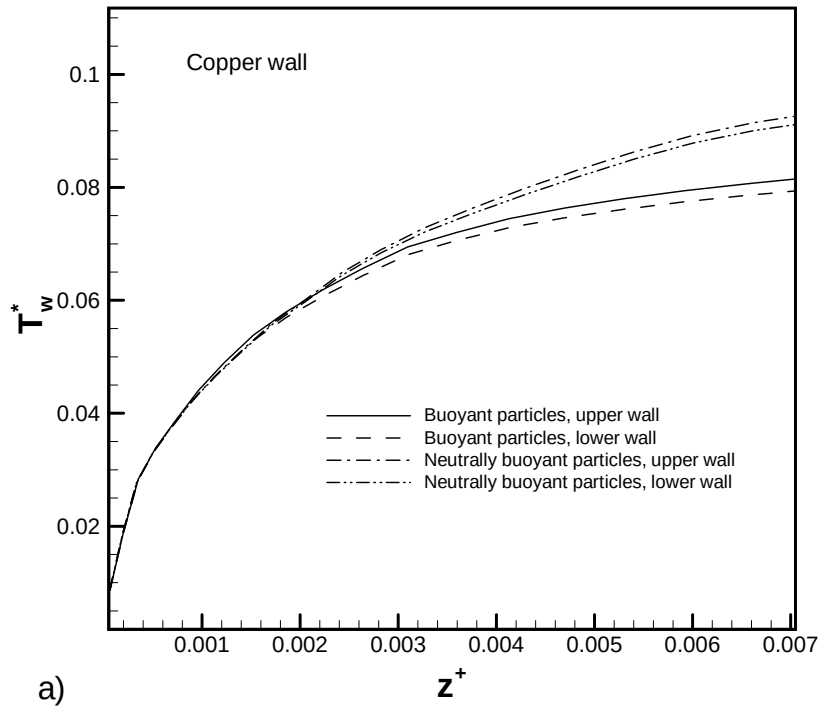

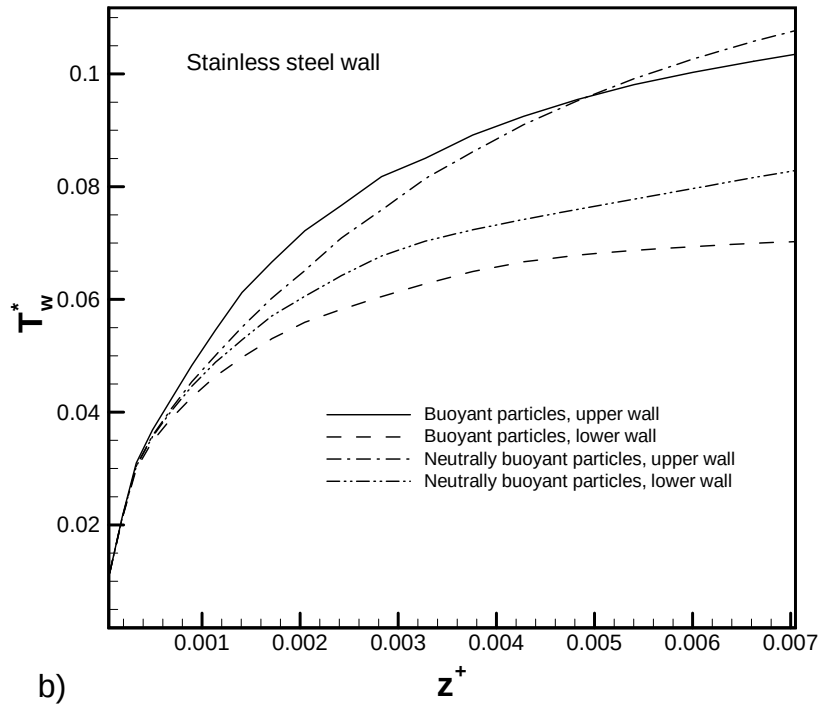

Figure 5-7 Particle buoyancy effects on upper and lower wall temperature a) copper tube and b) stainless steel tube

Concentration and thermal contours and a velocity vector plot are presented in Fig. 5-8 for the tube wall materials and buoyancy effects at the tube outlet. In Fig. 5-8 two concentration legends are used due to the large difference in concentrations for the two different buoyancy cases while one temperature legend is used for all cases. When buoyancy is neglected, Fig.s 5-8a and b, the slurry becomes nearly homogenous throughout the flow with solids concentrations varying from approximately 21% at the upper portion of the tube to 26% along approximately three quarters of the tube wall. The temperature of the neutrally buoyant case has a thicker hot portion at the top tube wall for the copper case. The concentration contours are nearly the same for the two tube wall materials. Even at the low settling velocity calculated using Eq.s 5.4 - 5.6, the buoyancy term has a noticeable effect on the thermal solution and the solids concentration across the slurry.

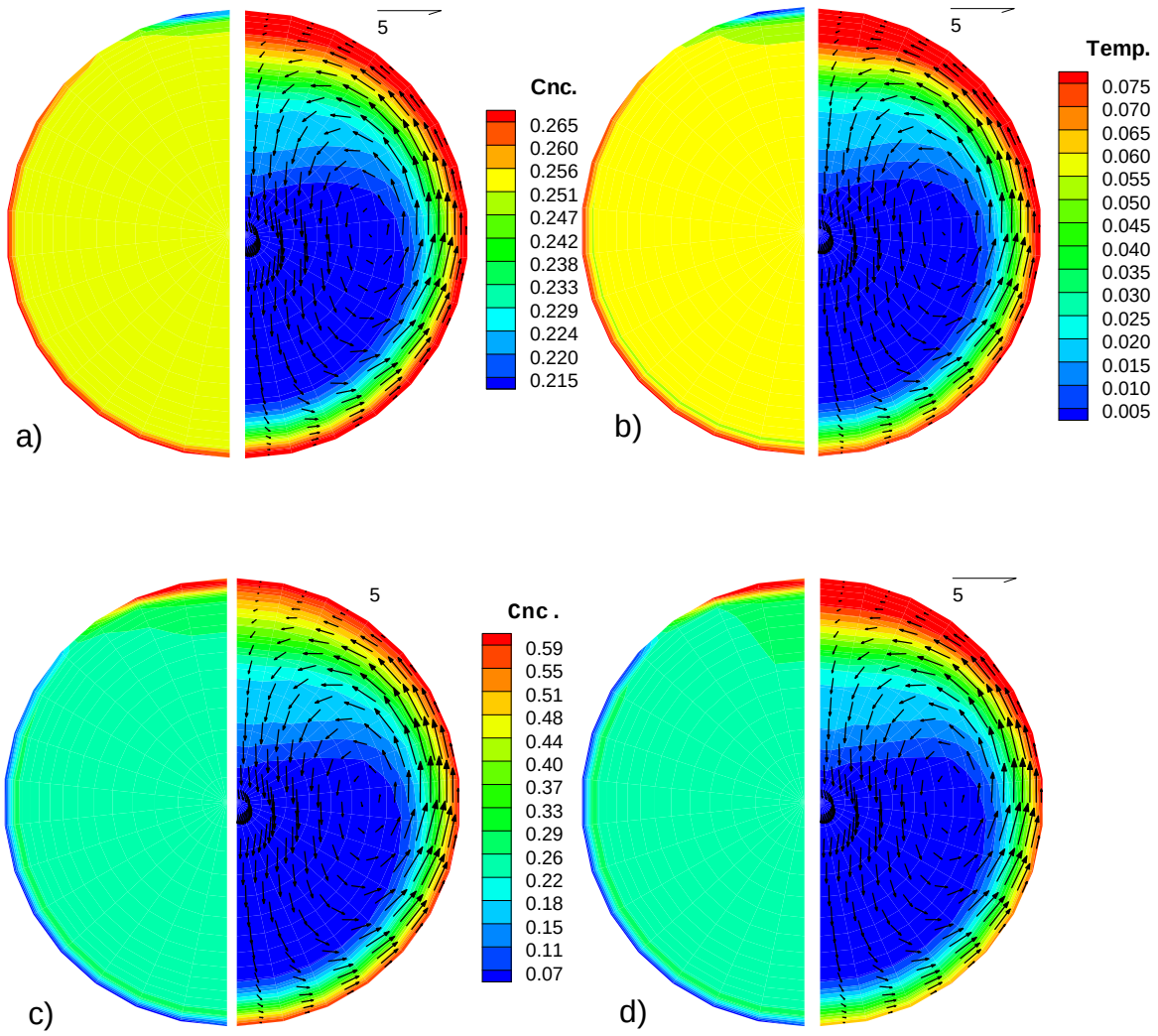

Figure 5-8 Buoyancy effects on solids concentration, temperature, and velocity at tube outlet a) neutrally buoyant copper wall, b) neutrally buoyant stainless wall, c) buoyant copper wall, and d) buoyant stainless wall

5.2.4 Concentration

Several methods have been used for comparing microPCM slurry flows of different concentrations or a pure fluid and include setting equal the mass flow rate or Reynolds number.

Here different concentrations are compared by using a constant power as the basis for comparison. This assumes a given application will have the same pump power available for any fluid flow.

For flow through a tube the required pump power is given by

$$P = \dot{m} f \frac{LV^2}{2D} \tag{5.7}$$

where f is the friction factor. The friction factor for laminar flow is

$$f = \frac{64}{\mathrm{Re}} \tag{5.8}$$

However, in the current application there is a two phase flow with mixed convection, therefore the friction factor will need to be adjusted to account for the mixed convection. A correlation[26] which was found for single phase fluids is then used to account for the mixed convection in the current two phase flow based on bulk properties. For the correlation the laminar friction factor is modified by an amount dependent on the bulk Rayleigh number

$$f^+ = \frac{64}{\mathrm{Re}} \left\{ 1.0 + \left(0.195\, \mathrm{Ra}_b^{0.15} \right)^{15} \right\}^{1/15} \tag{5.9}$$

The bulk Rayleigh number uses bulk slurry properties for all properties except for the coefficient of volumetric expansion which will be based only on the fluid properties. Substituting Eq. 5.9 into the pump power equation, Eq. 5.7, yields

$$P = \frac{128L}{\pi D} f^+ \dot{Q}^2 \mu_b \tag{5.10}$$

The first term in Eq. 5.10 remains constant for a given application and therefore if the power is to remain constant the term $f^+ \dot{Q}^2 \mu_b$ must remain constant between the various microPCM particle loadings. For the control case, based on experimental run #9-24_1, the mixed convection modified friction factor was $f^+ = 0.249$ and $f^+ \dot{Q}^2 \mu_b = 6.867 \text{ x } 10^{-14}$.

Table 5-1 is a matrix of test conditions which were varied from the control case and were were used in combination to investigate the effects of Ste, concentration, and flow rates. The Stefan number varies between the various concentrations because it is included in the definition of the Stefan number. The mass flow varies from 0.00790 (Re constant) to 0.01163 (power constant).

Table 5-1 Summary of concentration / Ste test condition

Y_s	α_s	**Ste**	$f^+\dot{Q}^2\mu_b$	$\dot{m}$ **(kg / s)**	**Re**
0.23	0.25	10.8	6.867×10^{-14} (control case)	0.009011	423
0.20	0.22	12.3	6.867×10^{-14} (power matched)	0.011663	627
0.20	0.22	12.3	5.326×10^{-14} (mass flow rate matched)	0.009011	485
0.20	0.22	12.3	4.651×10^{-14} (Re matched)	0.00790	423
0.23	0.25	5.4	6.867×10^{-14}	0.009011	423
0.20	0.22	6.2	6.867×10^{-14} (power matched)	0.011663	627
0.20	0.22	6.2	5.326×10^{-14} (mass flow rate matched)	0.009011	485
0.20	0.22	12.3	4.651×10^{-14} (Re matched)	0.00790	423

The dimensionless tube wall temperatures are plotted against axial position. At the higher Stefan number the temperatures are close together with the equal mass flow and equal power being nearly identical. At the lower Stefan number the equal Reynolds number at the lower mass flow rate is above the higher mass flow rate and the lower mass flow rates with equal power and

equal mass flow. Therefore as concentration changes equal pump power would be the best comparison method for a given application.

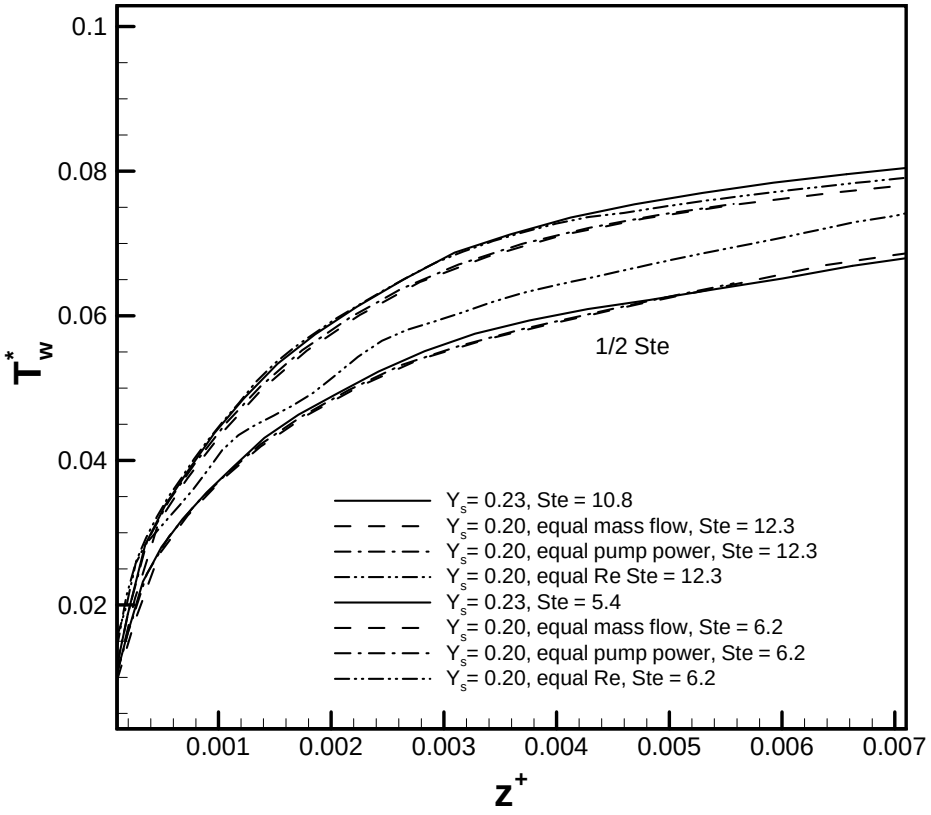

Figure 5-9 Stefan number variation at two concentrations

5.3 Parametric investigation

5.3.1 Rayleigh number

An increase in the Rayleigh number for a given flow causes a secondary cross stream flow pattern to develop in single phase flow. The secondary flow is a result in variations of the fluid

density due to temperature difference. The density variations in the numerical model developed have been linearized using the Bousinesq approximation and is directly related to the difference between the temperature of the local fluid with that of the inlet fluid temperature. The inlet temperature was chosen over a bulk temperature because the area of concern is the inlet region of thermally developing flows. The mixed convection phenomena have been well researched for the single phase flow. Similar secondary flows develop in the current application of a microPCM suspended in a carrier fluid forming a two phase flow.

5.3.2 Particle addition effects

The effects the microPCM particle addition has on the mixed convection resulting in a two phase mixed convective flow will be investigated. Figure 3-9 showed effects of the microPCM particles on the mixed convection with no melting. However, the experiment was limited to Raleigh numbers on the order of 10^5 otherwise the addition of heat required to raise the Rayleigh number would cause PCM melting. Numerically the Rayleigh number may be raised while not accounting for any latent heat effects due to melting and thus isolating the particle addition effects on the mixed convection. The control case was used with the following conditions modified

$$\begin{aligned} &\mathrm{Ra_b} = 0,\ 0.15\mathrm{x}10^6,\ 1.5\mathrm{x}10^6,\ \textit{and}\ 15.0\mathrm{x}10^6 \\ &\mathrm{Ste} = \infty \qquad\qquad (\textit{no melting}) \end{aligned} \tag{5.2}$$

Figure 5-10 includes the tube wall outer dimensionless temperature versus axial position for both a pure fluid and with the addition of the non-melting microPCM particles. From Fig. 5-10 the two phase flow showed a decrease in outer wall temperature at all values of the Rayleigh number. The difference between the single phase and two phase outer wall temperature decreased as the Rayleigh number increased. The dimensionless temperature of the single phase flow is above that

of the two phase flow at the inlet of the tube but for $Ra_b = 15.0x10^6$ the outer wall temperature becomes less than the lower Rayleigh number two phase flow cases at a dimensionless axial position of approximately 0.0012. The dimensionless wall temperature, when $Ra_b = 1.5x10^6$, was less than the dimensionless wall temperature for lower Rayleigh numbers during the two phase flow at an axial position of approximately 0.0055. Also for each Rayleigh number the single phase and two phase dimensionless wall temperatures appear to be parallel after reaching what seems to be a steady state when the wall temperature slopes become constant.

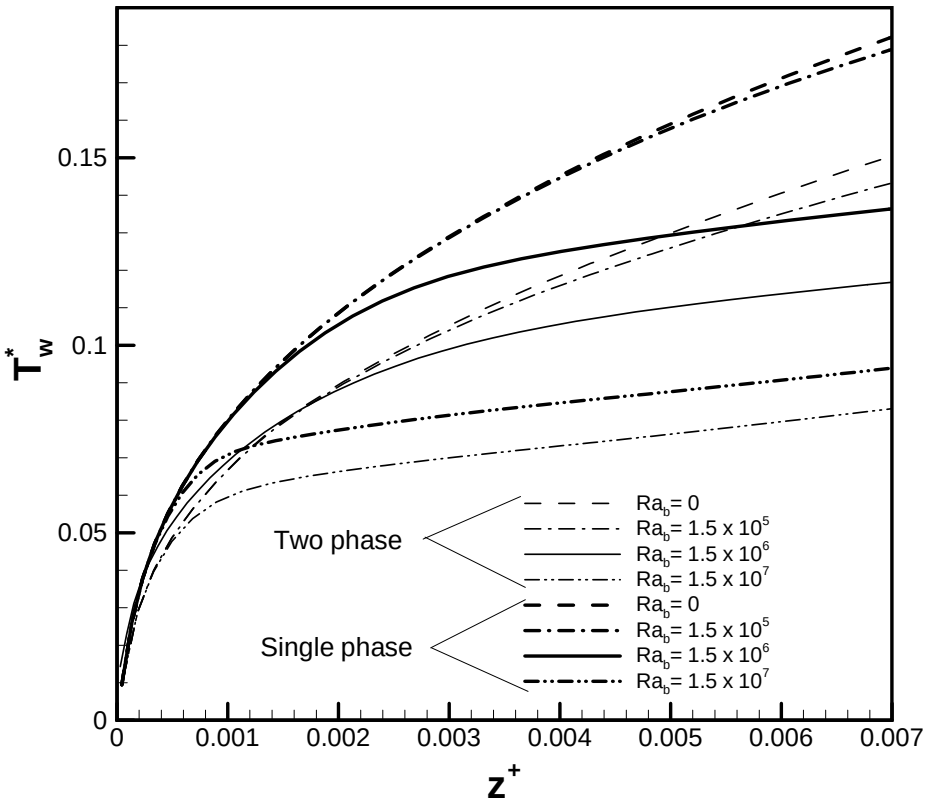

Figure 5-10 Mixed convection comparison of pure fluid and two-phase fluid at various Rayleigh numbers

The difference in dimensionless wall temperature and percent difference at the tube outlet are both summarized in Table 5-2.

Table 5-2 Outlet tube wall temperature differences at various Rayleigh numbers for a single phase fluid and a two phase fluid without phase change

Ra_b (x 10^6)	Dimensionless wall temperature difference at the tube outlet	% Difference
0	0.029	17
0.15	0.035	21
1.5	0.020	15
15.0	0.011	12

The contour plot of the tube outlet conditions, Fig. 5-11, compares an order of magnitude difference in the Rayleigh numbers. A concentration and temperature legend is shown for each Rayleigh numbers and the velocity vectors are all at the same scale. The enhanced heat transfer due to the addition of the particles can be seen through out the flow. The concentration for the two phase flow at the higher Rayleigh numbers is nearly homogeneous ranging from 0.24 to 0.26 where the gradients are isolated close to the wall. The lower Rayleigh number has a larger concentration variation of approximately 0.37 to 0.22 with the gradients still close to the wall but gradient position has moved farther into the flow.

The velocity profile at the exit of the tube is shown in Fig. 5-12 for both single phase and two phase flow at the two highest Rayleigh numbers. For both for both the single and two phase flows

the maximum axial velocity shifted downward with an increase in the Rayleigh number. The single phase maximum axial velocity was below that of the two phase flow for both Rayleigh numbers. This is consistent with the velocity vector plots of Fig. 5-11 which show a stronger cross stream circulation for the single phase flow at each Rayleigh number.

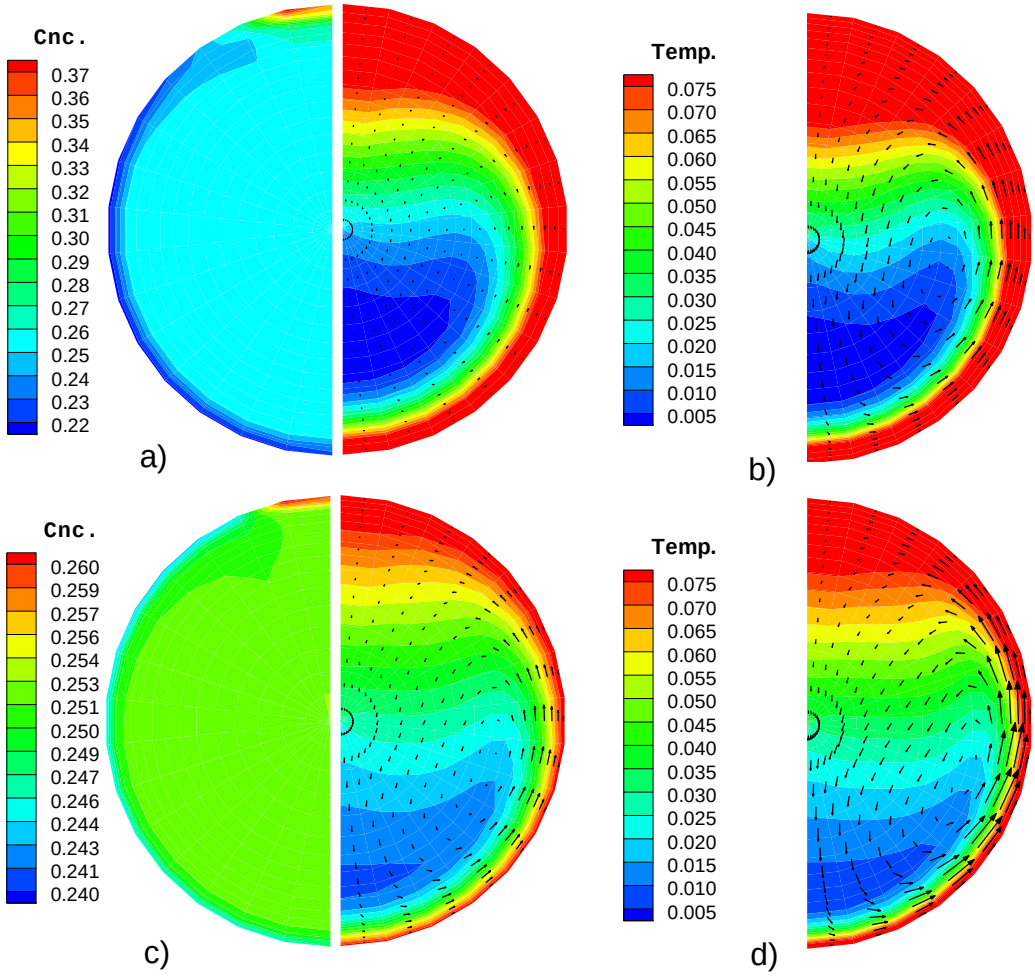

Figure 5-11 Two phase no melting – single phase outlet cross stream flow comparison a) Two phase Ra_b=1.5 x 10^6, b) Single phase Ra_b=1.5 x 10^6, c) Two phase Ra_b=1.5 x 10^7, and d) Single phase Ra_b=1.5 x 10^7

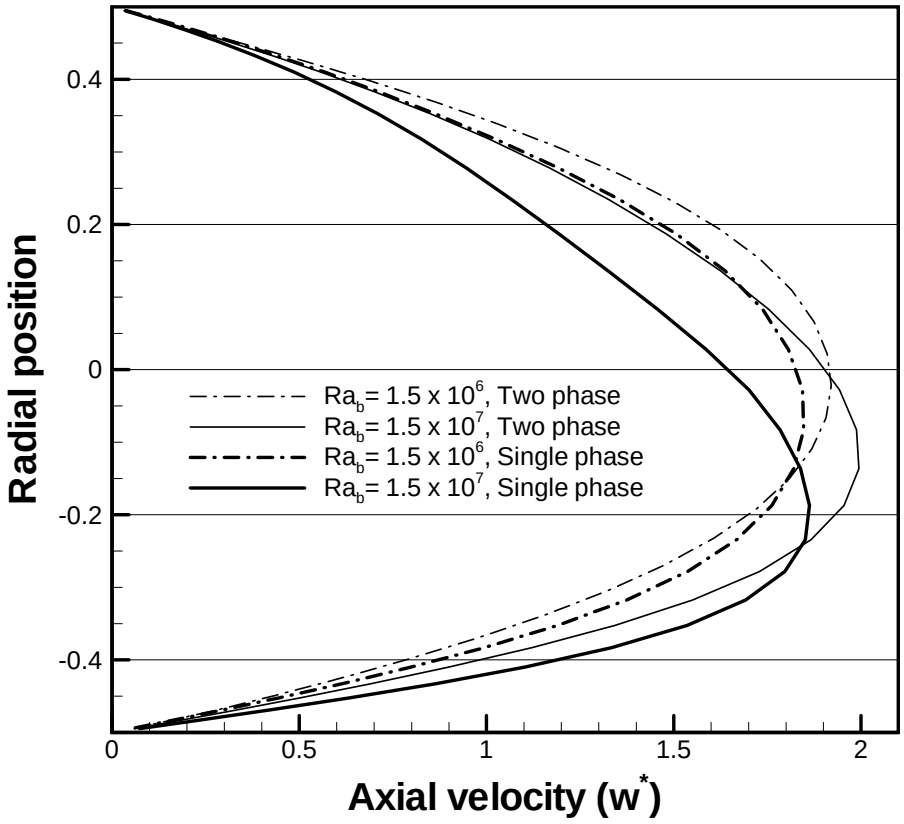

Figure 5-12 Two phase no melting – single phase outlet velocity profile comparison

5.3.3 PCM particles with melting

Both the particle and phase change effects are now included to investigate the effects of the Rayleigh number during the use of a microPCM slurry. The variations from the control case that were investigated are listed in Eq. 5.3, with all other quantities from the control case remaining constant.

$$\begin{aligned} &\mathrm{Ra}_b = 0,\ 0.15\mathrm{x}10^6,\ 1.5\mathrm{x}10^6,\ \textit{and}\ 15.0\mathrm{x}10^6 \\ &\mathrm{Ste} = 10.8\ \textit{and}\ \infty\ (\textit{no melting}) \end{aligned} \qquad 5.3$$

Dimensionless temperature results of the tube outer wall are presented in Fig. 5-13 and show the axial variation in temperature, all of these cases are two phase flows with the only difference being the PCM melting. Table 5-1 lists the difference in dimensionless wall temperature and the percent difference at the tube outlet for each Rayleigh number. At the lower Rayleigh numbers the % difference is lower than at the higher Rayleigh numbers.

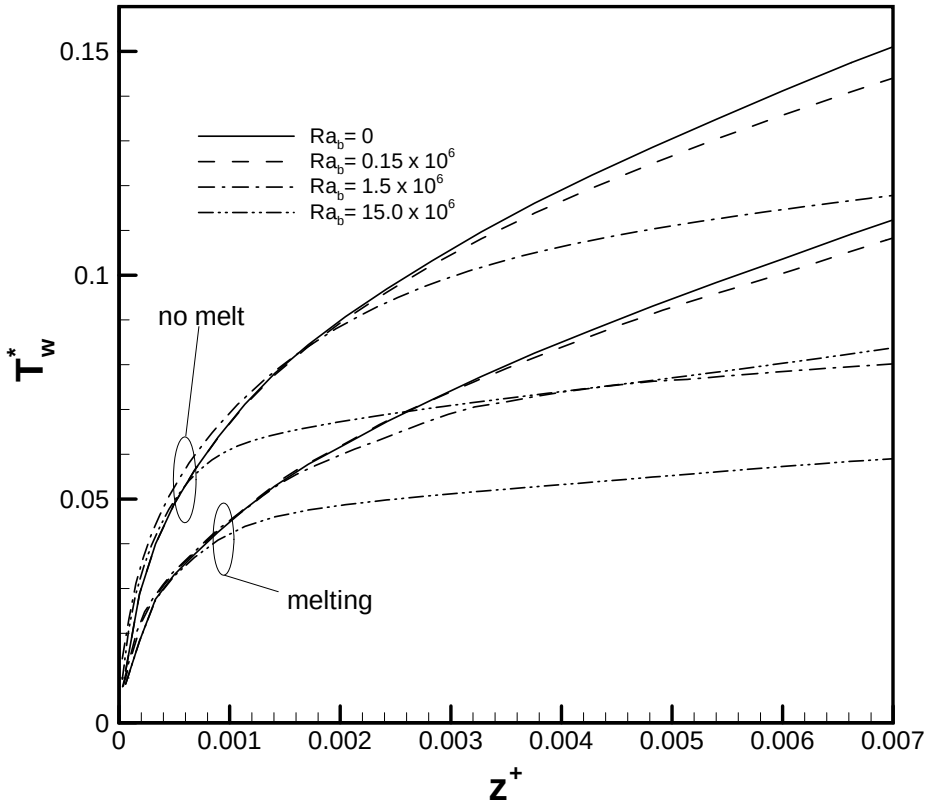

Figure 5-13 Rayleigh number variation

Table 5-3 Outlet tube wall temperature differences melting vs no melt at various Rayleigh numbers

Ra_b (x 10^6)	Difference in dimensionless wall temperature between cases with and without phase change at the tube outlet	% Difference
0	0.039	29
0.15	0.034	27
1.5	0.038	38
15.0	0.026	36

A contour plot of solid phase concentration and temperature along with velocity vector plot is provided for comparison, Fig 5-14, at the tube outlet for both particles with and without phase change at the three Rayleigh numbers which are not the control case, the control case contour and velocity plot is in Fig. 5-1.

When the Rayleigh number is zero there is no cross stream circulation due to fluid density variations only velocities associated with the buoyancy induced movement of the solid particles. As expected the concentration of solid particles is the same for melting and no melt and varies from 0.05 up to the packing limit 0.624 at the tube top. The temperature is nearly axisymmetric for both cases with the melting case having cooler fluid at all radial positions.

As the Rayleigh number is increased cross stream circulation begins to form in the no melt case as can be seen by the small velocity vectors and the downward deformation of the cooler core region. The melting case does not show the signs of any cross stream circulation due to fluid buoyancy. The fluid does remain cooler throughout the tube cross section as with the previous

case. Additionally there is very little change in the concentration contour from a Rayleigh number of 0 to 1.5 x 10^5 for both melting and no melt.

At the largest Rayleigh number, 1.5 x 10^5, the cross stream circulation is evident both by the velocity vectors and the temperature contours. The circulation of the no melting case is stronger as seen by the magnitude of the velocity vectors and the depression of the temperature contours. The stronger circulation also causes a nearly homogeneous fluid particle mixture across the tube which varies from 0.24 to 0.26. The melting case clearly has the lower temperature and since the temperature is the driving for behind the buoyancy driven flow of the liquid the circulation is weaker.

The axial development of the solids concentration are shown for Ra_b = 15.0 x 10^6 and Ra = 0, the extremes for the Rayleigh numbers investigated, in Fig.s 5-15 and 5-17, these may be compared with the control case, Fig. 5-2. At the inlet the solids concentrations start out similar but at an axial position of approximately 0.001 the high Rayleigh number case stops growing for the upper portion of the tube and stops declining for the lower portion. At this point the cross stream circulation is beginning to develop keeping the flow region closer to homogenous. A contour and vector plot is shown in Fig. 5-16 at this axial location in which the development of the circulation may be seen.

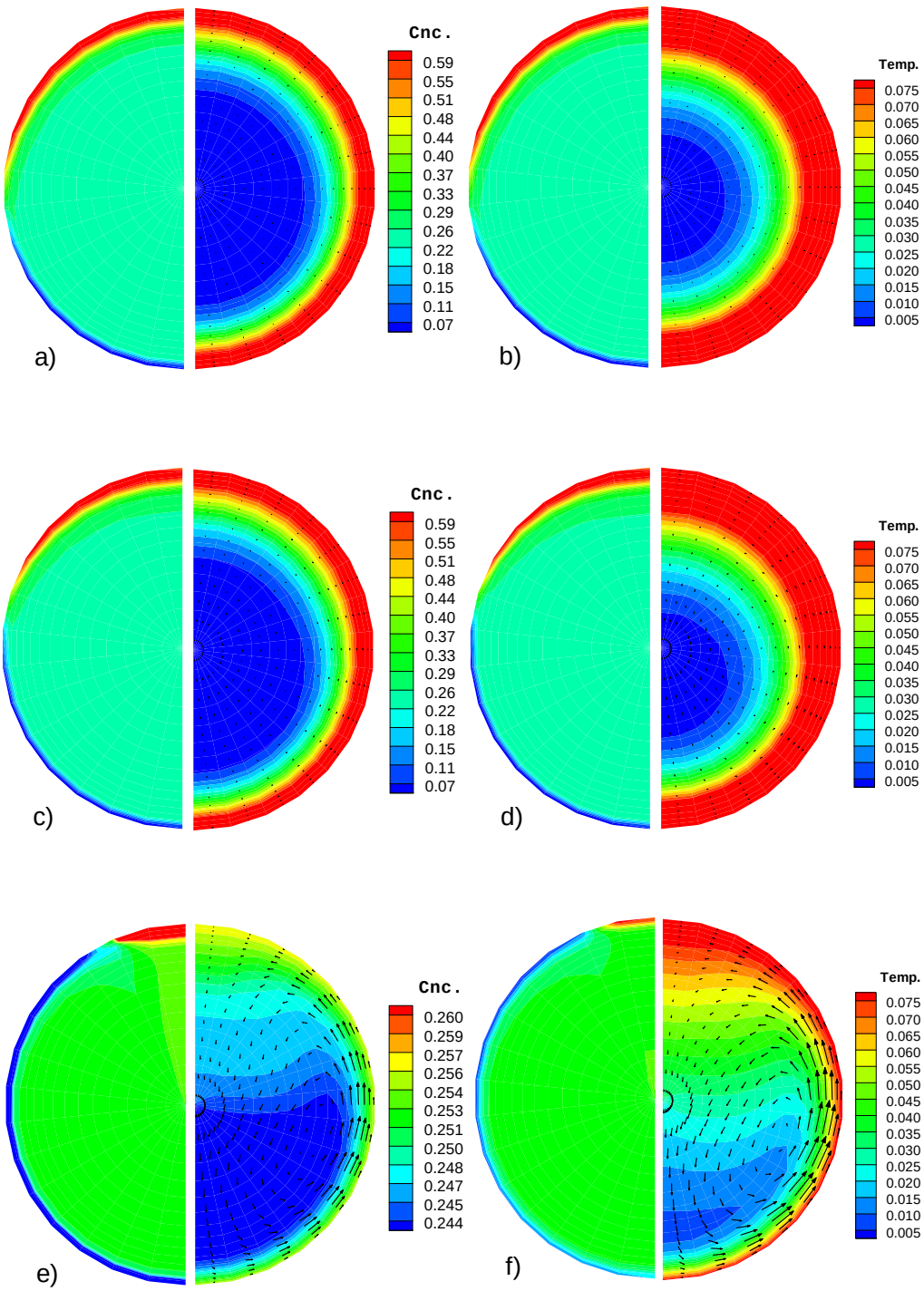

Figure 5-14 Concentration and temperature contours and velocity vectors at various Rayleigh numbers a) Ra_b= 0 melting, b) Ra_b= 0 no melt, c) Ra_b= 0.15 x 10^6 melting, d) Ra_b= 0.15 x 10^6 no melt, e) Ra_b= 15.0 x 10^6 melting, and f) Ra_b= 15.0 x 10^6 no melt

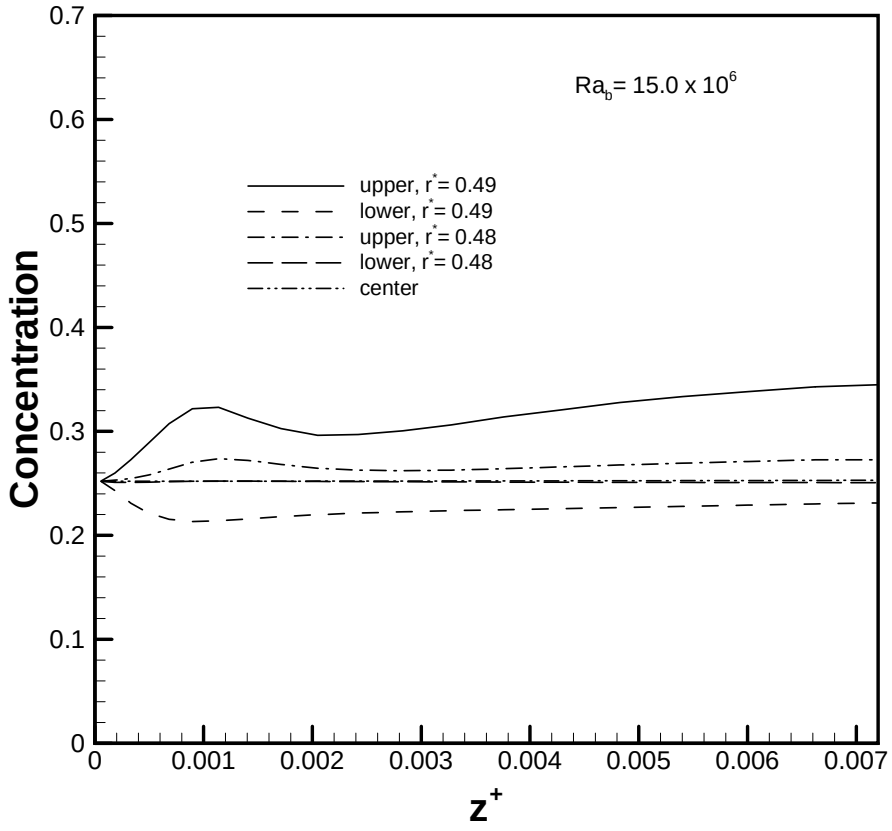

Figure 5-15 Solids concentration axial development at Ra_b = 15.0 x 10^6

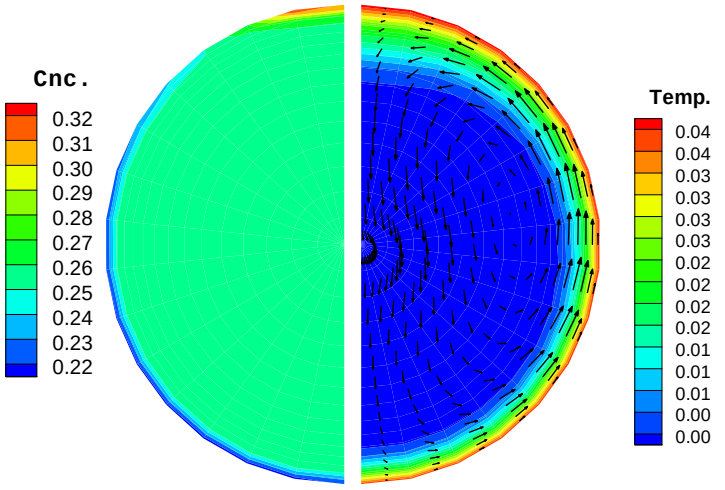

Figure 5-16 Solids concentration and temperature contours and velocity vector plots for Ra_b=15.0 x 10^6 at z^+= 0.0011

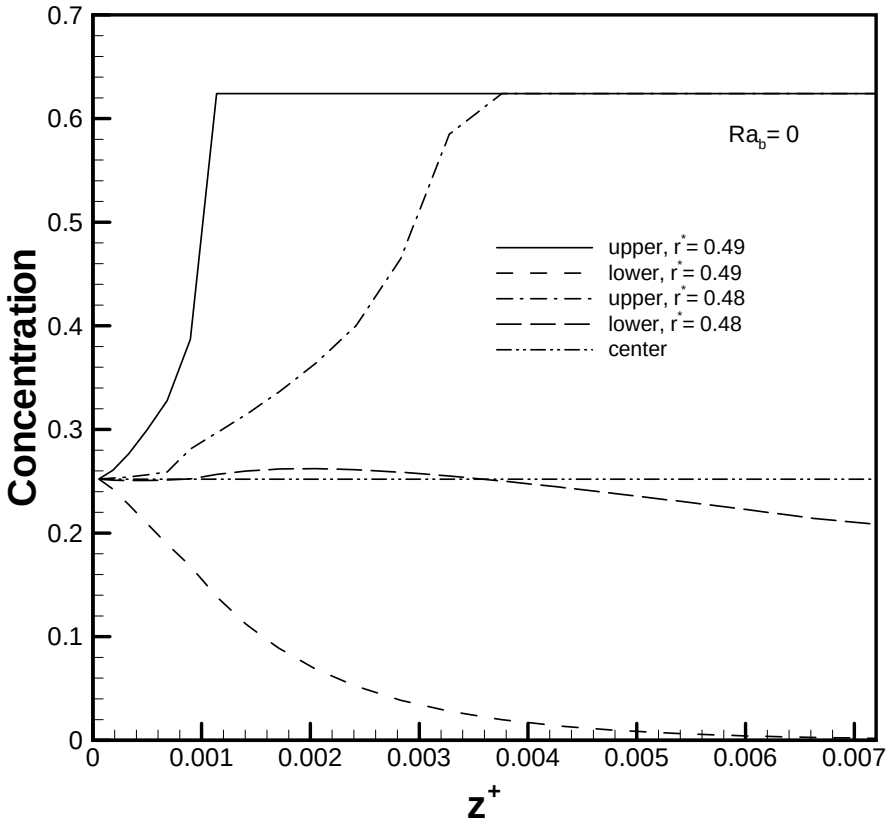

Figure 5-17 Solids concentration axial development at $Ra_b = 0$

The velocity profiles from bottom to top of the fluid axial velocity are shown in Fig. 5-18. There is very little difference in velocities at all but the highest Rayleigh number where there is some difference between the melting and no melt cases. The difference is due to the stronger cross stream circulation discussed previously associated with the no melt case.

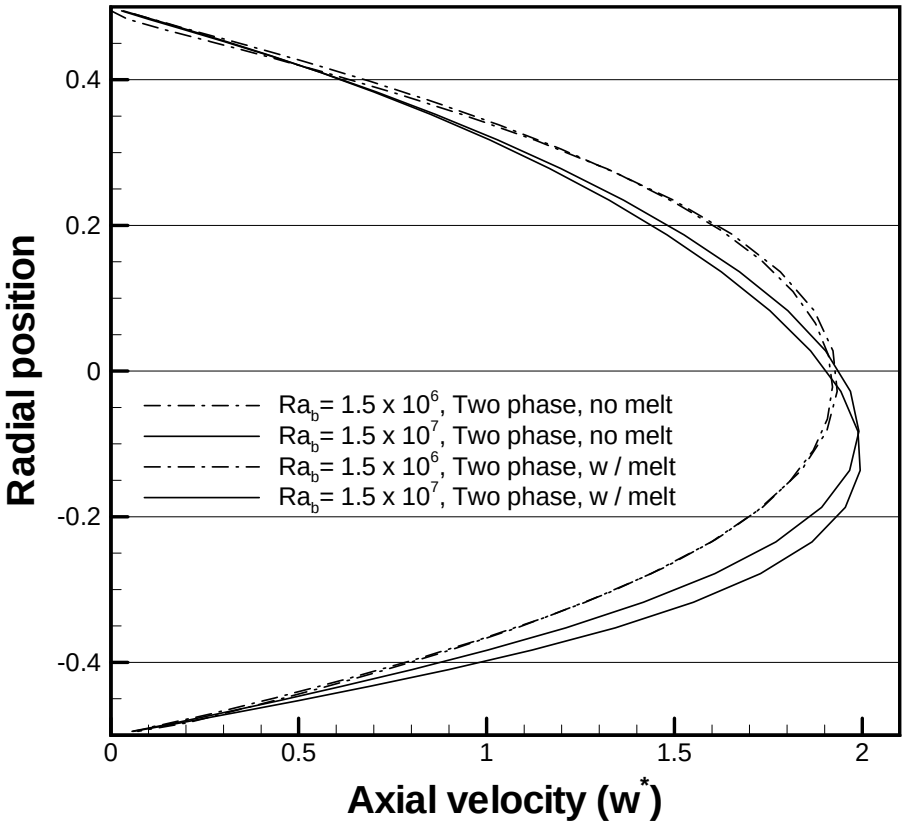

Figure 5-18 Outlet velocity profiles for two phase flow with and without PCM phase change

5.3.4 Stefan number

The Stefan number, an indication of the amount of latent heat energy available for storage, was varied according to the following

$$\mathrm{Ste} = 5.4,\ 10.8\ (\textit{control case}),\ 21.6,\ \textit{and}\ \infty\ (\textit{no melt}) \qquad 11$$

Figure 5-19 is a plot of dimensionless wall temperature along the axial length as expected with an increase in Stefan number the dimensionless wall temperature increases. This is because there is less latent heat storage available at a higher Stefan number.

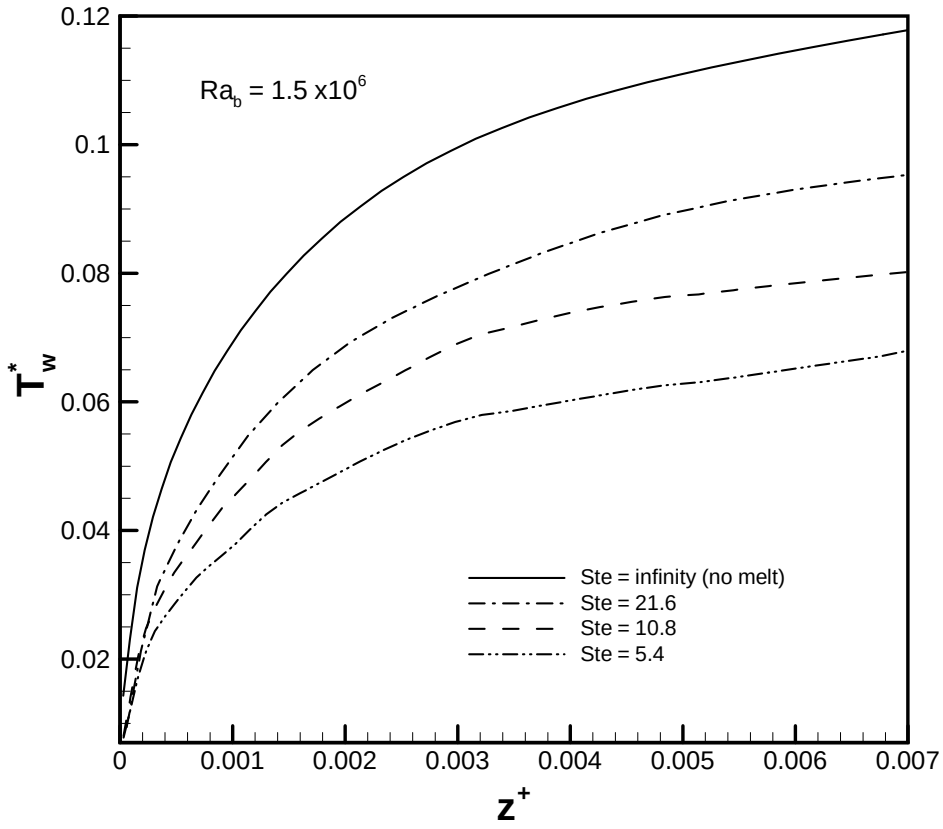

Figure 5-19 Stefan number variation

Solid concentration and temperature contours along with velocity vector plots are presented in Fig. 5-20. As the Stefan number is reduced the fluid temperature is also reduced due to the additional latent heat storage. The reduction in temperature then causes a lower circulation due to mixed convection and more particle separation with the microPCM particles accumulating at the top of the tube and less micro PCM particles at the lower portion of the tube.

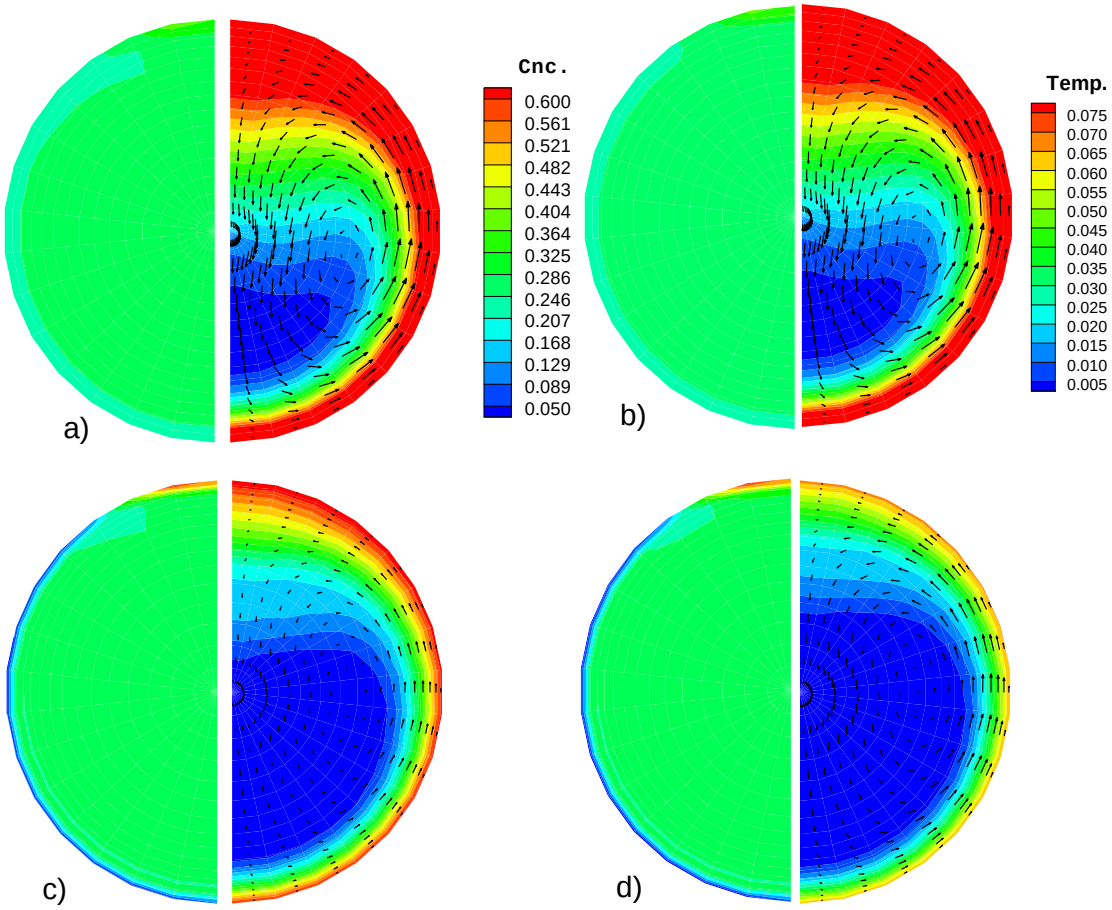

Figure 5-20 Contour and velocity vector plots a) Ste = ∞ (no melt), b) Ste = 21.6, c) Ste = 10.8 (control case), and d) Ste = 5.4

6 CONCLUSIONS

A two phase flow consisting of microPCM particles suspended in a 50 / 50 ethylene glycol water carrier fluid has been investigated both numerically and experimentally while the flow was in a mixed convective regime. The buoyancy driven secondary flows caused enhanced heat transfer similar to that of single phase flows. When comparing the numerical to experimental data it was found that supercooling allowed only a portion of the latent heat available to be used. This caused higher experimental wall temperatures than were predicted numerically.

The two phase mixed convective flow was similar to that of single phase flows but had lower buoyancy induced secondary flows. Even with the lower secondary flows the two phase mixture was numerically shown to produce lower tube wall temperatures even when the PCM material did not change phase. When the PCM was melting the temperature gradients within the flow were reduced which also reduced the secondary flows. The tube wall material was also shown to have a large effect on the tube wall temperatures due to circumferential conduction. The more conductive copper had a lower temperature difference from the top to the bottom of the tube than that of the stainless steel. It was also recommend that a constant pump power be used for comparison of different slurry mixtures.

Included within the numerical model were particle buoyancy effects which although small did cause the buoyant microPCM particles to separate and migrate toward the upper wall of the tube. The amount of segregation which occurred was not only dependent upon the particle buoyant parameters but also the amount of circulation due to mixed convection. As the Rayleigh number

was increased, and indication of the strength of circulation, the fluid became more homogenous keeping the microPCM particles mixed within the fluid.

6.1 Future Recommendations

6.1.1 Experimental

During the experimental phase, after heating the microPCM solution was not cooled below the crystallization temperature, therefore not all of the latent heat was available for energy storage and heat transfer enhancement. Efforts should be directed at reducing the supercooling effect through some of the available methods.[49] The resulting slurry should then be tested in a cooling loop with the ability to quantify the supercooling effect specifically by cooling the fluid below the crystallization temperature.

A second area of experimental focus should be in the use of the microPCM slurry in a more realistic cooling application which involves an actual system to be cooled. The experimentation would then need to include controlling both the heating and cooling processes to be able to quantify the use of the slurry in a pumped loop situation.

6.1.2 Numerical

The numerical methods should be expanded to include a loop type situation which would involve solutions to both the heating and cooling portions of the microPCM slurry. Also included should be the ability to include the effects of supercooling. Currently numerically only cases with no supercooling have been investigated this however is not realistic and over predicts the amount of enhanced heat transfer possible. Therefore, to calculate more realistic results the supercooling effect should be included in the numerical model.

7 REFERENCES

[1] Mulligan, J. C., Colvin, D. P., and Bryant, Y. G., "Microencapsulated Phase-Change Material Suspensions for Heat Transfer in Spacecraft Thermal Systems," Journal of Spacecraft and Rockets, Vol. 33, pp. 278-284.

[2] Jackson, W.B., Gould, R.D., and Mulligan, J.C., "Performance of an Octacosane Based MicroPCM Fluid for Cooling EV Electronics," 8th AIAA/ASME Joint Thermophysics and Heat Transfer Conference, AIAA paper 2002-3226, June 24-26, 2002.

[3] Kasza, K. E. and Chen, M. M., " Improvement of the Performance of Solar Energy or Waste Heat Utilization Systems by Using Phase-Change Slurry as an Enhanced Heat-Transfer Storage Fluid," Journal of Solar Energy Engineering, Vol. 107, 1985, pp. 229-236.

[4] Griffiths, P. W. and Eames, P. C., "Performance of Chilled Ceiling Panels Using Phase Change Material Slurries as the Heat Transport Medium," Applied Thermal Engineering, Vol. 27, 2007, pp. 1756-1760.

[5] Hart, R., and Thronton, F., "Microencapsulation of Phase Change Materials," Capsulated Systems, Inc., Final Report to Ohio Department of Energy, Contract 82-80, Fairborn, OH, Dec. 1982.

[6] Gibbs, B. M. and Hasnain, S. M., "DSC Study of Technical Grade Phase Change Heat Storage Materials for Solar Heating Applications," Solar Engineering, Vol. 2, 1995, pp. 1053-1062.

[7] Himran, S., Suwono, A. and Mabsoori, G. A., "Characterization of Alkanes and Paraffin Waxes for Application as Phase Change Energy Storage Medium," Energy Sources, Vol. 16, 1994, pp. 117-128.

[8] Goel, M., Roy, S. K., and Sengupta, S., "Laminar Forced Convection Heat Transfer in Microcapsulated Phase Change Material Suspensions," International Journal of Heat and Mass Transfer, Vol. 37, 1994, pp 593-604.

[9] Charunyakorn, P., Sengupta, S., and Roy, S. K., "Forced Convection Heat Transfer in Microencapsulated Phase Change Material Slurries: Flow in Circular Ducts," International Journal of Heat and Mass Transfer, Vol. 34, 1991, pp. 819-833.

[10] Zhang, Y. and Faghri, A., "Analysis of Forced Convection Heat Transfer in Microencapsulated Phase Change Material Suspensions," Journal of Thermophysics and Heat Transfer, Vol. 9, No. 4, 1995, pp. 727-732.

[11] Cassidy, D. and Gould, R. D., "Temperature Range and Conjugate Effects in Microencapsulated Phase Change Suspensions," Journal of Thermophysics and Heat Transfer, Vol. 22, 2008.

[12] Liu, Z. and Chung, D. D. L., "Calorimetric Evaluation of Phase Change Materials for Use as Thermal Interface Materials," Thermochimica Acta, Vol. 366, 2001, pp. 135-147.

[13] Montenegro, R. and Landfester, K., "Metastable and Stable Morphologies during Crystallization of Alkanes in Miniemulsion Droplets," Langmuir, Vol. 19, No. 15, 2003, pp 5996-6003.

[14] Lan, X. Tan, Z., Zou, G., Sun, L., and Shang, T., "Microencapsulation of n-eicosane as Energy Storage Material," Chinese Journal of Chemistry, Vol. 22, 2004, pp. 411-414.

[15] Gibbs, B. M. and Hasnain, S. M., "DSC Study of Technical Grade Phase Change Heat Storage Materials for Solar Heating Application," Solar Engineering, Vol. 2, 1995, pp. 1053-1062.

[16] Xing, K Q., Tao, T. X., and Hao, Y. L., "Performance Evaluation of Liquid Flow With PCM Particles in Microchannels," Journal of Heat Transfer, Vol. 127, 2005, pp. 931-940.

[17] Choi, E., Cho, Y. I., and Lorsch, H. G., "Forced Convection Heat Transfer with Phase-Change-Material Slurries: Turbulent Flow in a Circular Tube," International Journal of Heat and Mass Transfer, Vol. 37, 1994, pp. 207-215.

[18] Rao, Y., Dammel, F., and Stephan, P., "Convective Heat Transfer Characteristics of Microencapsulated Phase Change Material Suspensions in Minichannels," Heat and Mass Transfer, Vol. 44, 2007, pp. 175-186.

[19] Yang, J. and Chalaturnyk, R. J., "Computational Fluid Dynamics Simulation of a Very Dense Liquid – Solid Flow Using a Eulerian Model," from Computational Methods in Multiphase Flow III, Vol. 50 WIT Press, 2005.

[20] Ling, J., Skudarnov, P. V., Lin, C. X., and Ebadian, M. A., "Numerical Investigations of Liquid-Solid Slurry Flows in a Fully Developed Turbulent Flow Region," International Journal of Heat and Fluid Flow, Vol. 24, 2003, pp. 389-398.

[21] Yang, B. H., Wang, J., Hoseph, D. D>, Hu, H.H., Pan, T.-W., and Glowinski, R., "Numerical Study of Particle Migration in Tube and Plane Poiseuille Flows," Proceedings of the IUTAM Symposium on Computational Multiphase Flow, 2006, pp. 225-235.

[22] Petukhov, B. S.and Polyakov, A. F., "Experimental Investigation of Viscogravitational Fluid Flow in a Horizontal Tube," Scientific Research Institute of High Temperature, Vol. 5, 1967, pp. 87-95.

[23] Gebhart, B., Jaluria, Y. Mahajan, R. L., and Sammakia, B., Buoyancy-Induced Flows and Transport, Hemisphere Publishing Corp., New York, NY, 1988.

[24] Incropera, F. P. and Dewitt, D. P., Fundamentals of Heat and Mass Transfer, 5th ed., Wiley, New Jersey, 2002, p. 539.

[25] Churchill, S. W., "Combined Free and Forced Convection in Channels," Heat Exchanger Design Handbook, Part 2, Hewitt, G. F. Editor, Begell House, Inc. New York, NY, 1998

[26] Morcos, S. M. and Bergles, A. E., "Experimental Investigation of Combined Forced and Free Laminar Convection in Horizontal Tubes," Journal of Heat Transfer, Vol . 97, 1975, pp. 212-219.

[27] Zhang, C. and Bell , K. J., "Mixed Convection Inside Horizontal Tubes with Nominally Uniform Heat Flux," AIChE Symposium Series, Heat Transfer-San Diego 1992, Vol. 88, pp.212-219.

[28] Shome, B. and Jensen, M. K., "Mixed Convection Laminar Flow and Heat Transfer of Liquids in Isothermal Horizontal Circular Ducts," International Journal of Heat and Mass Transfer, Vol. 38, 1995, pp. 1945-1956.

[29] Ouzzane, M. and Galanis, N., "Developing Mixed Convection in an Inclined Tube with Circumferentially Nonuniform Heating at its Outer Surface," Numerical Heat Transfer, Part A, Vol. 35, 1999, pp. 609-628.

[30] Wang, M., Tsuji, T., and Nagano, Y., "Mixed Convection with Flow Reversal in the Thermal Entrance Region of Horizontal and Vertical Pipes," International Journal of Heat and Mass Transfer, Vol. 37, 1994, pp. 2305-2319.

[31] Inaba, H., Dai, C., and Horibe, A., "Natural Convection Heat Transfer in Enclosures with Microemulsion Phase Change Material Slurry," Heat and Mass Transfer, Vol. 40, 2004, pp. 179-189.

[32] Barozzi, G. S. and Pagliarini, G., "A Method to Solve Conjugate Heat Transfer Problems: The Case of Fully Developed Laminar Flow in a Pipe," Journal of Heat Transfer, Vol. 107, 1985, pp. 77-83.

[33] Bouillard, J. X., Lyczkowski, R. W., and Gidaspow, D., "Porosity Distributions in a Fluidized Bed with an Immersed Obstacle," AIChE Journal, Vol. 35, 1989, pp. 908-922.

[34] Michaelides, E. E., "Hydrodynamic Force and Heat/Mass Transfer From Particles, Bubbles, and Drops – The Freeman Scholar Lecture," Journal of Fluids Engineering, Vol. 125, 2003, pp. 209-238.

[35] Massoudi, M., Rajagopal, K. R., Ekmann, J. M., and Mathur, M.P., "Remarks on the Modeling of Fluidized Systems," AIChE Journal, Vol. 38, 1992, pp. 471-472,

[36] Ranz, W. E. and Marshall, Jr., W. R., " Evaporation From Drops, Part II," Chemical Engineering Progress., Vol. 48, 1952, pp. 173-180.

[37] Floyd, S., Choi, K. Y., Taylor, T. W., and Ray, W. H., Polymerization of Olefins Through Heterogeneous Catalysis IV. Modeling of Heat and Mass Transfer Resistance in the Polymer Particle Boundary Layer," Journal of Applied Polymer Science, Vol. 31, 1986, pp. 2231-2265.

[38] Xing, K. Q., Tao, Y. X., and Hao, Y. L., "Slurry Viscosity Study and its Influence on Heat Transfer Enhancement Effect of PCM Slurry Flow in Micro/Mini Channels," Proceedings of IMECE2006-14902, 2006 ASME International Mechanical Engineering Congress and Exposition, Nov. 5-10, 2006.

[39] Thomas, D. G., "Transport Characteristics of Suspension: VIII. A Note on the Viscosity of Newtonian Suspensions of Uniform Spherical Particles," Journal of Colloid Science, Vol. 20, 1965, pp. 267-277.

[40] Enwald, H., Peirano, E., and Almstedt, A. E., "Eulerian Two-Phase Flow Theory Applied to Fluidization," International Journal of Multiphase Flow, Vol. 22, 1996, pp. 21-66.

[41] Kuipers, J. A. M., Prins, W., and van Swaaij, P. M., "Numerical Calculation of Wall-to-Bed Heat-Transfer Coefficients in Gas-Fluidized Beds," AIChE Journal, Vol. 38, 1992, pp. 1079-1091.

[42] Bart, G. C. J., and van der Laag, P. C., " Modeling of Arbitrary-Shaped Specific and Latent Heat Curves in Phase-Change Storage Simulation Rutines," Journal of Solar Engineering, Vol. 112, 1990, pp. 29-33.

[43] Hu, X., and Zhang, Y., " Novel Insight and Numerical Analysis of Convective Heat Transfer Enhancement with Microencapsulated Phase Change Material Slurries: Laminar Flow in a Circular Tube with Constant Heat Flux," International Journal of Heat and Mass Transfer, Vol. 45, 2002, pp. 3163-3172.

[44] Yamagishi, Y., Sugeno, T., and Ishige, T., "An Evaluation of Microencapsulated PCM for use in Cold Energy Transportation Medium," IEEE paper, No. 96082, 1996.

[45] Sun T. and Teja, A., S., "Density, Viscosity, and Thermal Conductivity of Aqueous Ethylene, Diethylene, and Triethylene Glycol Mixtures between 290 K and 450 K," Journal of Chemical Engineering Data, Vol. 48, 2003, pp.198-202.

[46] Daubert T. E. and Danner, R. P., Data Compilation Tables of Properties of Pure Compounds, Desiogn Institute for Physical Property Data American Institute of Chemical Engineers, New York, NY, 1985.

[47] Himran, S., Suwono, A., and Mansoori, G. A., "Characterization of Alkanes and Pariffin Waxes for Application as Phase Change Energy Storage Medium, Energy Sources," Vol 16, 1994, pp. 117-128.

[48] Sharma, S. D. and Sagara, K., "Latent Heat Storage Materials and Systems: A Review," International Journal of Green Energy, Vol. 1, 2005. , pp. 1-56

[49] Zhang, X. X., Fan, Y. F., Tao, X. M., and Yick, K. L., "Crystallization and Prevention of Supercooling of Microencapsulated n-alkanes," Journal of Colloid and Interface Science, Vol. 281, 2005, pp. 299-306.

[50] Royon, L. and Guiffant, G., " Heat Tansfer in Paraffin Oil/Water Emulsion Involving Supercooling Phenomenon," Energy Conservation Management, Vol. 42, 2001, pp. 2155-2161.

[51] Churchill, S. W. and Ozoe, H., "Correlations for Laminar Forced Convection with Uniform Heating in Flow Over a Plate in Developing and Fully Developed Flow in a Tube," Journal of Heat Transfer, Vol. 95, 1973, pp.78-85.

[52] Kline, S. J. and McKlintock, F. A., "Describing Uncertainties in Single-Sample Experiments," Mechanical Engineering, Vol. 75, 1953, pp. 385-387.

[53] Morcos, S. M. and Bergles, A. E., "Experimental Investigation of Combined Forced and Free Laminar Convection in Horizontal Tubes," Journal of Heat Transfer, 1975.

[54] Tannehill, J. C., Anderson, D. A., and Pletcher, R. H., Computational Fluid Mechanics and Heat Transfer, 2nd edition, Taylor and Francis, Philadelphia, PA, 1997.

[55] Patankar, S. V., Numerical Heat Transfer and Fluid Flow, Hemisphere Publishing Corp., New York, NY, 1980.

[56] Zhang, K., Zhang, H., Lovick, J., Zhang, J., and Zhang, B., "Numerical Computation and Experimental Verification of the Jet Region in a Fluidized Bed," Industrial and Engineering Chemistry Research., Vol. 41, 2002, pp.3696-3794.

[57] Spalding, D. B., "Numerical Computation of Multi-Phase Fluid Flow and Heat Transfer," Recent Advances in Numerical Methods in Fluids, Vol. 1, Taylor, K. M. Editor, Pineridge Press, Swansea, 1980.

[58] Spalding, D. B., "Developments in the IPSA Procedure for Numerical Computation of Multiphase-flow Phenomena with Interphase Slip, Unequal Temperatures, etc.," Numerical

Methodologies in Heat Transfer, Shih, T. M. Editor, Proceedings of the Second National Symposium, Hemisphere, New York, 1983.

[59] Van Doormal, J. P. and Raithby, G. D., "Enhancement of the SIMPLE Method for Predicting Incompressible Fluid Flows," Numerical Heat Transfer, Vol. 7 pp., 1984, 147-163.

[60] Zhao, X. Richards, P. G., Shang, S. J., and Liu, J., "High-Resolution Schemes for Bubbling Flow Computations," Applied Mathematical Modeling, Vol. 29, 2005, pp. 1232-1251.

[61] Carver, M. B., "A Method of Limiting Intermediate Values of Volume Fraction in Iteratitive Two-Fluid Computations," Journal Mechanical Engineering Science, Vol. 24, 1982, pp. 221-224.

[62] Zhang, K., Zhang, J., and Zhang B., "CFD Simulation of Jet Behavior and Voidage Profile in a Gas-Solid Fluidized Bed," International Journal of Energy Research, Vol. 28, 2004, pp. 1065-1074.

[63] Siegel, R., Sparrow, E. M., and Hallman, T. M., "Steady Laminar Heat Transfer in a Circular Tube with Prescribed Wall Heat Flux," Applied Scientific Research, Vol. 7., 1958, pp. 386-392.

[64] Shook, C. A. and Roco, M.C., Slurry Flow Principles and Practice, Butterworth-Heinemann, Stoneham, MA, 1991.

APPENDIDICES

APPENDIX A

Considering the dimensional form of Eq. 2.2

$$\left(\frac{\partial(\alpha_l \rho_l v_{rl})}{\partial t}+\frac{\partial(\alpha_l \rho_l v_{rl}^2)}{\partial r}+\frac{1}{r}\frac{\partial(\alpha_l \rho_l v_{rl} v_{\theta l})}{\partial \theta}-\frac{\alpha_l \rho_l v_{\theta l}^2}{r}+\frac{\partial(\alpha_l \rho_l v_{rl} v_{zl})}{\partial z}\right)=$$

$$-\alpha_l \frac{\partial p}{\partial r}-\alpha_l \rho_l g\cos\theta - K_{ls}(v_{rl}-v_{rs}) \qquad \text{A.1}$$

$$+\left(\frac{\partial}{\partial r}\left(\frac{1}{r}\mu_l \alpha_l \frac{\partial(r v_{rl})}{\partial r}\right)+\frac{1}{r^2}\frac{\partial}{\partial \theta}\left(\mu_l \alpha_l \frac{\partial v_{rl}}{\partial \theta}\right)-\frac{2\mu_l \alpha_l}{r^2}\frac{\partial v_{\theta l}}{\partial \theta}\right)$$

The first and second terms are combined using the fact that the second is the radial derivative of the hydrostatic pressure, the first and second terms are

$$-\alpha_l \frac{\partial p}{\partial r}-\alpha_l \rho_l g\cos\theta \qquad \text{A.2}$$

Using Bousinesq approximation for the temperature dependent fluid density

$$\rho_l = \rho_{in\,l}-\rho_{in\,l}\beta(T-T_{in\,l}) \qquad \text{A.3}$$

now defining an alternate pressure which includes hydrostatic pressure

$$p^+ = p+\alpha_l \rho_{inl} g r\cos\theta+\alpha_s \rho_s g r\cos\theta \qquad \text{A.4}$$

then taking the derivative with respect to the radial direction and rearranging

$$\frac{\partial p}{\partial r}=\frac{\partial p^+}{\partial r}-\alpha_l \rho_{inl} g\cos\theta-\alpha_s \rho_s g\cos\theta \qquad \text{A.5}$$

Substituting Eq. A.5 into Eq. A.2 the term becomes

$$-\alpha_l \frac{\partial p}{\partial r}-\alpha_l \rho_l g\cos\theta =$$

$$-\alpha_l\left(\frac{\partial p^+}{\partial r}-\alpha_l \rho_{inl} g\cos\theta-\alpha_s \rho_s g\cos\theta\right)-\alpha_l \rho_l g\cos\theta \qquad \text{A.6}$$

Replacing the liquid volumetric fraction that is in the parenthesis of Eq. A.6 with

$$\alpha_l = 1.0 - \alpha_s \tag{A.7}$$

and after rearranging the original term, Eq. A.2, may be written as

$$\begin{aligned} -\alpha_l \frac{\partial p}{\partial r} - \alpha_l \rho_l g \cos\theta = \\ -\alpha_l \frac{\partial p^+}{\partial r} + \alpha_l \rho_{in\,l} g \cos\theta - \alpha_l \rho_l g \cos\theta - \alpha_l \alpha_s g \cos\theta \left(\rho_{in\,l} - \rho_s\right) \end{aligned} \tag{A.8}$$

Substituting the liquid density of Eq. A.3 yields

$$\begin{aligned} -\alpha_l \frac{\partial p}{\partial r} - \alpha_l \rho_l g \cos\theta = \\ -\alpha_l \frac{\partial p^+}{\partial r} + \alpha_l \rho_{in\,l} g\beta\left(T - T_{in\,l}\right)\cos\theta - \alpha_l \alpha_s g \cos\theta \left(\rho_{in\,l} - \rho_s\right) \end{aligned} \tag{A.9}$$

Included in Eq. A.9 are both a liquid buoyancy term which is dependant upon the local temperature and a solid buoyancy term which is dependant upon the density of the solid phase of the two phase mixture. The liquid phase equation, Eq. A.1 may now be written as

$$\left(\frac{\partial(\alpha_l\rho_l v_{rl})}{\partial t}+\frac{\partial(\alpha_l\rho_l v_{rl}^2)}{\partial r}+\frac{1}{r}\frac{\partial(\alpha_l\rho_l v_{rl}v_{\theta l})}{\partial\theta}-\frac{\alpha_l\rho_l v_{\theta l}^2}{r}+\frac{\partial(\alpha_l\rho_l v_{rl}v_{zl})}{\partial z}\right)=$$

$$\begin{aligned}&-\alpha_l\frac{\partial p}{\partial r}+\alpha_l\rho_{in\,l}g\beta(T-T_{in\,l})\cos\theta-\alpha_l\alpha_s g\cos\theta(\rho_{in\,l}-\rho_s)\\&-\alpha_l\rho_l g\cos\theta-K_{ls}(v_{rl}-v_{rs})\\&+\left(\frac{\partial}{\partial r}\left(\frac{1}{r}\mu_l\alpha_l\frac{\partial(rv_{rl})}{\partial r}\right)+\frac{1}{r^2}\frac{\partial}{\partial\theta}\left(\mu_l\alpha_l\frac{\partial v_{rl}}{\partial\theta}\right)-\frac{2\mu_l\alpha_l}{r^2}\frac{\partial v_{\theta l}}{\partial\theta}\right)\end{aligned}$$

A.10

Where the superscript on the pressure term has now been dropped, using the defined dimensionless variables and including the solids pressure term Eq. 2-12 is obtained. The same process may be used to obtain the solid phase equation, which in dimensional form is

$$\left(\frac{\partial(\alpha_l\rho_l v_{rl})}{\partial t}+\frac{\partial(\alpha_l\rho_l v_{rl}^2)}{\partial r}+\frac{1}{r}\frac{\partial(\alpha_l\rho_l v_{rl}v_{\theta l})}{\partial\theta}-\frac{\alpha_l\rho_l v_{\theta l}^2}{r}+\frac{\partial(\alpha_l\rho_l v_{rl}v_{zl})}{\partial z}\right)=$$

$$\begin{aligned}&-\alpha_l\frac{\partial p}{\partial r}+\alpha_l\rho_{in\,l}g\beta(T-T_{in\,l})\cos\theta-\alpha_l\alpha_s g\cos\theta(\rho_{in\,l}-\rho_s)\\&-\alpha_l\rho_l g\cos\theta-K_{ls}(v_{rl}-v_{rs})\\&+\left(\frac{\partial}{\partial r}\left(\frac{1}{r}\mu_l\alpha_l\frac{\partial(rv_{rl})}{\partial r}\right)+\frac{1}{r^2}\frac{\partial}{\partial\theta}\left(\mu_l\alpha_l\frac{\partial v_{rl}}{\partial\theta}\right)-\frac{2\mu_l\alpha_l}{r^2}\frac{\partial v_{\theta l}}{\partial\theta}\right)\end{aligned}$$

A.11

An assumption that the solid phase and liquid phase share the same pressure has also been used. The solid phase does not include the temperature dependent term as it has been assumed the solid phase remains at a constant density. Also the solid – liquid term is of opposite signs in the two equations as they exert opposite and equal forces on each other.

Similarly the circumferential direction includes buoyancy terms and is then converted to dimensionless form which includes the Grashoff and Archimedes numbers. The axial direction however, is horizontal and thus no body (gravity) forces are included.

APPENDIX B

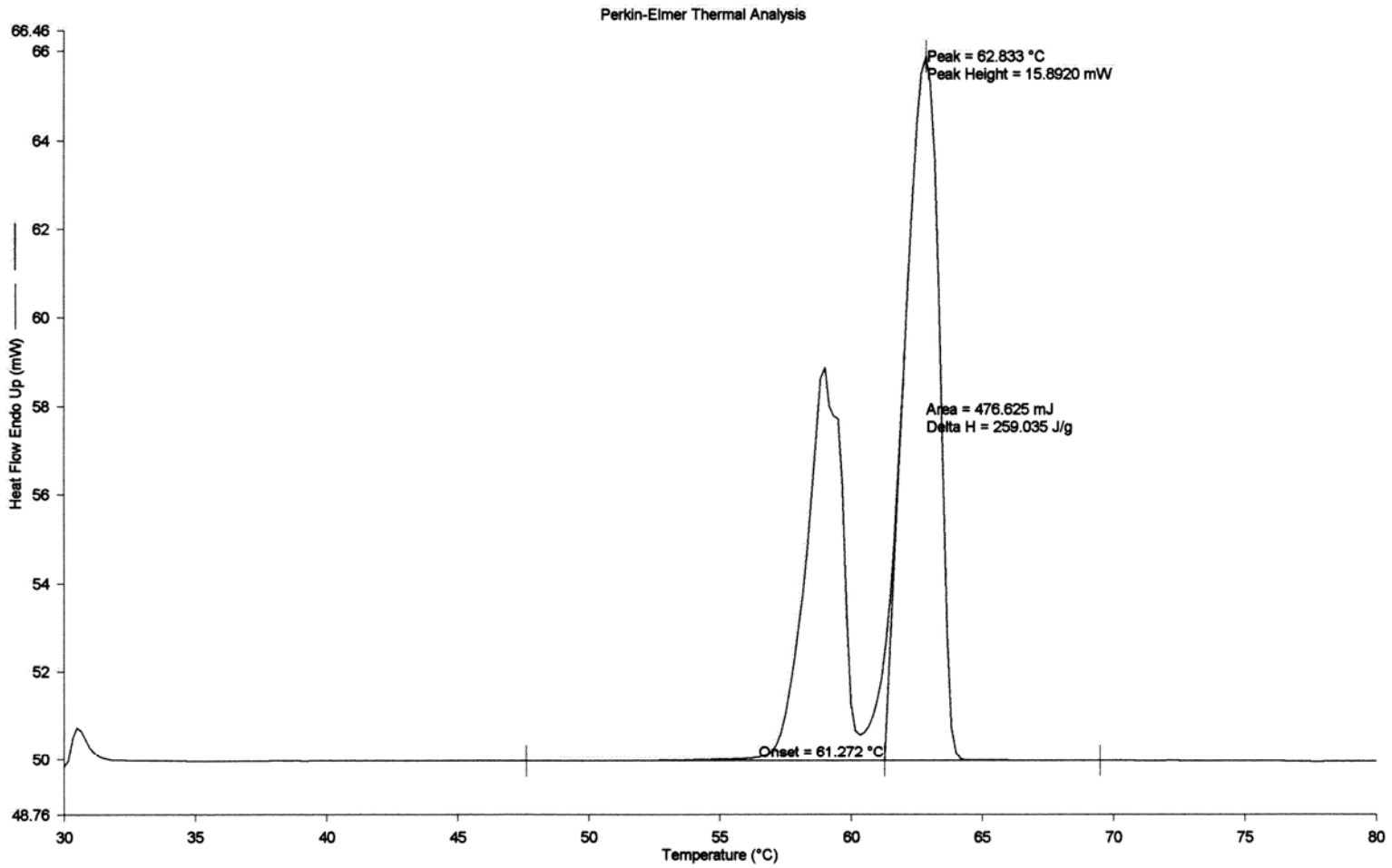

Figure B-1 Bulk octacosane DSC results from a heating process

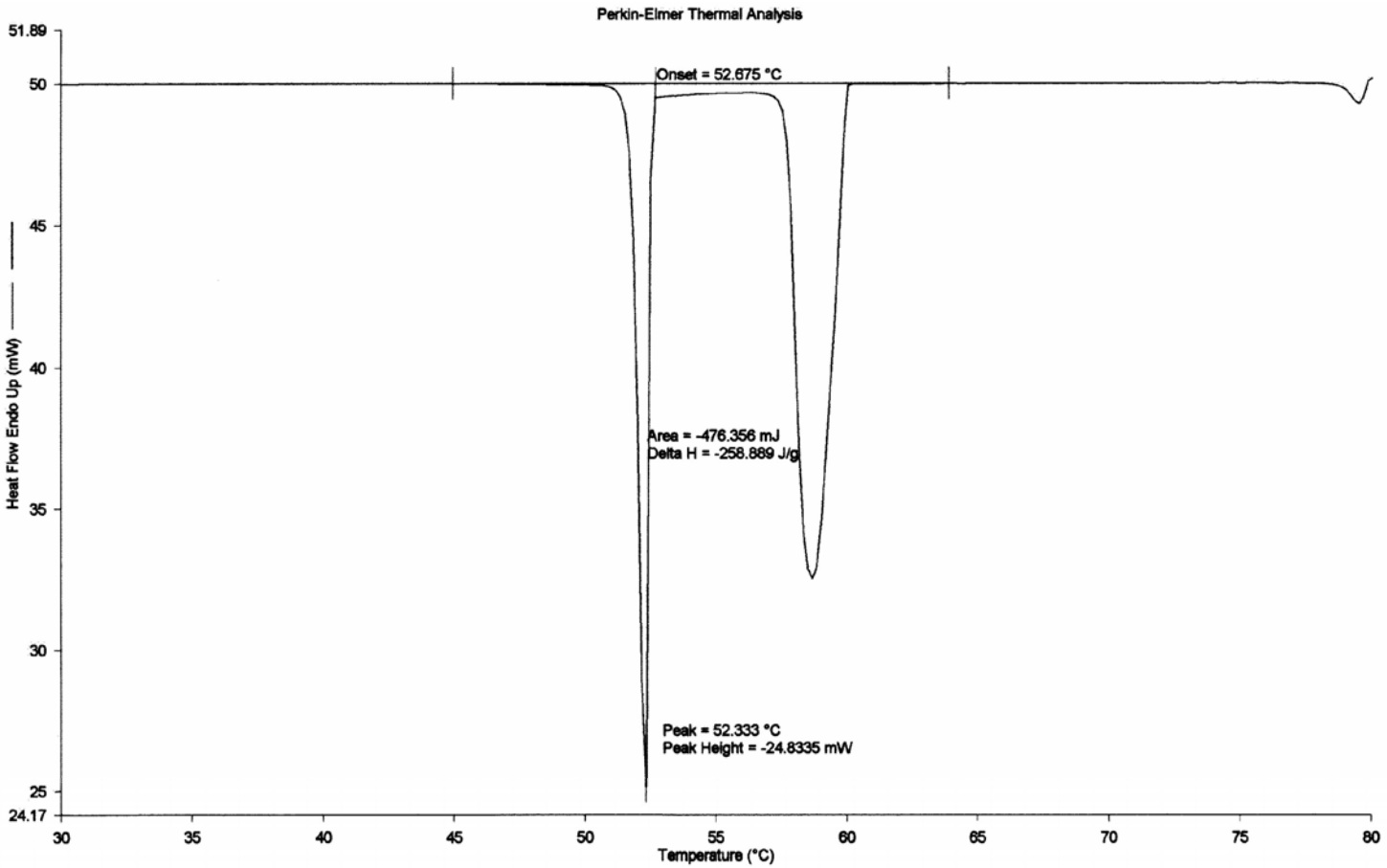

Figure B-2 Bulk octacosane DSC results from a cooling process